MEASUREMENT OF THE MECHANICAL PROPERTIES OF ANGLE PLY LAMINATES

By

Jing Wang

A thesis submitted in conformity with the requirements
for the Degree of Doctor of Philosophy
Department of Chemical Engineering and Applied Chemistry
University of Toronto

MEASUREMENT OF THE MECHANICAL PROPERTIES OF ANGLE PLY LAMINATES

Doctor of Philosophy 2000

Jing Wang

Department of Chemical Engineering and Applied Chemistry

University of Toronto

ABSTRACT

Design of advanced fiber composite structures requires a knowledge of the strength and stiffness of laminates. For modulus, designs rely on classical lamination theory. For strength a failure criterion is needed. For off-axis plies this is normally a maximum stress criterion, or smoothed out versions such as "Tsai-Wu". They are based on early experiments on long and narrow specimens. However, tests on short and wide specimens gave much higher results both for modulus and strength. These are confirmed by test on tubes, which have been available in the literature and appear to have been ignored by designers. The problem is due to an edge softening effect. The edge softening effect can cause the stiffness and the strength to be undervalued in tensile tests.

Experimental data on carbon/epoxy angle ply laminates' tensile properties are presented here based on tests of short and wide specimens and ASTM specimens. The wider specimens gave higher moduli than the narrow ones for lay-up angles of 15^0, 30^0,

and 45^0. This trend disappeared when the angles were bigger than 45^0. The moduli were within classical lamination theory prediction boundaries. Measured Poisson's ratios were much less than the theoretical values due to the end constraint. The angle ply laminates showed non-elastic deformation at low stress levels except for the 0^0 and 90^0 lay-ups.

The photoelastic method was used to provide an overall strain image in the gauge area. The images showed a uniform stress distribution when the samples were in the elastic range and a non-uniform stress distribution at higher stresses. The fiber presence was observed from lines or bands visible in the pictures.

It is clear from the results that there are ineffective or partially effective regions in the test specimens. and the size of these depend both on ply angle ϕ and specimen aspect ratio. An edge softening model has been set up based on the results. The model fitted the test data very well for the stiffness but only fairly well for the strength.

ACKNOWLEDGEMENTS

I wish to express my deepest gratitude and thanks to Professor M. R. Piggott for his supervision, guidance and encouragement during the course of this research and writing of this thesis. I am grateful to Professor M. T. Kortschot and Professor J. S. Hansen for being my reading committee members and giving me guidance and advice. Special thanks to Jenny Clifford for her friendship, help, and encouragement.

I am thankful to all members of the Advanced Composite Physics and Chemistry Group for their support and friendship. Thanks all of you, Mimi, Alex, Lynn, Chris, Shane, Asif, Michael, Vicky, and Jessica, for providing an enjoyable research environment. It was fun. Many thanks to Mr. Shuren Dai for his technical assistance.

I am especially indebted to my dear wife Xiao Fang, and my sons Zi Teng and Zi Yang. Without their full support I could not have finished my degree. They shared all the laughs and tears with me during my studies and experimental difficulties.

Last but not least, greatest thanks to my parents who planned my desires to be a doctor.

TABLE OF CONTENTS

LIST OF FIGURES

LIST OF TABLES

1. INTRODUCTION

1.1. Composite Materials

1.1.1. General Description

Structural materials can be divided into four basic categories: metals, polymers, ceramics and composites. Composites, which consist of two or more separate materials combined in a macroscopic structural unit, are made from various combinations of the other three materials. Although many man made materials have two or more constituents, they are generally not referred to as composites if the structural unit is formed at the microscopic level rather than at the macroscopic level. Thus metallic alloys and polymer blends are usually not classified as composites. Table 1.1 [1] indicates the scale of polymer fiber composites relative to atomic, molecular, and complete engineering structure sizes.

The relative importance of the four basic materials in a historical context has been presented by Ashby [2], as shown schematically in Figure 1.1. In this the steadily increasing importance of polymers, composites, and ceramics and the decreasing role of metals is shown clearly. Fiber composites are generally used because they have desirable properties which could not be achieved by either of the constituent materials acting alone.

Table 1.1. The scale of polymer fiber composites [1]

	pm	nm	μm	mm	m	km
Atom	**					
Polymer molecules		***				
Biological high polymers		** **				
Crystallite		* *				
Spherulite			***			
Fiber diameter			*			
Lamina thickness			*	**		
Laminate thickness				***		
Laminate length					*** **	
Usable structure						*****

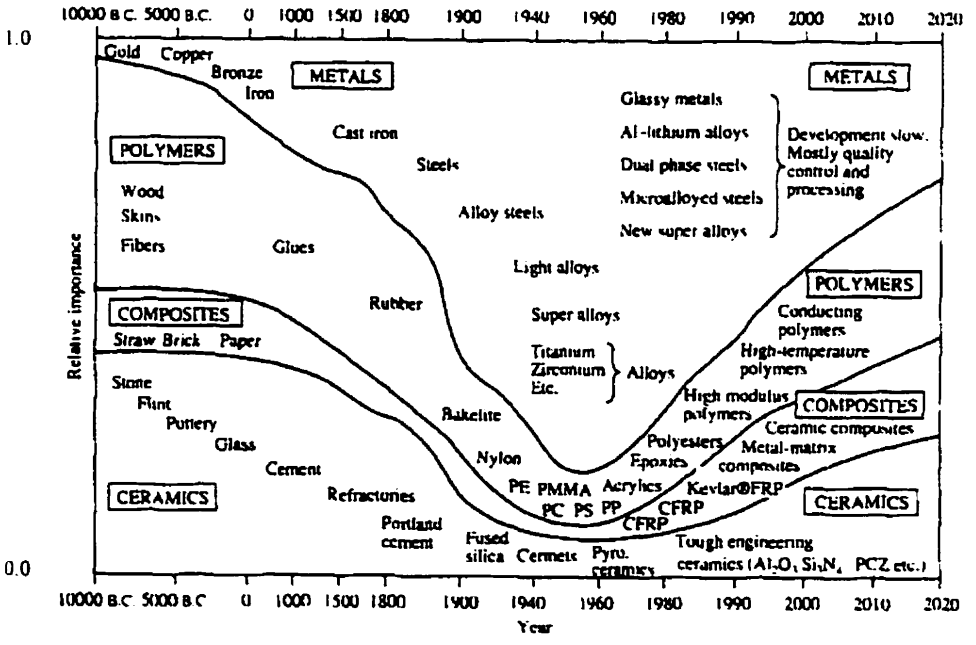

Figure 1.1. Relative importance of materials as a function of time [2]

Composite materials can be observed in many naturally occurring substances. Wood is an organic composite composed primarily of bundles of cellulose fibers embedded in an amorphous lignin matrix at a ratio of about two to one. The strong cellulose fiber and the strong bonding between the fibers and the lignin make wood strong and stiff.

Fibrous reinforcement is very effective because many materials are much stronger and stiffer in fiber form than they are in bulk form. This phenomenon was probably first demonstrated scientifically in 1920 by Griffith [3], who measured the tensile strengths of glass rods and glass fibers of different diameters. Griffith found that as the rods and fibers got thinner, they got stronger, see Figure 1.2. This apparently is because the smaller the diameter, the smaller the likelihood that failure-inducing surface cracks would be generated during fabrication and handling. By extrapolating these results, Griffith found that for very small diameters the fiber strength approached the theoretical cohesive strength between adjacent layers of atoms whereas, for large diameters, the fiber strength dropped to near the strength of bulk glass.

Results similar to those published by Griffith have been reported for a wide variety of other materials. The reasons for the difference between fiber and bulk behavior, however, are not necessarily the same for the other materials. For example, polymeric fibers are stronger and stiffer than bulk polymers because polymer chains in the fiber are highly aligned and extended, while, in the bulk polymers the polymer chains are randomly oriented. A similar effect occurs in crystalline materials such as graphite. In

addition, a single crystal, which is very small in diameter and very long, tends to have a lower dislocation density than a polycrystalline solid, so single crystal "whisker" materials are much stronger than the same material in polycrystalline bulk form. Indeed, "whiskers" are currently the strongest reinforcing materials available.

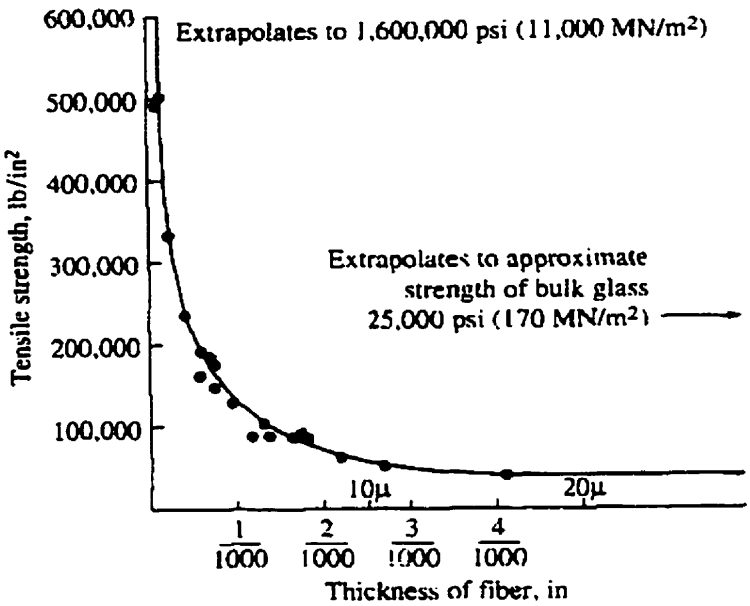

Figure 1.2. Griffith's measurements of tensile strength as a function of fiber thickness for glass fibers [3]

Although fibers allow us to obtain the maximum tensile strength and stiffness of a material, there are obvious disadvantages of using a material in fiber form. Fibers alone cannot support longitudinal compressive loads and their transverse mechanical properties are generally not so good as the corresponding longitudinal properties. Thus fibers are generally useless as structural materials unless they are held together in a structural unit with a binder or matrix material. Transverse reinforcement is generally provided by

orienting fibers at various angles according to the stress field in the structure of interest. The matrix also provides protection for fibers from environmental attacks and external damage.

Composites have many mechanical characteristics that are different from metals, polymers, and ceramics. The most important properties of composites are their inhomogeneity and anisotropy. An inhomogeneous body has nonuniform properties over the body, i.e., the properties depend on the position in the body. An anisotropic body has material properties that are different in all directions at a point in the body. For polymer matrix composites, along the fiber direction, it is stiff and strong but this is not so in the transverse direction. Tensile strengths in the longitudinal and transverse directions can differ by at least one order of magnitude; often much more. This is known for wood, which shows less extreme differences than for celery, and for banana skins. They are easily split in the longitudinal direction, and show substantial pull-out of fibers when any attempt is made to try to break them by applying longitudinal loads, see Figure 1.3 and 1.4.

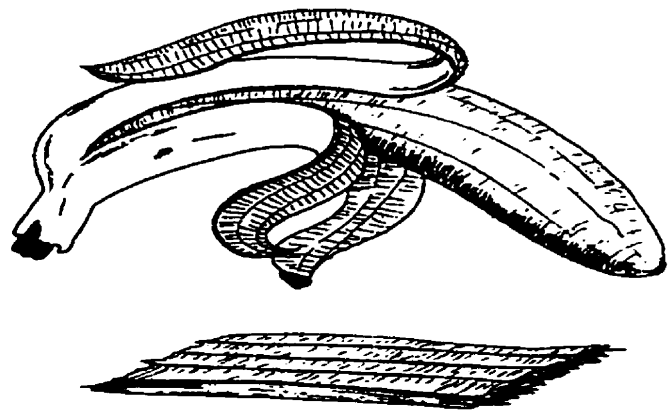

Figure 1.3. Longitudinal and transverse failure in a banana skin

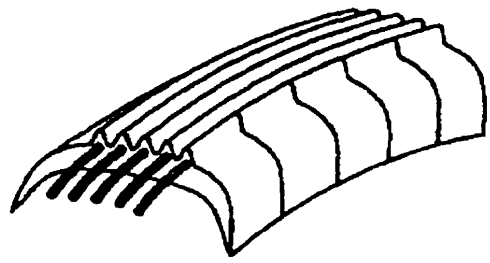

Figure 1.4. Fiber failure in a celery section

The need for fiber placement in different directions, according to a particular application, has led to various types of composites: continuous fiber composites, woven fiber composites, chopped fiber composites, and hybrid composites. In the continuous fiber composite laminate, individual continuous fiber/matrix laminae are oriented in the required directions and bonded together to form a laminate. This is used extensively in the aerospace industry and other industries where high performance is required. Most woven fiber composites have balanced properties in both fiber directions. It is easier to process them. As the fibers are not as straight as in the continuous fiber laminate, some strength and stiffness are sacrificed. Chopped fiber composites are cheap so they are used extensively in high volume applications. But their mechanical properties are poorer than those of continuous fiber composites. Hybrid composites may consist of mixed fiber types such as glass/graphite or mixed chopped fibers and continuous fibers. The design flexibility offered by these and other composite configurations is obviously quite attractive to designers, and the potential now exists to design not only the structure, but also the structural material itself.

1.1.2. Constituent Materials and Manufacturing of Composites

Glass fibers consist primarily of silica (silicon dioxide) and metallic-oxide-modifiers. The fibers are generally produced by the mechanical drawing of molten glass through small orifices. E-glass accounts for most glass fiber production and is the most widely used. S-glass, which has about 30% greater tensile strength and 20% greater modulus of elasticity than E-glass, is not as widely used as E-glass because of its higher cost. S-glass actually has greater strength than most advanced fibers, but its relatively low modulus limits its application.

Carbon fibers are the most widely used advanced fibers. Carbon/epoxy composites are now used routinely in aerospace structures. These fibers are usually produced by subjecting organic precursor fibers, such as polyacrylonitrile (PAN) or rayon, to a sequence of heat treatments, so that the precursor is converted to carbon by pyrolysis. The higher treatment temperature results the higher carbon contains in the fiber. Table 1.2 [4] lists the properties of some fibers and bulk metals.

Aramid polymer fibers, produced primarily by E. I. Du Pont de Nemours & Company under the trade name "Kevlar®", were originally developed for use in radial tires. Kevlar®29 is still used for this purpose. A higher modulus version, Kevlar®49, is extensively used in structural composites. Its density is about half that of glass and its specific strength is among the highest of currently available fibers. Kevlar® 49 also has excellent toughness, ductility, and impact resistance.

Boron fibers are composites consisting of boron coating on a tungsten or carbon substrate. The diameter of a boron fiber is among the largest of all the advanced fibers, typically 0.05-0.2 mm. Boron fibers have much higher strength and stiffness than carbon fibers. They also have higher density. Boron/epoxy and boron/aluminum composites are widely used in aerospace structures, but their high cost still prevents more widespread use.

Polymers, metals, and ceramics are all used as matrix materials in composites, depending on the particular requirements. The matrix holds the fibers together in a structural unit and protects them from external damage, transfers and distributes the applied loads to the fibers, and in many cases contributes some properties such as ductility, toughness, or electrical insulation. A strong interface bond between the fiber and matrix is desirable in polymer composites, so the matrix must be capable of developing a mechanical or chemical bond with the fiber or achieving so by a interface. The fiber and matrix should also be chemically compatible, especially under high temperature.

Polymers are the most widely used matrix materials in advanced composites. Both thermosets (e.g., epoxy, polyester, phenolic) or thermoplastics (e.g., polyimide (PI), polysulfone (PS), polytheretherketone (PEEK), polyphenylene sulfide (PPS)) are widely used. Upon curing, thermosets form a highly cross-linked, three dimensional molecular network which does not melt at high temperature. Thermoplastics are based on polymer

chains which do not cross-link. As a result, a thermoplastic will soften and melt at high temperature, then harden again upon cooling.

Table 1.2 Selected properties of fibers and bulk metals [4]

Material	Tensile strength (GPa)	Tensile modulus (GPa)	Density (g/cm^3)
Bulk 6061T6 (Aluminum)	0.31	0.7	2.71
Bulk SAE4340 (Steel)	1.03	0.2	7.83
Glass Fibers			
E-Glass Fibers	3.45	0.07	2.54
S-Glass Fibers	4.48	0.09	2.49
Carbon fibers (PAN Precursor)			
AS-4 (Hercules)	4.00	0.23	1.80
IM-7 (Hercules)	5.41	0.28	1.77
T-300 (Amoco)	3.65	0.23	1.77
T-650/42 (Amoco)	5.03	0.29	1.77
Carbon fibers (pitch precursor)			
P-55 (Amoco)	1.72	0.38	1.99
P-75 (Amoco)	2.07	0.52	1.99
P-100 (Amoco)	2.24	0.69	2.16
Aramid fibers			
Kevlar®29 (Dupont)	3.79	0.06	1.44
Kevlar®49 (Dupont)	3.79	0.13	1.47
Boron fibers			
0.1 mm diameter (Textron)	3.51	0.40	2.57
1.4 mm diameter (Textron)	3.51	0.40	2.49

Epoxies and polyesters have been the principal polymer matrix materials for several decades, but advanced thermoplastic such as PEEK and PPS are receiving

considerable attention for their excellent toughness and low moisture absorption. Aerospace grade epoxies are typically cured at about 177^0C and generally not used above 150^0C. For higher temperatures, PI can be considered.

By using lightweight metals, such as aluminum, titanium, and magnesium, and their alloys, as matrix materials, the composites can be used under high temperatures. For example titanium can be used up to 1250^0C. Other advantages of metal matrices are their higher strength, stiffness, and ductility compared to polymers, at the expense of higher density. Ceramic matrix materials such as silicon carbide and silicon nitride can be used at temperatures of up to 1650^0C. Ceramics have poor tensile strength and are notoriously brittle. There is a need for further research before the materials can be routinely used. Carbon/carbon composites can be used at temperatures approaching 2760^0C, if there is no oxidization. The cost of such materials is very high and they are only used in a few critical aerospace applications.

With composites we design and build not only the structure but also the structural material itself. The selection of a fabrication process is important and depends on the constituent materials in the composite, with the matrix material being the key. Only a few fabrication processes for polymer matrices are mentioned here. Components in the form of panels can be formed with heat and pressure using autoclave or hot press molding. Figure 1.5 shows an autoclave the author used. Structure components, with constant cross-section such as rods, tubes or beams, can be formed by pultrusion, where continuous reinforcements impregnated with resin are pulled through a heated die.

Filament winding, where continuous reinforcement impregnated with resin is wound onto a mandrel at specific angles, is useful in producing vessels or other hollow structures; see Figure 1.6. For thin structures with complex shapes, hand lay-up of prepregs is still used despite the high labour cost. In the case of thicker and more complex structures, resin transfer moulding (RTM) is used to force the resin into pre-shaped fiber preforms. For short fiber composites, hot press moulding is used for relatively simple shapes while injection moulding is used to produce more complex structures. Figure 1.7 shows composite processing maps which address the concerns of polymer matrix, reinforcement aspect ratio and its orientation in the final structure. The part complexity as well as production volume are also considered [5].

1.1.3. Applications

Composite structural elements are now used in a variety of components for aerospace, automotive, marine, and architectural structures in addition to consumer products such as skis, golf clubs, and tennis rackets. Since much of the advanced composite technology evolved from aerospace applications, it is appropriate to start an overview there.

Figure 1.5. An autoclave with a molded C/E panel

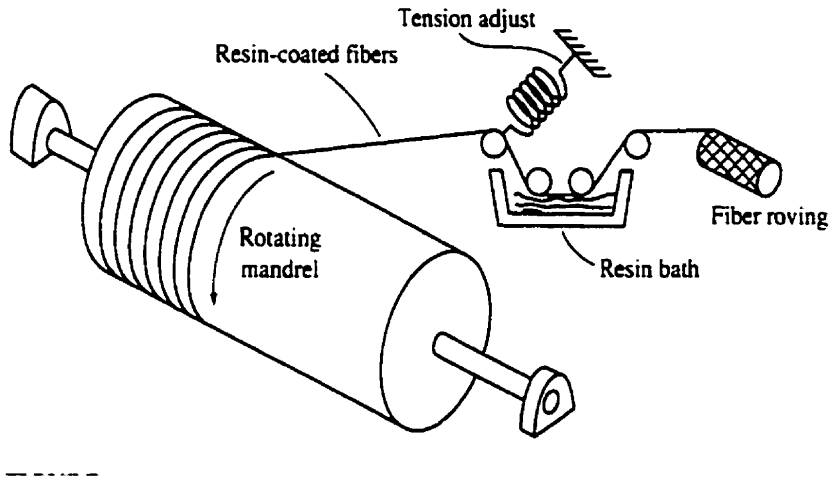

Figure 1.6. Filament winding process

Military aircraft designers were among the first to realize the tremendous potential of composites with high specific strength and high specific stiffness since performance and maneuverability of those aircrafts depend so heavily on weight. Composite construction also leads to smooth surfaces (no rivets or sharp transitions as in metallic construction) which reduce drag. The general Dynamics F-111 wing-pivot fitting was the first part which used a boron/epoxy "band-aid" to reduce the stress level [6].

(a)

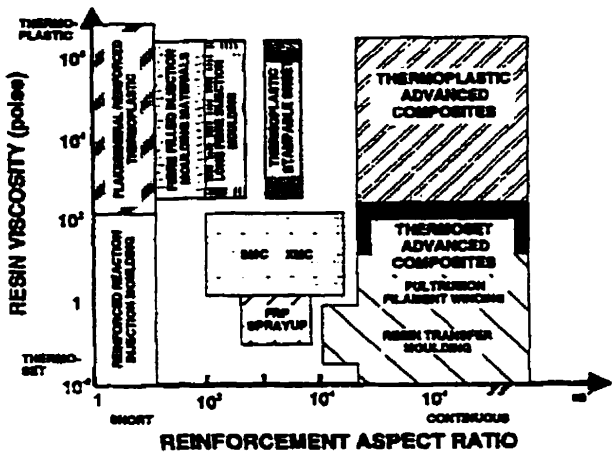

(b)

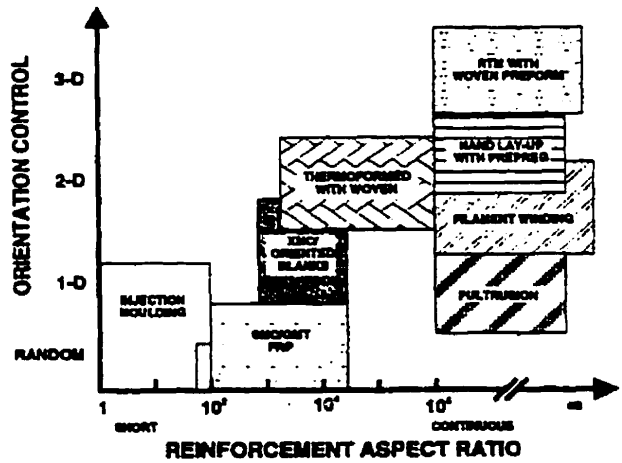

(c)

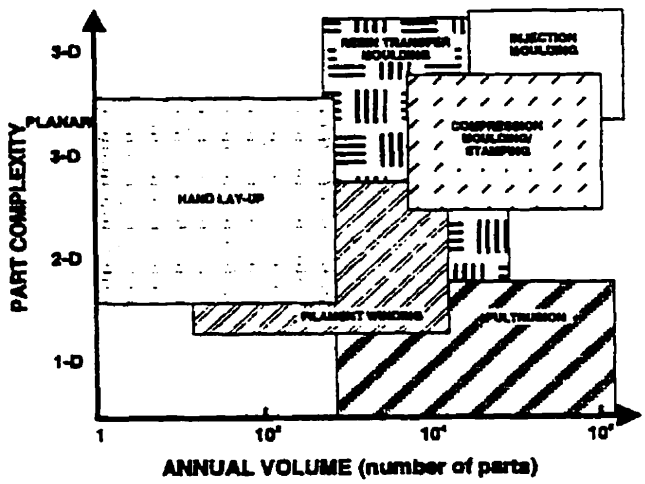

Figure 1.7 Composite processing maps: (a) materials (b) orientation (c) volume [5]

Composite structural elements, such as horizontal and vertical stabilizers, flaps, wing skins, and various control surfaces, have been used in fighter aircraft such as the F-14, F-15, and F-16 with a typical weight saving of about 20%. The AV-8B has more composite parts which reduce its weight by 26%. Figure 1.8 shows composite materials used on the F-18C/D which save 35% of the weight. One of the most demanding applications thus far is the use of a graphite/epoxy composite wing structures on the forward-swept wing X-29A fighter from Grumman, see Figure 1.9. Although the concept of a forward-swept wing for improved maneuverability is not new, conventional aluminum structures could not withstand the aerodynamic force acting on such a wing, so the implementation of the concept had to wait for the development of advanced composites. The Northrop Grumman B-2 Stealth Bomber, see Figure 1.10, has most external parts are made from various composite materials. This is because of its radar-absorption. Furthermore it can be formed into shapes that naturally lower the radar cross section. However the details are not publicly available.

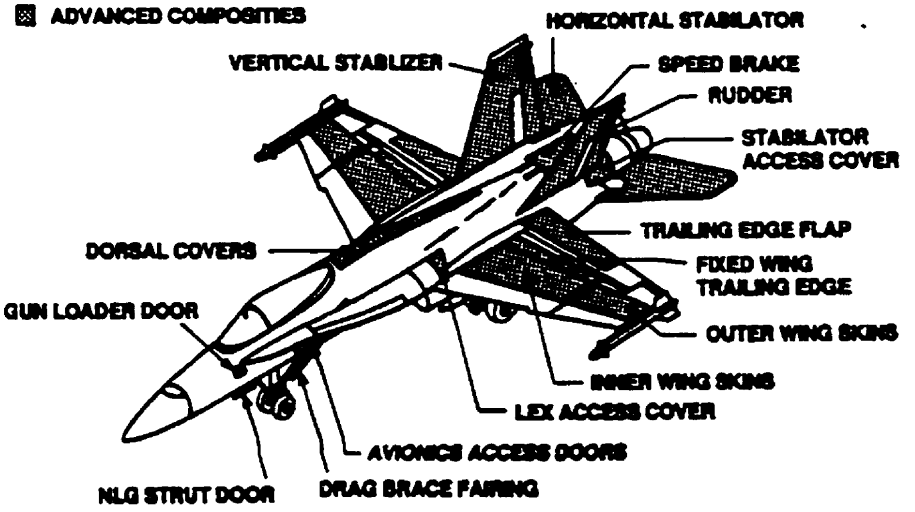

Figure 1.8. F-18C/D composite materials usage

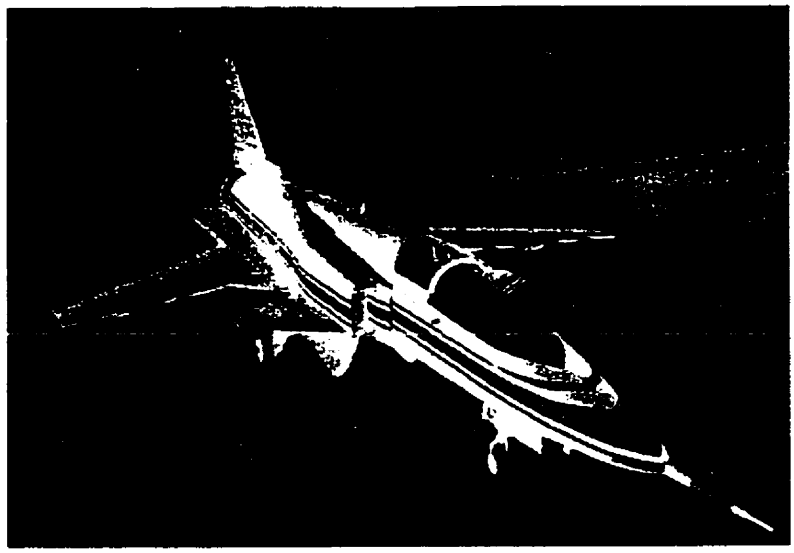

Figure 1.9. Grumman X-29A

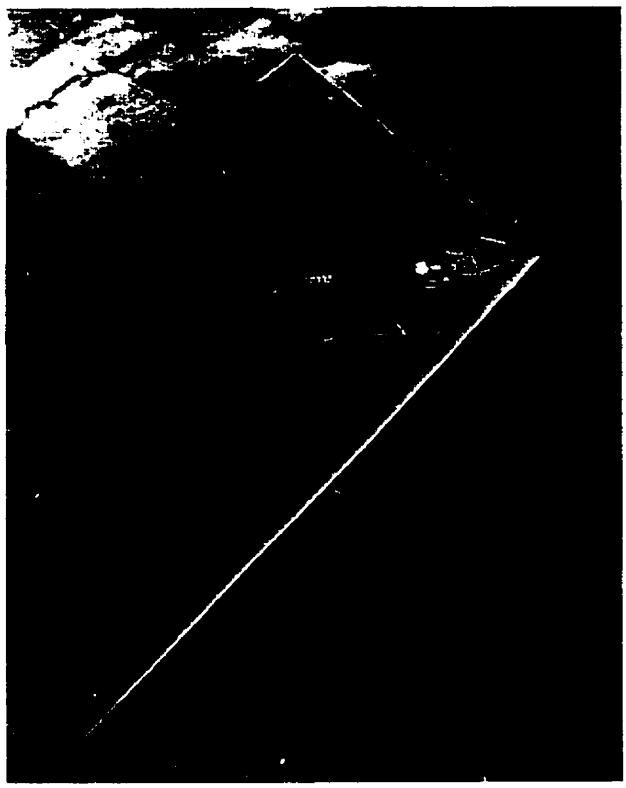

Figure 1.10. B-2 Stealth Bomber

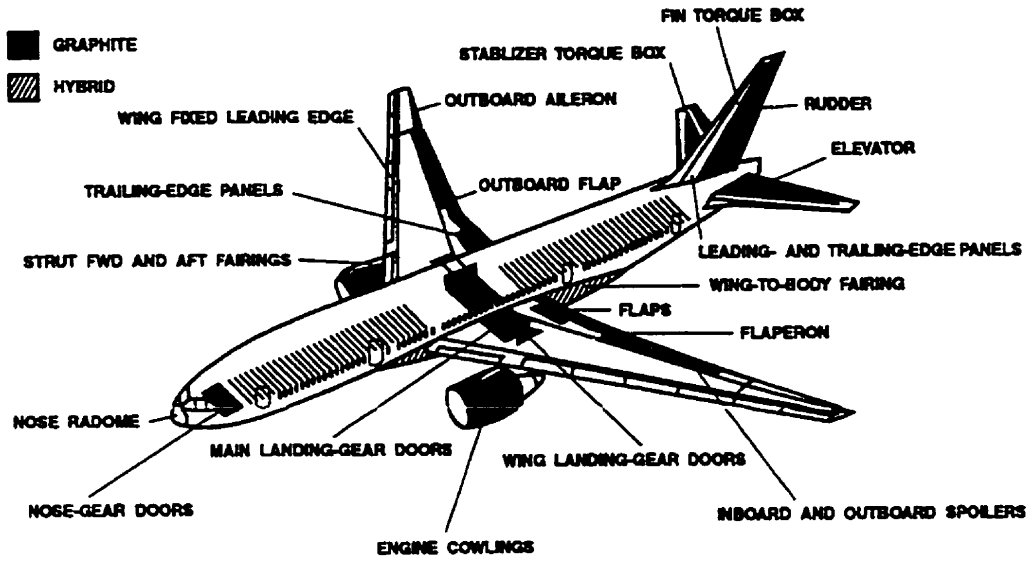

Figure 1.11. Boeing 777 (Hybrid is glass and carbon.)

Composite applications in commercial aircraft have been steadily increasing as material costs come down, as design and manufacturing technology evolves, and as the experience with composites in aircraft continues to increase. The Boeing 757 and 767 were among the first commercial airliners to make extensive use of composites. The Boeing 757 used about 1,350 kg composites, and about 30% of the external surface of the Boeing 767 consists of composites. Figure 1.11 shows composites, about 8,400 kg, used on the Boeing 777 for both primary structure (a first for Boeing) and secondary structure for a total of 10% of the structure weight.

Due to the tremendous cost per unit weight to place an object in space, the value of weight saved is even greater for spacecraft than for aircraft. Thus, composites are extremely attractive for spacecraft. The NASA Space Shuttle has a number of composite parts, including graphite/epoxy cargo bay doors and an experimental graphite/epoxy solid

rocket booster motor case. Some graphite/epoxy structures can be tailored to have a zero coefficient of thermal expansion. This is a big advantage for large antennas that must pass in and out of the sun, and yet maintain dimensional stability for accuracy of pointing the signal. For example, a graphite/epoxy truss is used to stabilize and support the Hubble Space Telescope.

To reduce weight and increase average gas mileage from the current 11.7 km/l to 34 km/l is the main reason for using composites in automotive applications. The attempts started with Henry Ford's "corn cob car" in the late 1930's. Since then, progress has been made year by year. Although the bottlenecks are still the cost of the composite materials and the slow manufacture process, compared with the metal stamping in the car industry, there are some parts which have survived, such as leaf springs, and drive shafts. The achievement of the goal for composite car relies on the breaking of the bottlenecks.

Composites are also increasingly used as surgical implants in medical applications due to their lightweight, chemical inertness, and the ease of fabrication. Figure 1.12 shows a leg brace designed and fabricated by the author in which carbon reinforced polypropylene was used.

Figure 1.12. Carbon/PP leg brace

Composite materials found their way into commercial applications very quickly when costs were controlled or were not an issue. Fiberglass fishing rods, for example, were produced in the 1940s and became a standard by the 1960s. Many other fiberglass products, such as boats, cars to a limited extent, tennis rackets, skis, and surfboards, became popular. Costly fibers such as the boron, and carbon are used in golf clubs and tennis rackets. In fact, the early use of carbon in golf clubs was a significant factor in enhanced use in military aircraft because the increased production volume reduced the carbon fiber cost for all users. Carbon/epoxy is quite effective in reinforcing already built columns of bridges in seismically active regions such as Japan. More and more applications will occur as the world's inventors use their imagination and cunning to improve old products and create new products.

1.2. Composite Stiffness and Strength

The mechanical properties of the fiber laminates are quite different from isotropic homogeneous materials. This is because of the strongly directional nature of the mechanical properties of the layers, and because of the complex interactions between the layers [7]. In connection with this, special effects can occur which are not very important in homogeneous materials, such as free-edge effects, which give highly localized interlaminar stress. Here we shall review some experimental evidence of measurement of laminate properties in terms of stiffness and strength. In sections 1.3 to 1.6, we shall also present the classical lamination theory, the laminate failure criteria, the edge effect, and the principle of photoelastic measurement required for an understanding of the experimental results and the theoretical development.

1.2.1. Measurement of Composite Elastic Constants with Flat Specimens

The test methods for composites are developed from those used for isotropic materials. Earlier work done by Tsai [8], see Figure 1.13, which has been widely cited, used very long and narrow specimens (63 mm gauge length and 4.6mm width) to test the composite tensile elastic constants and strength. Ever since then long and narrow specimens have been widely used to test laminate tensile properties. In the recent ASTM standard D 3039/D 3039M -95a, a long and narrow specimen (150mm gauge length and 25mm width) is used for determining the in-plane tensile properties of a polymer matrix

composite reinforced by high-modulus fibers with balanced and symmetric laminae [9]. With such a specimen shape the edge effect may be important.

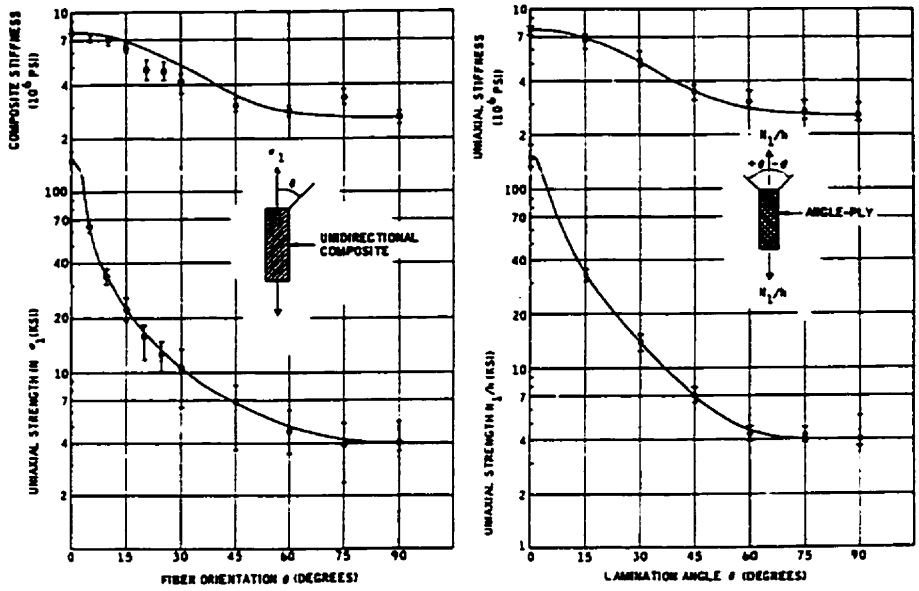

Figure 1.13. Tsai's results of stiffness and strength for glass/epoxy [8]

For example, Kress [10] measured carbon/epoxy "long" samples with different widths, which varied from 6mm to 20mm. The lay-up sequences he used were two groups of $[0_a/90_b]_s$, $[(\pm 15)_a/90_b]_s$, $[(\pm 30)_a/90_b]_s$, $[(\pm 45)_a/90_b]_s$, where a = 2, b = 1 and a =4, b = 2, and another reversed sequence group of $[90_b/0_a]_s$, $[90_b/(\pm 15)_a]_s$, $[90_b/\pm 30)_a]_s$, $[90_b/(\pm 45)_a]_s$, where a = 2 and b =1. He found that all the stiffness results were below the classical lamination theory (see Section 1.3) prediction. The stiffness decreased progressively with the reduction of sample width. The 15^0 and 45^0 laminates had the largest stiffness reductions, about 22% less than the classical lamination theory prediction.

The composite elastic constants can only be measured correctly if a good experiment is carried out. Hine et al [11,12] used ultrasonic velocity measurements to determine Poisson's ratios for carbon/epoxy and glass/epoxy angle-ply laminates. They measured the angle-ply laminate stiffness constants by means of measuring time of flight for a 2.25 MHz sound pulse to travel through the sample. Their results agreed very well with the classical lamination theory. Figure 1.14 shows their Poisson's ratio result for carbon/epoxy in which the Poisson's ratio approached two in the lay-up $[\pm 20]_{2s}$.

Khatibzadeh and Piggott tested $[\pm 45]_s$ carbon/epoxy and glass/epoxy laminates with different gauge length to width aspect ratios [13]. They found that the laminate stiffness increased with the decrease of the aspect ratio, see Figure 1.15.

The free edge effect due to interlaminar stress will be discussed later (section 1.5). This effect has been noticed earlier and treated theoretically [14-17]. Closed-forms or numerical solutions to evaluate the stiffness under the free edge effects have been developed.

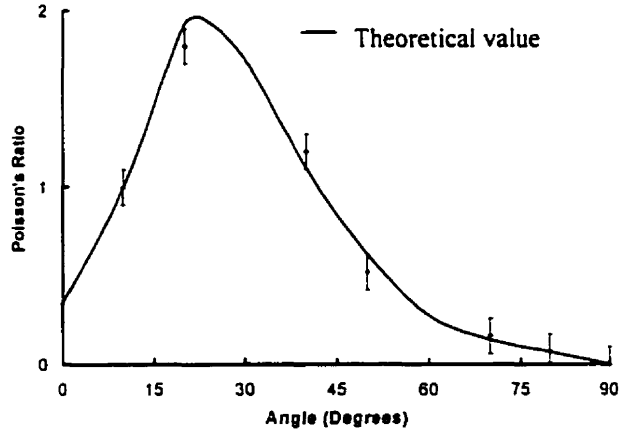

Figure 1.14. Poisson's ratio tested by Hine et al [11,12]

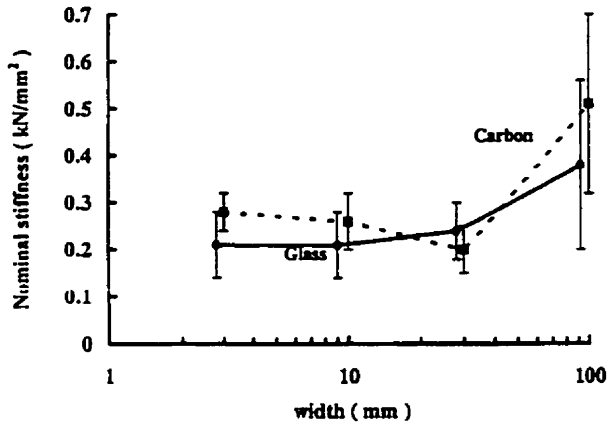

Figure 1.15. Stiffness versus specimen width for glass and carbon $[\pm 45]_s$ laminates [13]

1.2.2 Measurement of Composite Strength with Flat Specimens

Snell used angle ply laminates to test carbon/epoxy strength [18]. The specimens he used were 20 mm gauge length and 20 mm width. He obtained higher strengths than that Tsai-Wu failure criterion (see Section 1.4) predicted. His work seems to have been ignored.

Sun and Quinn [19] found that interactive criteria, such as Tsai-Wu criterion, can significantly underestimate ultimate laminate failure.

Khatibzadeh and Piggott [20] found that $[\pm\phi]_s$ angle-ply laminates could be five times stronger than that predicted by the Tsai-Hill criterion and the maximum stress criterion, if moderately wide and short specimens were used. They also observed that the

strength increased with increasing of specimen width. They developed an equation to calculate the angle-ply laminate strength. This was:

$$\sigma_{u\phi} = \sigma_{1\phi}(1 - \frac{\tan\phi}{\tan\phi_0}) + \frac{\tau_{12u}}{\cos^2\phi\tan\phi_0} \qquad (1.1)$$

where $\sigma_{u\phi}$ is the laminate strength, σ_{1f}=σ_{1u} and τ_{12u} are the lamina longitudinal tensile and shear strengths respectively, and ϕ is the lay-up angle. $\phi_0 \le \phi_c = \arctan(\frac{W}{L})$, W is specimen width, L is specimen gauge length. They found ϕ_0=48^0 for their specimens.

1.2.3. Measurement of the Composite Properties with Tubular Specimens

Soden et al [21-23] used E-glass/epoxy tubes with $[\pm 15]_s$, $[\pm 35]_s$, and $[\pm 45]_s$ lay-ups to test the composite elastic constants and strengths under uniaxial and biaxial loads. The specimen they used was 300 mm long with 100 mm internal diameter and 60 mm gauge length. They claimed the moduli agreed with classical lamination theory. Their Poisson's ratios were less than the theory prediction. Their testing results are shown in Figures 1.16 and 1.17.

Based on previous numerical analysis done by Whitney and Pagano, and Daniel [24-26], Toombes and Swanson [27] designed and analyzed a tubular specimen which was modified later by Smith and Swanson [28]. They believed their specimen avoided the

stress concentration due to the end effect, generated by clamps, and provided a uniform stress in the gauge area. The tube had thickened ends so it could be used for both hoop

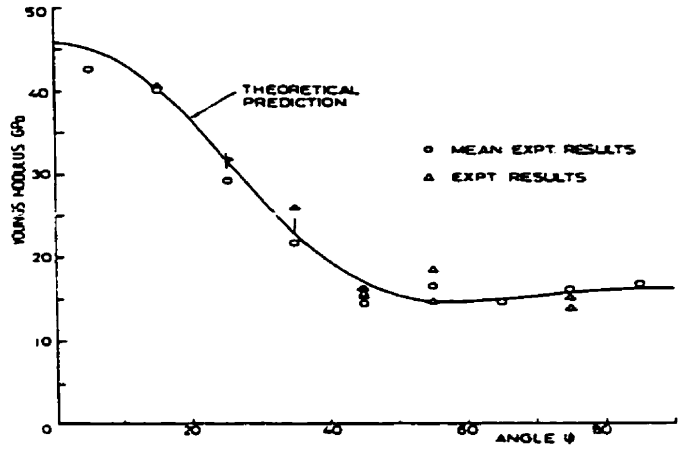

Figure 1.16. Stiffness results of Soden et al [21-23]

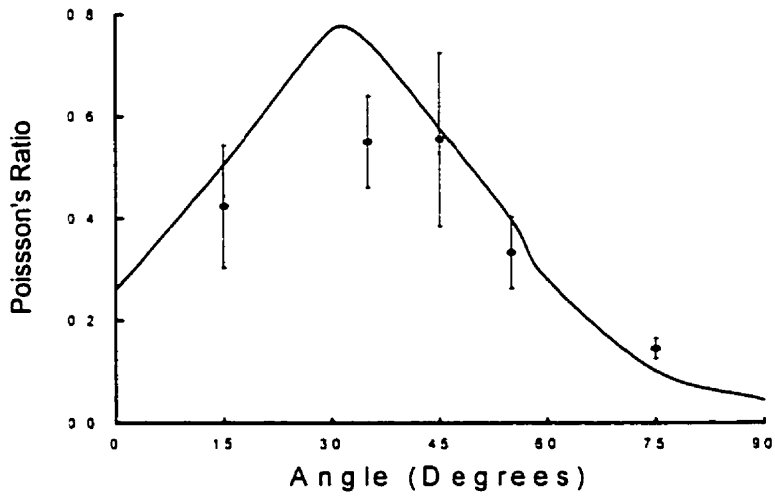

Figure 1.17. Poisson's ratio results of Soden et al [21-23]

and axial loading and for biaxial loading. The internal diameter of the specimen was 96 mm. Different lay-ups were used which gave different wall thickness. The length of the tube changed a little between the early work and the later work. Dimensions of the latest

specimen are shown in Figure 1.18. In this section the 0^0 refers to the tube hoop direction, which is denoted by x. The y refers to the tube longitudinal direction.

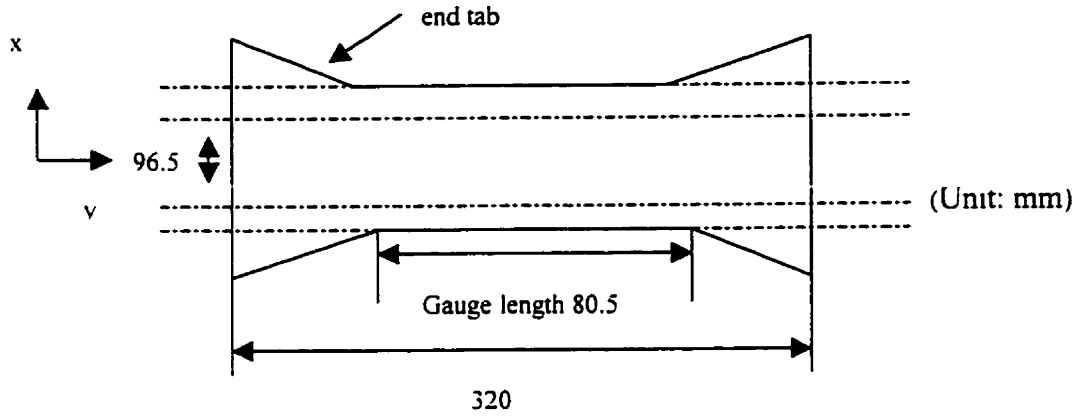

Figure 1.18. Tubular specimen used by Swanson

They [29-34] tested carbon/epoxy tubes with the lay-ups of $[0/\pm45/90]_{ns}$, $[0_3/\pm45/90]_{ns}$, $[0/(\pm45)_2/90]_{ns}$, $[90/\pm45/0]_{ns}$, $[0/\pm60]_{ns}$, $[\pm45]_{2s}$, and $[0]_n$, where n is one, two, or three. The loads they used were internal pressures plus an axial force. They normally used 3 strain gauge rosettes located at the axial mid-plane and spaced around the circumference. Each strain gauge rosette had three strain gauges stacked together at 0^0, 90^0, and 45^0. The average reading was taken from the three rosettes.

About 60% of their laminate tube stiffnesses agreed with the classical lamination theory, as can be seen in table 1.3. In table 1.3 the $\overline{Q}_x$, $\overline{Q}_y$, *and* G_{xy} are the sample stiffness in x, y directions and shear modulus respectively. Swanson reported no Poisson's ratios.

Tennyson et al [35, 36] used $[\pm\phi]_s$ glass/epoxy and carbon/epoxy tubes to test the laminate strengths under biaxial loading. They found the composite tube failure pressures were much higher than the prediction from the Tsai-Wu criterion. They developed a cubic model to predict the laminate strength and the model fitted their experimental data better than the Tsai-Wu criterion.

Soden et al 's [21-23] strength results showed that the angle ply laminate strength could be five times higher than those predicted by the Tsai-Wu criterion.

Swanson et al's [29-34] results showed that the Tsai-Wu criterion did not agree at all with the experimental data. The measured strengths from tubular specimens were much higher than those predicted by the Tsai-Wu criterion. They claimed that, in general, the maximum strain generated in longitudinal tensile flat coupon tests could be used as a failure criterion. Because of the low in-plane minor Poisson's ratio, using the maximum stress instead gaves essentially the same prediction.

Bai et al [37-39] used glass/epoxy $[\pm 35]_n$ filament wound tube to study the composite mechanical behavior and damage mechanisms. They also found the tubes were much stronger than that predicted by Tsai-Wu criterion prediction. Their results agreed with Soden et al's [21-23].

Table 1.3. Stiffness of C/E laminates (GPa) measured by Swanson et al [28-33]

Materials	Lay-ups	$\overline{Q}_x$	$\overline{Q}_y$	G_{xy}	$\overline{Q}_{xth}$	$\overline{Q}_{yth}$	G_{xyth}
AS4/3501-6	$[0/\pm60/0]_s$	65±2	52±1	15±1	68	51	18
	$[0/\pm45/90]_s$	49±3.5	55±2	-	57	57	-
	$[22.5/67.5/-22.5/-67.5]_s$	51±3	53±2	-	57	57	-
	$[11.25/56.25/-33.75/-78.75]_s$	51±2	53±3	-	57	57	-
T800/3900-2	$[0/\pm45/90]_{ns}$	64	65	20.2	65	65	20
	$[0_3/\pm45/90]_{ns}$	94	45	13	95	46	14
	$[0/(\pm45)_2/90]_{ns}$	57	54	23	59	59	26
AS4, s-glass/55A	$[\pm45_{gr}/0_{gr}/90_{gl}/0_{gr}/90_{gl}]_T$	29±2	55±2.9	6.5±0.8	30	53	7
AS4/55A	[0]	135±9.5	9.5±0.4	3.3±0.2	138	8	2

Note: x: Hoop direction, y: Longitude direction

$_{th}$: Theoretical data from the classical laminate plate theory (gr: graphite AS4, gl: S-glass)

No standard deviation for the T800/3900-2. We could assume for the for $\overline{Q}$ it is ±3, and for G it is ±1.

1.3 Classical Lamination Theory

1.3.1 Lamina Stress-strain Behavior

The generalized Hook's law relating stresses to strains can be written in contracted notation as:

$$\sigma_i = C_{ij}\varepsilon_j \qquad i, j = 1,\ldots\ldots 6 \qquad (1.2)$$

where σ_i are the stress components shown on a 3-dimention cube in x, y, z, coordinates, see Figure 1.19.

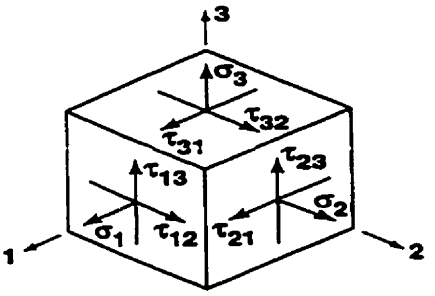

Figure 1.19. Stresses on an element

C_{ij} is the stiffness matrix, and ε_j are the strain components. The strains are defined by:

$$\varepsilon_1 = \frac{\partial u}{\partial x} \qquad \varepsilon_2 = \frac{\partial v}{\partial y} \qquad \varepsilon_3 = \frac{\partial w}{\partial z} \qquad (1.3)$$

$$\gamma_{23} = \frac{\partial v}{\partial x} + \frac{\partial w}{\partial y} \qquad \gamma_{31} = \frac{\partial w}{\partial x} + \frac{\partial u}{\partial z} \qquad \gamma_{12} = \frac{\partial u}{\partial y} + \frac{\partial v}{\partial x}$$

where u, v, w are displacements in the x, y, z directions or the 1, 2, 3 directions.

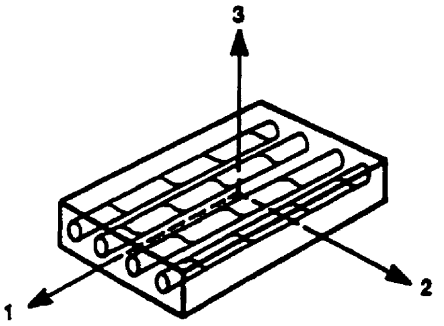

Figure 1.20. Unidirectional reinforced lamina

If we consider a plane stress condition, and put a lamina longitudinal direction along the 1 direction, as shown in Figure 1.20, then

$$\begin{bmatrix} \varepsilon_1 \\ \varepsilon_2 \\ \gamma_{12} \end{bmatrix} = \begin{bmatrix} S_{11} & S_{12} & 0 \\ S_{12} & S_{22} & 0 \\ 0 & 0 & S_{66} \end{bmatrix} \begin{bmatrix} \sigma_1 \\ \sigma_2 \\ \sigma_3 \end{bmatrix} \tag{1.4}$$

where S_{ij} are the compliance, that is:

$$[S_{ij}] = \begin{bmatrix} \frac{1}{E_1} & \frac{-\nu_{21}}{E_2} & 0 \\ \frac{-\nu_{12}}{E_1} & \frac{1}{E_2} & 0 \\ 0 & 0 & \frac{1}{G_{12}} \end{bmatrix} \tag{1.5}$$

in which:

E_1, E_2 are lamina Young's (extension) moduli in the 1, 2 directions. ν_{ij} are the Poisson's ratio (extension-extension coupling coefficient),

that $\nu_{ij} = \frac{\varepsilon_j}{\varepsilon_i}$ for $\sigma_i = \sigma$ and all other stresses are zero. and G_{12} is the shear modulus in the 1-2 plane.

Equation 1.4, the strain-stress relations, can be inverted to obtain the stress-strain relations

$$\begin{bmatrix}\sigma_1\\ \sigma_2\\ \tau_{12}\end{bmatrix}=\begin{bmatrix}Q_{11} & Q_{12} & 0\\ Q_{12} & Q_{22} & 0\\ 0 & 0 & Q_{66}\end{bmatrix}\begin{bmatrix}\varepsilon_1\\ \varepsilon_2\\ \gamma_{12}\end{bmatrix} \tag{1.6}$$

Where the Q_{ij} are the reduced stiffnesses for a plane stress state in the 1-2 plane, determined by

$$[Q_{ij}]=[S_{ij}]^{-1} \tag{1.7}$$

or

$$Q_{11}=\frac{S_{22}}{S_{11}S_{22}-S_{12}^{\ 2}}=\frac{E_1}{1-\nu_{12}\nu_{21}} \qquad Q_{22}=\frac{S_{11}}{S_{11}S_{22}-S_{12}^{\ 2}}=\frac{E_2}{1-\nu_{12}\nu_{21}}$$

$$Q_{12}=\frac{S_{12}}{S_{11}S_{22}-S_{12}^{\ 2}}=\frac{\nu_{12}E_2}{1-\nu_{12}\nu_{21}}=\frac{\nu_{21}E_1}{1-\nu_{12}\nu_{21}} \tag{1.8}$$

$$Q_{66}=\frac{1}{S_{66}}=G_{12}$$

When the stresses and strains were are applied at an angle ϕ to the principal material directions, as shown in Figure 1.21, then a method of transforming stress-strain relations from one coordinate system to another is needed.

The transformations are commonly written as

$$\begin{bmatrix}\sigma_x\\ \sigma_y\\ \tau_{xy}\end{bmatrix}=[T]^{-1}\begin{bmatrix}\sigma_1\\ \sigma_2\\ \tau_{12}\end{bmatrix} \qquad \text{and} \qquad \begin{bmatrix}\varepsilon_x\\ \varepsilon_y\\ \frac{\gamma_{xy}}{2}\end{bmatrix}=[T]^{-1}\begin{bmatrix}\varepsilon_1\\ \varepsilon_2\\ \frac{\gamma_{12}}{2}\end{bmatrix} \tag{1.9}$$

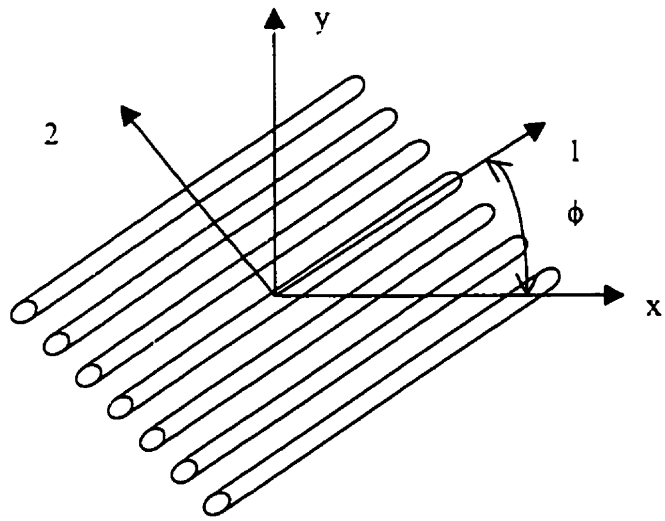

Figure 1.21. Positive rotation of material axes from x-y axes

where

$$[T]=\begin{bmatrix}\cos^2\phi & sin^2\phi & 2\sin\phi\cos\phi\\ \sin^2\phi & \cos^2\phi & -2\sin\phi\cos\phi\\ -\sin\phi\cos\phi & \sin\phi\cos\phi & \cos^2\phi-\sin^2\phi\end{bmatrix} \tag{1.10}$$

Then the stress-strain relations in x-y coordinates are

$$\begin{bmatrix}\sigma_x\\ \sigma_y\\ \tau_{xy}\end{bmatrix}=[\overline{Q}]\begin{bmatrix}\varepsilon_x\\ \varepsilon_y\\ \gamma_{xy}\end{bmatrix}=\begin{bmatrix}\overline{Q}_{11} & \overline{Q}_{12} & \overline{Q}_{16}\\ \overline{Q}_{12} & \overline{Q}_{22} & \overline{Q}_{26}\\ \overline{Q}_{16} & \overline{Q}_{26} & \overline{Q}_{66}\end{bmatrix}\begin{bmatrix}\varepsilon_x\\ \varepsilon_y\\ \gamma_{xy}\end{bmatrix} \tag{1.11}$$

in which

$$\begin{aligned}
\overline{Q}_{11} &= Q_{11}\cos^4\phi + 2(Q_{12}+2Q_{66})\sin^2\phi\cos^2\phi + Q_{22}\sin^4\phi\\
\overline{Q}_{12} &= (Q_{11}+Q_{22}-4Q_{66})\sin^2\phi\cos^2\phi + Q_{12}(\sin^4\phi+\cos^4\phi)\\
\overline{Q}_{22} &= Q_{11}\sin^4\phi + 2(Q_{12}+2Q_{66})\sin^2\phi\cos^2\phi + Q_{22}\cos^4\phi\\
\overline{Q}_{16} &= (Q_{11}-Q_{12}-2Q_{66})\sin\phi\cos^3\phi + (Q_{12}-Q_{22}+2Q_{66})\sin^3\phi\cos\phi\\
\overline{Q}_{26} &= (Q_{11}-Q_{12}-2Q_{66})\sin^3\phi\cos\phi + (Q_{12}-Q_{22}+2Q_{66})\sin\phi\cos^3\phi\\
\overline{Q}_{66} &= (Q_{11}+Q_{22}-2Q_{12}-2Q_{66})\sin^2\phi\cos^2\phi + Q_{66}(\sin^4\phi+\cos^4\phi)
\end{aligned} \tag{1.12}$$

The strain-stress relations are then

$$\begin{bmatrix}\varepsilon_x\\ \varepsilon_y\\ \gamma_{xy}\end{bmatrix}=[\overline{S}]\begin{bmatrix}\sigma_x\\ \sigma_y\\ \tau_{xy}\end{bmatrix}=\begin{bmatrix}\overline{S}_{11} & \overline{S}_{12} & \overline{S}_{16}\\ \overline{S}_{12} & \overline{S}_{22} & \overline{S}_{26}\\ \overline{S}_{16} & \overline{S}_{26} & \overline{S}_{66}\end{bmatrix}\begin{bmatrix}\sigma_x\\ \sigma_y\\ \tau_{xy}\end{bmatrix} \tag{1.13}$$

in which

$$\begin{aligned}
\overline{S}_{11} &= S_{11}\cos^4\phi + (2S_{12}+S_{66})\sin^2\phi\cos^2\phi + S_{22}\sin^4\phi\\
\overline{S}_{12} &= S_{12}(\sin^4\phi+\cos^4\phi) + (S_{11}+S_{22}-S_{66})\sin^2\phi\cos^2\phi\\
\overline{S}_{22} &= S_{11}\sin^4\phi + (2S_{12}+S_{66})\sin^2\phi\cos^2\phi + S_{22}\cos^4\phi\\
\overline{S}_{16} &= (2S_{11}-2S_{12}-S_{66})\sin\phi\cos^3\phi - (2S_{22}-2S_{12}-S_{66})\sin^3\phi\cos\phi\\
\overline{S}_{26} &= (2S_{11}-2S_{12}-S_{66})\sin^3\phi\cos\phi - (2S_{22}-2S_{12}-S_{66})\sin\phi\cos^3\phi\\
\overline{S}_{66} &= 2(2S_{11}+2S_{22}-4S_{12}-S_{66})\sin^2\phi\cos^2\phi + S_{66}(\sin^4\phi+\cos^4\phi)
\end{aligned} \tag{1.14}$$

Comparing equation 1.14 with equation 1.5, the engineering constants in x-y plane can be expressed as

$$\begin{aligned}
\frac{1}{E_x} &= \frac{1}{E_1}\cos^4\phi + \left[\frac{1}{G_{12}} - \frac{2\upsilon_{12}}{E_1}\right]\sin^2\phi\cos^2\phi + \frac{1}{E_2}\sin^4\phi \\
\upsilon_{xy} &= E_x\left[\frac{\upsilon_{12}}{E_1}\left(\sin^4\phi + \cos^4\phi\right) - \left(\frac{1}{E_1} + \frac{1}{E_2} - \frac{1}{G_{12}}\right)\sin^2\phi\cos^2\phi\right] \\
\frac{1}{E_y} &= \frac{1}{E_1}\sin^4\phi + \left(\frac{1}{G_{12}} - \frac{2\upsilon_{12}}{E_1}\right)\sin^2\phi\cos^2\phi + \frac{1}{E_2}\cos^4\phi \\
\frac{1}{G_{xy}} &= 2\left(\frac{2}{E_1} + \frac{2}{E_2} + \frac{4\upsilon_{12}}{E_1} - \frac{1}{G_{12}}\right)\sin^2\phi\cos^2\phi + \frac{1}{G_{12}}\left(\sin^4\phi + \cos^4\phi\right)
\end{aligned} \tag{1.15}$$

1.3.2 Laminated Plate Theory

The laminate is presumed to consist of perfectly bonded laminae. Moreover, the bonds are presumed to be infinitesimally thin as well as non-shear-deformable. That is the displacements are continuous across lamina boundaries so that no lamina can slip relative to another. Thus, the laminate acts as a single layer with very special properties that constitute a structure element.

If the laminate is thin, the Kirchhoff hypothesis for plates and the Kirchhoff-Love hypothesis for shells applied. These are that a line originally straight and perpendicular to the middle surface of the laminate, i.e., a normal to the middle surface, is assumed to remain straight and perpendicular to the middle surface when the laminate is deformed, e.g., bent, extended, contracted, sheared, or twisted. This means the shearing strains in

planes perpendicular to the middle surface is ignored, that is $\gamma_{xz}=\gamma_{yz}=0$, where z is the normal direction to the middle surface, see Figure 1.22. In addition, the normals are presumed to have constant length so that the strain perpendicular to the middle surface is ignored as well, that is $\varepsilon_z=0$.

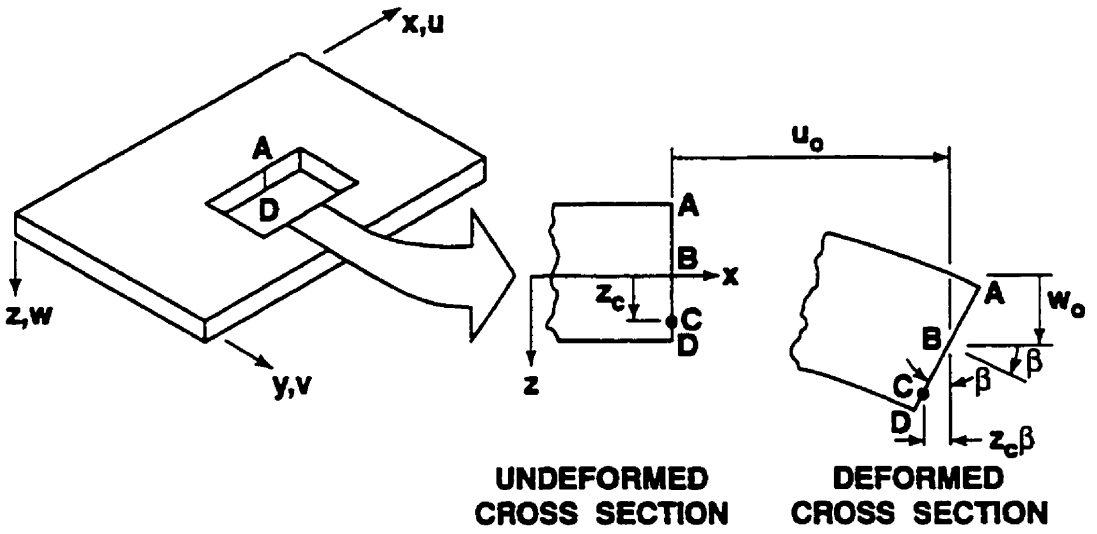

Figure 1.22 Geometry of deformation in the x-z plane [40]

The implications of the Kirchhoff hypothesis on the laminate displacements u, v, and w in the x, y, and z directions are derived by use of the laminate cross section in the x-z plane shown in Figure 1.22. The displacement in the x direction of point B from the undeformed middle surface to the deformed middle surface is u_0. The sub-note "0" here is used to designate middle-surface values of a variable. Because line ABCD remains straight under deformation of the laminate, the displacement at point C is

$$u_c = u_0 - z_c\beta \tag{1.16}$$

where z_c is the distance from the middle surface to point C, and β is the slope of the laminate middle surface in the x direction, that is,

$$\beta = \frac{\partial w_0}{\partial x} \tag{1.17}$$

Then the displacement, u, at any point z through the laminate thickness is

$$u = u_0 - z\frac{\partial w_0}{\partial x} \tag{1.18}$$

By similar reasoning, the displacement, v, in the y direction is

$$v = v_0 - z\frac{\partial w_0}{\partial y} \tag{1.19}$$

The laminate strains have been reduced to ε_x, ε_y, and γ_{xy} by virtue of the Kirchhoff hypothesis. For small strains (linear elasticity), those strains are defined in terms of displacements as

$$\begin{aligned} \varepsilon_x &= \frac{\partial u}{\partial x} \\ \varepsilon_y &= \frac{\partial v}{\partial y} \\ \gamma_{xy} &= \frac{\partial u}{\partial y} + \frac{\partial v}{\partial x} \end{aligned} \tag{1.20}$$

Thus for the displacement u and v in equation 1.17 and 1.18, the strains are

$$\begin{bmatrix} \varepsilon_x \\ \varepsilon_y \\ \gamma_{xy} \end{bmatrix} = \begin{bmatrix} \varepsilon^0{}_x \\ \varepsilon^0{}_y \\ \gamma^0{}_{xy} \end{bmatrix} + z \begin{bmatrix} \kappa_x \\ \kappa_y \\ \kappa_{xy} \end{bmatrix} \tag{1.21}$$

Where the middle surface strains are

$$\begin{bmatrix} \varepsilon^0{}_x \\ \varepsilon^0{}_y \\ \gamma^0{}_{xy} \end{bmatrix} = \begin{bmatrix} \dfrac{\partial u_0}{\partial x} \\ \dfrac{\partial v_0}{\partial y} \\ \dfrac{\partial u_0}{\partial y} + \dfrac{\partial v_0}{\partial x} \end{bmatrix} \tag{1.22}$$

and the middle-surface curvatures are

$$\begin{bmatrix} \kappa_x \\ \kappa_y \\ \kappa_{xy} \end{bmatrix} = \begin{bmatrix} \dfrac{\partial^2 w_0}{\partial x^2} \\ \dfrac{\partial^2 w_0}{\partial y^2} \\ 2\dfrac{\partial^2 w_0}{\partial x \partial y} \end{bmatrix} \tag{1.23}$$

The last term in equation 1.22 is the twist curvature of the middle surface. Since only the middle-surface is the reference surface to the curvatures, the note "0" is not necessary.

In a laminate, the stress strain relations for k^{th} lamina can be written as

$$[\sigma]_k = [\overline{Q}_{ij}]_k [\varepsilon]_k \tag{1.24}$$

where the $\overline{Q}_{ij}$ are given in equation 1.12.

By substitution of the strain variation through the thickness, equations 1.21 and 1.24 can be expressed in terms of the laminate middle-surface strains and curvatures as

$$\begin{bmatrix} \sigma_x \\ \sigma_y \\ \tau_{xy} \end{bmatrix} = \begin{bmatrix} \overline{Q}_{11} & \overline{Q}_{12} & \overline{Q}_{16} \\ \overline{Q}_{12} & \overline{Q}_{22} & \overline{Q}_{26} \\ \overline{Q}_{16} & \overline{Q}_{26} & \overline{Q}_{66} \end{bmatrix}_k \left[\begin{bmatrix} \varepsilon^0{}_x \\ \varepsilon^0{}_y \\ \gamma^0{}_{xy} \end{bmatrix} + z \begin{bmatrix} \kappa_x \\ \kappa_y \\ \kappa_{xy} \end{bmatrix} \right] \tag{1.25}$$

The $\overline{Q}_{ij}$ can be different for each layer of the laminate, so the stress variation through the laminate thickness is not necessarily linear, even though the strain variation is linear. There is a hidden assumption here, that is the stress and strain in a layer are uniform and linear.

The resultant forces, N, and moments, M, acting on a laminate are obtained by integration of the stresses in each layer or lamina through the laminate thickness as

$$\begin{bmatrix} N_x \\ N_y \\ N_{xy} \end{bmatrix} = \int_{-\frac{t}{2}}^{\frac{t}{2}} \begin{bmatrix} \sigma_x \\ \sigma_y \\ \tau_{xy} \end{bmatrix} dz = \sum_{k=1}^{N} \int_{z_{k-1}}^{z_k} \begin{bmatrix} \sigma_x \\ \sigma_y \\ \tau_{xy} \end{bmatrix} dz \tag{1.26}$$

and

$$\begin{bmatrix} M_x \\ M_y \\ M_{xy} \end{bmatrix} = \int_{-\frac{t}{2}}^{\frac{t}{2}} \begin{bmatrix} \sigma_x \\ \sigma_y \\ \tau_{xy} \end{bmatrix} z\, dz = \sum_{k=1}^{N} \int_{z_{k-1}}^{z_k} \begin{bmatrix} \sigma_x \\ \sigma_y \\ \tau_{xy} \end{bmatrix} z\, dz \tag{1.27}$$

where t, z_k, and z_{k-1} are defined in basic laminate geometry of Figure 1.23.

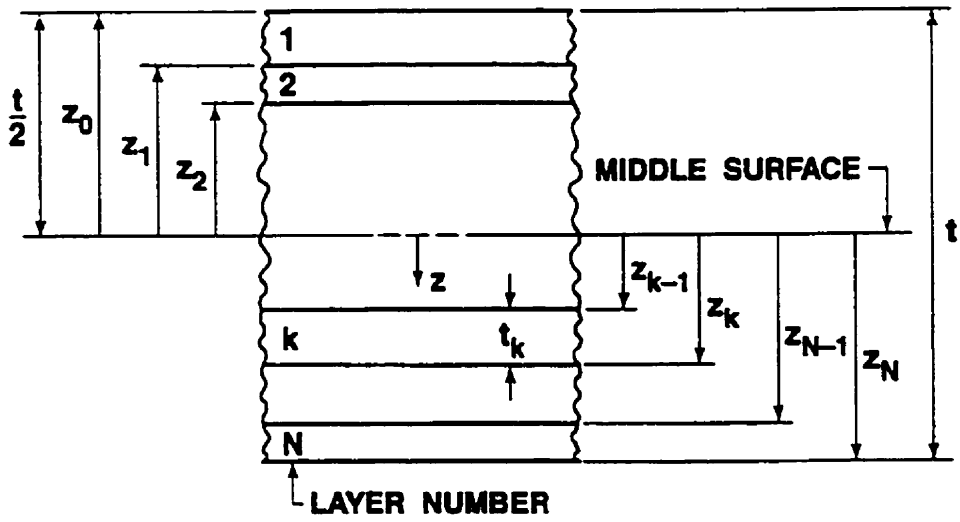

Figure 1.23. Geometry of an N-layered laminate [40]

We rearrange the equations 1.26 and 1.27 to take the advantage of the fact that the stiffness matrix for a lamina is often constant within the lamina, the forces and the moments become

$$\begin{bmatrix} N_x \\ N_y \\ N_{xy} \end{bmatrix} = \sum_{k=1}^{N} \begin{bmatrix} \bar{Q}_{11} & \bar{Q}_{12} & \bar{Q}_{16} \\ \bar{Q}_{12} & \bar{Q}_{22} & \bar{Q}_{26} \\ \bar{Q}_{16} & \bar{Q}_{26} & \bar{Q}_{66} \end{bmatrix}_k \left[\int_{z_{k-1}}^{z_k} \begin{bmatrix} \varepsilon^0{}_x \\ \varepsilon^0{}_y \\ \gamma^0{}_{xy} \end{bmatrix} dz + \int_{z_{k-1}}^{z_k} \begin{bmatrix} \kappa_x \\ \kappa_y \\ \kappa_{xy} \end{bmatrix} z\, dz \right] \tag{1.28}$$

$$\begin{bmatrix} M_x \\ M_y \\ M_{xy} \end{bmatrix} = \sum_{k=1}^{N} \begin{bmatrix} \overline{Q}_{11} & \overline{Q}_{12} & \overline{Q}_{16} \\ \overline{Q}_{12} & \overline{Q}_{22} & \overline{Q}_{26} \\ \overline{Q}_{16} & \overline{Q}_{26} & \overline{Q}_{66} \end{bmatrix}_k \left[\int_{z_{k-1}}^{z_k} \begin{bmatrix} \varepsilon^0{}_x \\ \varepsilon^0{}_y \\ \gamma^0{}_{xy} \end{bmatrix} z\,dz + \int_{z_{k-1}}^{z_k} \begin{bmatrix} \kappa_x \\ \kappa_y \\ \kappa_{xy} \end{bmatrix} z^2\,dz \right] \tag{1.29}$$

Since the ε^0_x, ε^0_y, γ^0_{xy}, κ_x, and κ_y are not function of z, but are middle-surface values, they can be removed from within the summation signs. Thus we have generalized classical lamination theory as:

$$\begin{bmatrix} N_x \\ N_y \\ N_{xy} \end{bmatrix} = \begin{bmatrix} A_{11} & A_{12} & A_{16} \\ A_{12} & A_{22} & A_{26} \\ A_{16} & A_{26} & A_{66} \end{bmatrix} \begin{bmatrix} \varepsilon^0{}_x \\ \varepsilon^0{}_y \\ \gamma^0{}_{xy} \end{bmatrix} + \begin{bmatrix} B_{11} & B_{12} & B_{16} \\ B_{12} & B_{22} & B_{26} \\ B_{16} & B_{26} & B_{66} \end{bmatrix} \begin{bmatrix} \kappa_x \\ \kappa_y \\ \kappa_{xy} \end{bmatrix} \tag{1.30}$$

$$\begin{bmatrix} M_x \\ M_y \\ M_{xy} \end{bmatrix} = \begin{bmatrix} B_{11} & B_{12} & B_{16} \\ B_{12} & B_{22} & B_{26} \\ B_{16} & B_{26} & B_{66} \end{bmatrix} \begin{bmatrix} \varepsilon^0{}_x \\ \varepsilon^0{}_y \\ \gamma^0{}_{xy} \end{bmatrix} + \begin{bmatrix} D_{11} & D_{12} & D_{16} \\ D_{12} & D_{22} & D_{26} \\ D_{16} & D_{26} & D_{66} \end{bmatrix} \begin{bmatrix} \kappa_x \\ \kappa_y \\ \kappa_{xy} \end{bmatrix} \tag{1.31}$$

where

$$\begin{aligned} A_{ij} &= \sum_{k=1}^{N} \left(\overline{Q}_{ij}\right)_k (z_k - z_{k-1}) \\ B_{ij} &= \frac{1}{2} \sum_{k=1}^{N} \left(\overline{Q}_{ij}\right) (z_k^2 - z_{k-1}^2) \\ D_{ij} &= \frac{1}{3} \sum_{k=1}^{N} \left(\overline{Q}_{ij}\right) (z_k^3 - z_{k-1}^3) \end{aligned} \tag{1.32}$$

In equations 1.30, 1.31, and 1.32, the A_{ij} are extensional stiffnesses, the B_{ij} are bending-extension coupling stiffnesses, and D_{ij} are bending stiffnesses.

1.3.3. Balanced Angle Ply Laminates

For balanced angle ply laminates with the lay up angle of $\pm\phi$, the shear extension coupling A_{16} and A_{26}, the bending extension coupling, B_{ij}, and the bend twist coupling, D_{16} and D_{26}, are all zero. Thus the classical lamination theory becomes

$$\begin{bmatrix} N_x \\ N_y \\ N_{xy} \end{bmatrix} = \begin{bmatrix} A_{11} & A_{12} & 0 \\ A_{12} & A_{22} & 0 \\ 0 & 0 & A_{66} \end{bmatrix} \begin{bmatrix} \varepsilon^0_x \\ \varepsilon^0_y \\ \gamma^0_{xy} \end{bmatrix} \tag{1.32}$$

$$\begin{bmatrix} M_x \\ M_y \\ M_{xy} \end{bmatrix} = \begin{bmatrix} D_{11} & D_{12} & 0 \\ D_{12} & D_{22} & 0 \\ 0 & 0 & D_{66} \end{bmatrix} \begin{bmatrix} \kappa_x \\ \kappa_y \\ \kappa_{xy} \end{bmatrix} \tag{1.33}$$

If the laminate plies are all made from the same prepreg tape, thickness t after cure, then equation 1.32 becomes

$$\begin{bmatrix} \sigma_x \\ \sigma_y \\ \tau_{xy} \end{bmatrix} = \begin{bmatrix} \overline{Q}_{11} & \overline{Q}_{12} & 0 \\ \overline{Q}_{12} & \overline{Q}_{22} & 0 \\ 0 & 0 & \overline{Q}_{66} \end{bmatrix} \begin{bmatrix} \varepsilon^0_x \\ \varepsilon^0_y \\ \gamma^0_{xy} \end{bmatrix} \tag{1.34}$$

In the tensile test, the load is applied along the x direction. If the angle ply specimen is very long, relative to its width and thickness, there are uniaxial stress

conditions [41]. This means that the stresses σ_y and τ_{xy} vanish and only σ_x is nonzero with

$$\sigma_x = \left(\overline{Q}_{11} - \nu_{xy}\overline{Q}_{12}\right)\varepsilon_x = E_x\varepsilon_x \tag{1.35}$$

Here E_x is the specimen modulus and ν_{xy} is the principal Poisson's ratio, given by

$$E_x = \overline{Q}_{11} - \nu_{xy}\overline{Q}_{12} \tag{1.36}$$

$$\nu_{xy} = \frac{\overline{Q}_{12}}{\overline{Q}_{22}} \tag{1.37}$$

When a sample is extremely wide, relative to its length, we assume that the grips prevent Poisson's shrinkage from taking place, so there are uniaxial strain conditions [40]. This means the strain ε_y and γ_{xy} vanish and gives the stress:

$$\sigma_x = \overline{Q}_{11}\varepsilon_x \tag{1.38}$$

From equations 1.36 and 1.38 we can see that for angle ply laminates with all angles in the range 0^0 to 90^0:

$$\overline{Q}_{11} \geq E_x \tag{1.39}$$

In the actual case, the test specimens have finite lengths. Equation 1.35 is valid only if the specimen is long enough so that the end effects are not significant in the gauge length. The decay of such localized effects with distance away from the source is justified by the use of Saint-Venant's principle. The decay length, λ, the distance from end of the specimen over which the stress decays to 1/e of the value of the stress at the end for orthotropic composites, is given by [4]:

$$\lambda = \frac{b}{2\pi}\sqrt{\frac{E_1}{G_{12}}} \qquad as \quad \frac{G_{12}}{E_1} << 1 \tag{1.40}$$

Where b is the width of the strip.

1.4 Lamina Failure Criteria

We shall review some of the most widely used composite failure criteria and we shall restrict ourselves to biaxial loading here.

1.4.1. Maximum Stress Criterion and Maximum Strain Criterion

The maximum stress criterion predicts failure load and mode by comparing lamina stresses σ_1, σ_2, and τ_{12} separately. Interactions between the stresses are not considered. The maximum stress criterion for tensile loading involves three equations:

$$\sigma_x = \frac{\sigma_{1u}}{\cos^2 \phi}$$

$$\sigma_x = \frac{\sigma_{2u}}{\sin^2 \phi} \qquad (1.41)$$

$$\sigma_x = \frac{\tau_{12u}}{\sin \phi \cos \phi}$$

Where

σ_{1u}, σ_{2u} and τ_{12u} are the lamina longitudinal strength, transverse strength, and shear strength respectively.

The maximum strain criterion is similar to the maximum stress criterion since the lamina is presumed to fail elastically. The equations are:

$$\sigma_x = \frac{\sigma_{1u}}{\cos^2 \phi - \nu_{12} \sin^2 \phi}$$

$$\sigma_x = \frac{\sigma_{2u}}{\sin^2 \phi - \nu_{21} \cos^2 \phi} \qquad (1.42)$$

$$\sigma_x = \frac{\tau_{12}}{\sin \phi \cos \phi}$$

The only difference between the maximum stress criterion and the maximum strain criterion is that the latter includes Poisson's ratio terms.

1.4.2. Tsai-Hill Failure Criterion

The Tsai-Hill criterion is one of the interactive criteria. These criteria predict the failure by using a single quadratic or higher order polynomial equation involving all stresses or strains. The theory is based on the distortion energy failure theory of von-Mises for isotropic materials. (The total strain energy in a body consists of two parts, one due to a change in volume, called dilation energy, and the second due to a change in shape and is called distortion energy.) It is assumed that failure takes place when the distortion energy is greater than some critical value called the failure distortion energy of the material. Hill adapted the von-Mises distortional energy yield criterion to anisotropic materials, and then Tsai adapted it to a unidirectional lamina. This gives the equation:

$$\frac{1}{\sigma_x^2} = \frac{\cos^4\phi}{\sigma_{1u}^2} + \left(\frac{1}{\tau_{12}^2} - \frac{1}{\sigma_{1u}^2}\right)\cos^2\phi\sin^2\phi + \frac{\sin^4\phi}{\sigma_{2u}^2} \qquad (1.43)$$

The criterion gives a smooth curve rather than cusps obtained with the maximum stress and maximum strain criteria.

1.4.3. Tsai-Wu Failure Criterion

One obvious way to improve the correlation between a criterion and experiment is to increase the number of terms in the prediction equation. Tsai and Wu did this to develop an improved interactive criterion. The new criterion is based on the total strain energy failure theory of Beltrami (see reference [40]). The criterion is:

$$F_{11}\sigma_1^2 + F_{22}\sigma_2^2 + F_{66}\tau_{12}^2 + F_1\sigma_1 + F_2\sigma_2 + 2F_{12}\sigma_1\sigma_2 = 1 \qquad (1.44)$$

Where

$$F_1 = (\frac{1}{\sigma_{1u}}) + (\frac{1}{\sigma_{1cu}}), \qquad F_2 = (\frac{1}{\sigma_{2u}})(\frac{1}{\sigma_{2cu}}), \qquad F_{11} = -\frac{1}{\sigma_{1u}(\sigma_{1cu})},$$

$$F_{22} = -\frac{1}{\sigma_{2u}(\sigma_{2cu})}, \qquad F_{66} = \frac{1}{\tau_{12u}^2},$$

F_{12} is an experimental determined parameter, Tsai assumes $F_{12} = -\frac{\sqrt{F_{11}F_{22}}}{2}$.

σ_{1cu} and σ_{2cu} are the lamina longitudinal compressive strength and transverse compressive strength respectively.

When the compressive strengths equal to the tensile strength, the Tsai-Wu criterion reduces to the Tsai-Hill criterion.

1.4.4. Other Composite Failure Criteria

Soden et al [42] recently organized a failure exercise, in which people were invited to predict composite strength and stress strain behavior under different loading cases. Table 1.4 lists the failure criteria used in the exercise and their representatives.

Table 1.4. Modes of failure in the theories [43]*

Mode of failure	Failure criterion	Theory representatives
Fiber failure in tension	$\frac{1}{\varepsilon_{1t}}\left(\varepsilon_1+\frac{\nu_{f12}}{E_{f1}}m_{\sigma f}\sigma_2\right)=1$	Puck
Longitudinal tension failure	$\sigma_1=\sigma_{1t}$	Zinoviev, Rotem, Sun, Edge
Longitudinal tensile failure	$\varepsilon_1=\varepsilon_{1t}$	Hart-Smith and Eckold
Fiber failure in tension and compression	$\left[\frac{\int_{\varepsilon_1^*}^{\varepsilon_1}\sigma_1 d\varepsilon_1}{\int_{\varepsilon_1^*}^{\varepsilon_1}\sigma_1 d\varepsilon_1}\right]^{m1} \Big/ \sum_{i=1,2,6}\left[\frac{\int_{\varepsilon_i^*}^{\varepsilon_i}\sigma_1 d\varepsilon_i}{\int_{\varepsilon_i^*}^{\varepsilon_i}\sigma_1 d\varepsilon_i}\right]^{mi} \geq 0.1$	Wolf
Fiber failure in compression	$\frac{1}{\varepsilon_{1c}}\left(\varepsilon_1+\frac{\nu_{f12}}{E_{f1}}m_{\sigma f}\sigma_2\right)=1-(10\gamma_{12})$	Puck
Longitudinal compressive failure	$\sigma_1=\sigma_{1cf}$	Zinoviev, Rotem, Sun, Edge, Hart-Smith and Eckold
Longitudinal compressive failure	$\varepsilon_1=\varepsilon_{1cf}$	Hart-Smith and Eckold

Table 1.4. Contd. [43]

Mode of failure	Failure criterion	Theory representatives
Shear of fiber	$\varepsilon_1 = \pm\nu_{fII}\left(\frac{1+\nu_{fII}}{1+\nu_{fI}}\right)\varepsilon_1^t$ $\varepsilon_1 = \mp R_e\left(\frac{1+\nu_{fII}}{1+\nu_{fI}}\right)\varepsilon_1^t$	Hart-Smith
Transverse tensile failure	$\sigma_2 = \sigma_1$	Zinoviev, Edge, Eckold and Sun
Transverse tensile cracking	$\sigma + k\sigma_1\rangle \sqrt{\frac{4p\gamma}{\frac{1}{E_A(2p)} - \frac{1}{E_A(p)}}} + \bar{\sigma}_0$, where 2γ is fracture energy.	McCarteny
Transverse tensile failure	$\varepsilon_2 = \varepsilon_{21}$	Hart-Smith and Eckold
Transverse compressive failure	$\sigma_2 = \sigma_{21}$	Zinoviev, Edge, Eckold and Sun
Transverse compressive failure	$\varepsilon_2 = \varepsilon_{2C}$	Hart-Smith and Eckold
Inter-fiber failure mode A for transverse tension	$\sqrt{\left(\frac{\tau_{21}}{S_{21}}\right)^2 + \left(1 - p_{1\parallel}^{(+)}\frac{\sigma_1}{S_{21}}\right)^2\left(\frac{\sigma_2}{\sigma_1}\right)^2} + p_{1\parallel}^{(+)}\frac{\sigma_2}{S_{21}} = 1 - \frac{\sigma_1}{\sigma_{1D}}$	Puck

Table 4.1. Contd. [43]

Mode of failure	Failure criterion	Theory representatives
Inter-fiber failure mode B for moderate transverse compression	$\frac{1}{S_{21}}\left(\sqrt{\tau_{21}^2+\left(p_{\perp\parallel}^{(-)}\sigma_2\right)^2}+p_{\perp\parallel}^{(-)}\sigma_2\right)=1-\frac{\sigma_1}{\sigma_{1t}}$	Puck
Inter-fiber failure mode C for large transverse compression	$\left[\left(\frac{\tau_{21}}{2\left(1+p_{\perp\parallel}^{(-)}\right)S_{21}}\right)^2+\left(\frac{\sigma_2}{\sigma_f}\right)^2\right]\frac{\sigma_f}{(-\sigma_2)}=1-\frac{\sigma_1}{\sigma_{1t}}$	Puck
In-plane shear failure	$\tau_{12}=S_{12}$	Zinoviev, Edge, Hart-Smith, and Sun
Combined transverse tension and shear	$\left(\frac{\sigma_2}{\sigma_{2f}}\right)^2+\left(\frac{\tau_{12}}{S_{12}}\right)^2=1$	Edge
Combined longitudinal compression and shear	$\left(\frac{\sigma_1}{H_{1c}}\right)+\left\lvert\frac{\tau_{12}}{S_{12}}\right\rvert=1$	Edge
Delamination	$\tau_{12}t_e>\omega_r$	Edge
Matrix failure	$\left(\frac{\sigma_2}{\sigma_f}\right)^2+\left(\frac{\tau_{12}}{S_{12}}\right)^2=1$	Edge

Table 1.4. Contd.[43]

Mode of failure	Failure criterion	Theory representatives
Matrix failure	$\left(\frac{E_{m(\varepsilon_1)}\varepsilon_1}{\sigma_{mf}}\right)^2+\left(\frac{\sigma_2}{\sigma_t}\right)^2+\left(\frac{\tau_{12}}{S_{12}}\right)^2=1$	Rotem
Matrix failure	$\left[\frac{\int_{\varepsilon_1^*}^{\varepsilon_1}\sigma_1 d\varepsilon_1}{\int_{\varepsilon_1^*}^{\varepsilon_1}\sigma_1 d\varepsilon_1}\right]^{m1} \Big/ \sum_{i=1,2,6}\left[\frac{\int_{\varepsilon_i^*}^{\varepsilon_i}\sigma_i d\varepsilon_i}{\int_{\varepsilon_i^*}^{\varepsilon_i}\sigma_i d\varepsilon_i}\right]^{mi} < 0.1$	Wolf

*:The nomenclature used here is the same as that in the original paper, but includes additional terms to the used in this thesis. there are:

Symbles:

H	shear-compression interaction parameter
k	constant
m_{af}	mean stress magnification factor
p	transverse crack density
$p_{\perp\parallel}^{(-)}$	slope of the σ_n, τ_{nt} fracture envelope for $\sigma_{n<=}0$ at $\sigma_n=0$
$p_{\perp\parallel}^{(+)}$	slope of the σ_n, τ_{nt} fracture envelope for $\sigma_n>0$ at $\sigma_n=0$
Rε	$\varepsilon_T/\varepsilon_{fT}$
S	shear strength
σ_{1D}	stress value for lamina degradation
$\overline{\sigma}_0$	effective crack closure stress for uniaxial loading
t_e	effective ply thickness
ω_f	delamination criterion

Subscripts:

A	axial direction
L	longitudinal
n	normal
nt	normal/transverse
T	tensile
T	transverse

Superscripts:

m_i	strain energy shape factor
t	to failure
u	ultimate

1.4.5. Laminate Failure Analysis

For a laminate, or a composite, there is a lack of faith in the failure criteria in current use. There is even no universal definition of what constitutes "failure" of a composite. In the broadest sense, a designer would define "failure" as the point at which the structure or component ceases to fulfill its function. Therefore, the failure is to the specific application. It would be the weeping of fluid through the pipe wall to the pipe designer, or it would be a 10% loss of stiffness to a bridge designer. Also there is lack of evidence to show whether any of the criteria provide accurate and meaningful predictions of failure over anything other than a very limited range of circumstances.

A composite plate exhibits progressive failure on a layer-by-layer basis. Because of the various characteristics of composite laminates, it is difficult to determine a strength criterion in which all failure modes and their interactions are properly accounted for. Moreover, the verification of a proposed strength criterion is greatly complicated by scatter in measured strengths caused by inconsistent processing techniques and inappropriate and misleading experimental techniques.

Before using the lamina properties to predict laminate strength, Hashin's words in a letter to Soden, quoted in Hinton and Soden's recent paper (1998) [43] are worth noting: "My only work in this subject relates to failure criteria of unidirectional fiber composites, not to laminates. I do not believe that even the most complete information about failure of single plies is sufficient to predict the failure of a laminate, consisting of

such plies. A laminate is a structure which undergoes a complex damage process (mostly of cracking) until it finally fails. The analysis of such a process is a per requisite for failure analysis. While significant advances have been made in this direction we have not yet arrived at the practical goal of failure prediction. I must say to you that I personally do not know how to predict the failure of a laminate (and furthermore, that I do not believe that anybody else does)."

All composite laminate strength criteria depend on the strengths in the lamina principal material directions, which likely do not coincide with laminae principal stress directions. Therefore, the strength of each lamina in a laminate must be assessed in a coordinate system that is likely different from those of its neighboring laminae. This coordinate mismatch is but one of the complications that characterize even a macroscopic strength criterion for laminates. Figure 1.24 shows the laminate strength analysis elements.

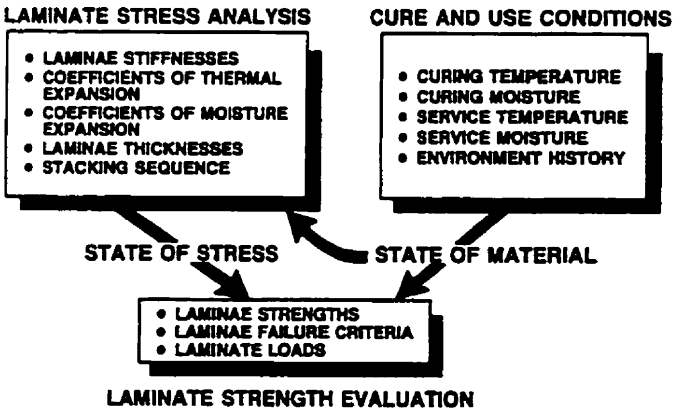

Figure 1.24. Laminate strength analysis elements [40]

A laminate can be subjected to thermal, moisture, and mechanical loads. A method of strength analysis is required to determine either the maximum loads that a given laminate can withstand, or the laminate characteristics necessary to withstand a given load. Figure 1.25 shows the analysis flowchart for laminate strength and load-deformation relations.

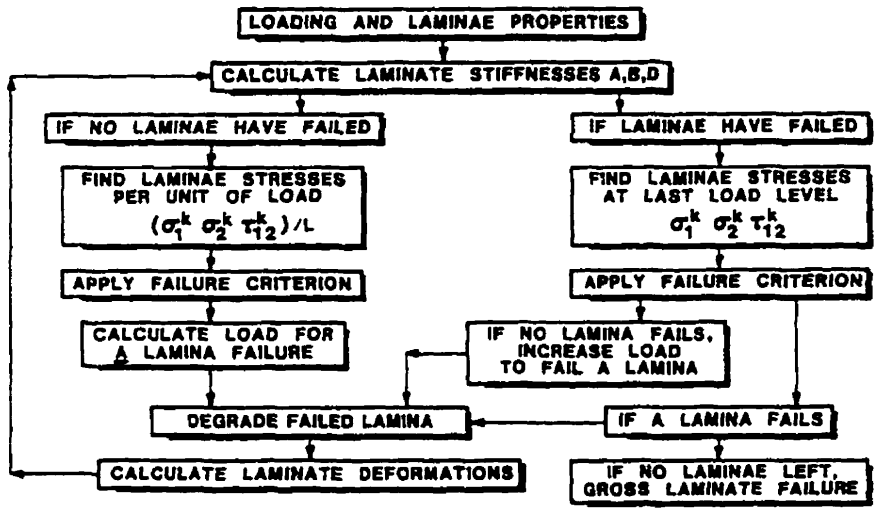

Figure.1.25. A flowchart of the analysis of laminate strength and load-deformation [40]

The procedure is a layer-by-layer analysis. The interaction between the layers is neglected. The lamina failure criteria are not mentioned explicitly in the flowchart. The entire procedure for strength analysis is independent of the actual lamina failure criteria, but the result of the procedure, the maximum loads and deformations, do depend on the specific lamina failure criteria. As in the stiffness analysis and lamina strength analysis, the lamina is assumed to be uniformly loaded, which is not true in actual applications.

1.4.6. Thermal and Hydroscopic Stress Analysis

Laminates normally are cured at temperatures different from the operating temperature. In such case, the thermal stresses arise and must be accounted for in the strength analysis.

The three-dimensional thermoelastic anisotropic strain stress relations are

$$\varepsilon_i = s_{ij}\sigma_j + \alpha_i \Delta T \qquad i,j = 1,2,....,6 \tag{1.45}$$

wherein the total strains ε_i are the sum of the mechanical strains $S_{ij}\sigma_j$ and the six free thermal strains, $\alpha_i\Delta T$, for a temperature change ΔT.

The three-dimensional stress strain relations are obtained by inversion 1.45

$$\sigma_i = C_{ij}\left(\varepsilon_j - \alpha_j \Delta T\right) \quad i,j = 1,2,....,6 \tag{1.46}$$

In both equations 1.45 and 1.46, the six α_i are the coefficients of thermal expansion and ΔT is the temperature difference. In equation 1.46, the terms $C_{ij}\alpha_j\Delta T$ are the thermal stresses if the specimen strain is zero.

The stress in a lamina under thermal and applied strains are

$$\begin{bmatrix}\sigma_1\\ \sigma_2\\ \tau_{12}\end{bmatrix}=\begin{bmatrix}Q_{11} & Q_{12} & 0\\ Q_{12} & Q_{22} & 0\\ 0 & 0 & Q_{66}\end{bmatrix}\begin{bmatrix}\varepsilon_1-\alpha_1\Delta T\\ \varepsilon_2-\alpha_2\Delta T\\ \gamma_{12}\end{bmatrix} \tag{1.47}$$

The stresses in laminate coordinates for the k^{th} layer are obtained by transformation of coordinates to give

$$\begin{bmatrix}\sigma_x\\ \sigma_y\\ \tau_{xy}\end{bmatrix}=\begin{bmatrix}\overline{Q}_{11} & \overline{Q}_{12} & \overline{Q}_{16}\\ \overline{Q}_{12} & \overline{Q}_{22} & \overline{Q}_{26}\\ \overline{Q}_{16} & \overline{Q}_{26} & \overline{Q}_{66}\end{bmatrix}\begin{bmatrix}\varepsilon_x-\alpha_x\Delta T\\ \varepsilon_y-\alpha_y\Delta T\\ \gamma_{xy}-\alpha_{xy}\Delta T\end{bmatrix} \tag{1.48}$$

where the appearance of α_{xy} signifies an apparent coefficient of thermal shear or distortion as in Figure 1.26.

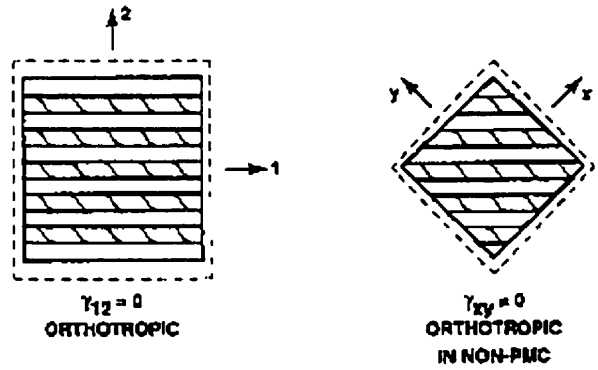

Figure 1.26. Thermal expansion and distortion of an orthotropic lamina [40]

Using equation 1.32 with equation 1.48 we obtain

$$\begin{bmatrix} N_x \\ N_y \\ N_{xy} \end{bmatrix} = \begin{bmatrix} A_{11} & A_{12} & A_{16} \\ A_{12} & A_{22} & A_{26} \\ A_{16} & A_{26} & A_{66} \end{bmatrix} \begin{bmatrix} \varepsilon_x^0 \\ \varepsilon_y^0 \\ \gamma_{xy}^0 \end{bmatrix} + \begin{bmatrix} B_{11} & B_{12} & B_{16} \\ B_{12} & B_{22} & B_{26} \\ B_{16} & B_{26} & B_{66} \end{bmatrix} \begin{bmatrix} \kappa_x \\ \kappa_y \\ \kappa_{xy} \end{bmatrix} - \begin{bmatrix} N_x^T \\ N_y^T \\ N_{xy}^T \end{bmatrix} \tag{1.49}$$

Where the thermal force are

$$\begin{bmatrix} N_x^T \\ N_y^T \\ N_{xy}^T \end{bmatrix} = \int \begin{bmatrix} \overline{Q}_{11} & \overline{Q}_{12} & \overline{Q}_{16} \\ \overline{Q}_{12} & \overline{Q}_{22} & \overline{Q}_{26} \\ \overline{Q}_{16} & \overline{Q}_{26} & \overline{Q}_{66} \end{bmatrix}_k \begin{bmatrix} \alpha_x \\ \alpha_y \\ \alpha_{xy} \end{bmatrix}_k \Delta T dz \tag{1.50}$$

(Note that N^T are the true thermal forces only when the total strains and curvatures are zero.)

Thus the force resultants can be rearranged to read

$$\begin{bmatrix} \overline{N}_x \\ \overline{N}_y \\ \overline{N}_{xy} \end{bmatrix} = \begin{bmatrix} N_x + N_x^T \\ N_y + N_y^T \\ \overline{N}_{xy} + \overline{N}_{xy}^T \end{bmatrix} = \begin{bmatrix} A_{11} & A_{12} & A_{16} \\ A_{12} & A_{22} & A_{26} \\ A_{16} & A_{26} & A_{66} \end{bmatrix} \begin{bmatrix} \varepsilon_x^0 \\ \varepsilon_y^0 \\ \gamma_{xy}^0 \end{bmatrix} + \begin{bmatrix} B_{11} & B_{12} & B_{16} \\ B_{12} & B_{22} & B_{26} \\ B_{16} & B_{26} & B_{66} \end{bmatrix} \begin{bmatrix} \kappa_x \\ \kappa_y \\ \kappa_{xy} \end{bmatrix} \tag{1.51}$$

In a similar manner, the moment resultants can be written as

$$\begin{bmatrix} \overline{M}_x \\ \overline{M}_y \\ \overline{M}_{xy} \end{bmatrix} = \begin{bmatrix} M_x + M_x^T \\ M_y + M_y^T \\ \overline{M}_{xy} + \overline{M}_{xy}^T \end{bmatrix} = \begin{bmatrix} B_{11} & B_{12} & B_{16} \\ B_{12} & B_{22} & B_{26} \\ B_{16} & B_{26} & B_{66} \end{bmatrix} \begin{bmatrix} \varepsilon_x^0 \\ \varepsilon_y^0 \\ \gamma_{xy}^0 \end{bmatrix} + \begin{bmatrix} D_{11} & D_{12} & D_{16} \\ D_{12} & D_{22} & D_{26} \\ D_{16} & D_{26} & D_{66} \end{bmatrix} \begin{bmatrix} \kappa_x \\ \kappa_y \\ \kappa_{xy} \end{bmatrix} \tag{1.52}$$

Equations 1.51 and 1.52 can also be used for moisture induced stresses if we replace the α_j by the coefficients of moisture expansion, β_j. The moisture effects arise because polymer materials absorb moisture and expand.

1.5 Interlaminar Stresses

One of the key limitations of the classical lamination theory is that each ply is assumed to be in plane stress in the x-y plane, and the interlaminar stresses associated with z axis are neglected. The interlaminar stresses can cause delamination, or separation of the laminate. A three dimensional elasticity solution by Pipes and Pagano [44] has shown that even in a laminate under simple uniaxial loading, see Figure 1.27, there is a boundary layer region along the free edge where a three dimensional state of stress exists, and that the boundary layer thickness is roughly equal to the laminate thickness.

Pipes and Daniel [45] then performed experiments to confirm Pipes and Pagano's solution for interlaminar stresses by using Moire technique. They used $[+25^0_4/-25^0_8/+25^0_4]$ long and narrow specimen (152 mm gauge length and 25 mm width). The results, as shown in Figure 1.28, agreed well with the elasticity solution.

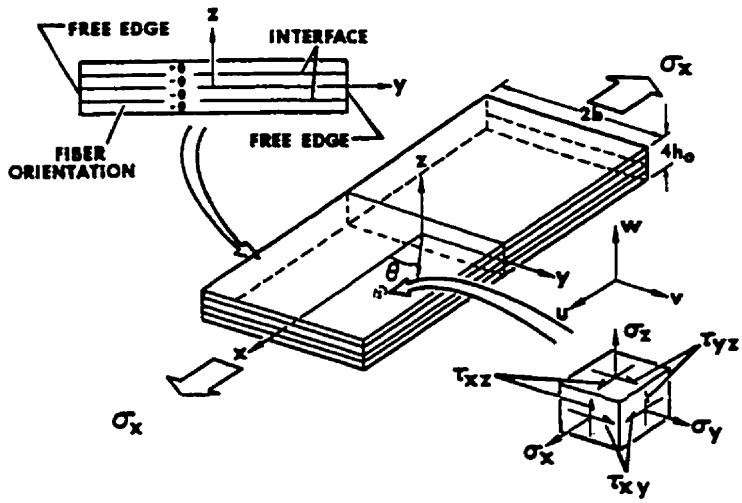

Figure 1.27. Symmetric angle-ply laminate geometry and stresses [44]

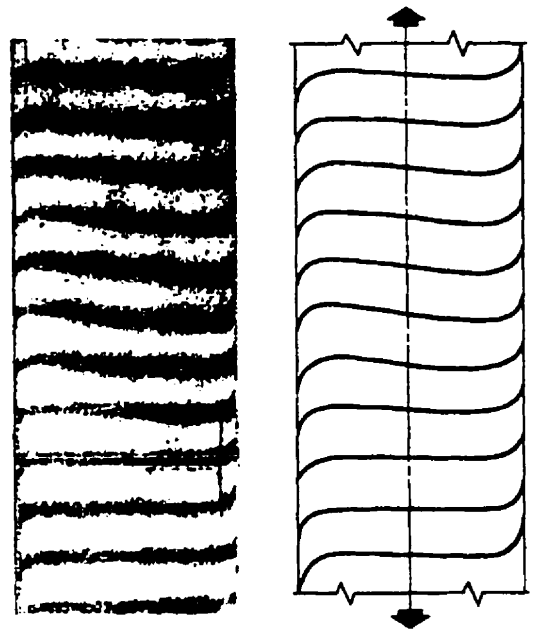

Figure 1.28. Moire fringe pattern [45]

The significance of interlaminar stresses relative to laminate stiffness, strength, and life is determined by classical lamination theory, i.e. classical lamination theory stresses are accurate over most of the laminate except in a very narrow boundary layer

near the free edges. Thus according to this work laminate stiffnesses are affected by global, not local, stresses, so laminate stiffnesses are essentially unaffected by interlaminar stresses. Nevertheless, as noted early (section 1.2.1), the proximity of free edges have been observed experimentally to reduce stiffness and this also been confirmed theoretically.

On the other hand, the details of locally high stresses dominate the failure process whereas lower global stresses are unimportant. Thus, laminate strength is dominated by interlaminar stresses in certain loading cases.

1.6 Photoelastic Measurement

The photoelastic method consists of bonding a thin sheet of photoelastic coating material to the surface of the specimen, such that the bonded interface is reflective [46]. When the specimen is loaded the surface strains are transmitted to the coating and produce a fringe pattern that is recorded and analyzed by means of a reflection polariscope. A perfect strain transmission yields:

$$\begin{aligned} \varepsilon_x^c &= \varepsilon_x^s \\ \varepsilon_y^c &= \varepsilon_y^s \end{aligned} \tag{1.53}$$

where

Superscripts c and s refer to the coating and the specimen respectively.

The difference in principal strains and the coating birefringence are related by the strain-optic law. This is:

$$\varepsilon_x^c - \varepsilon_y^c = \varepsilon_x^s - \varepsilon_y^s = nf \tag{1.54}$$

where the n is fringe order and f is the coating fringe value.

When the composite is orthotropic with the elastic axes of symmetry x, y coinciding with the axes of material, geometric, and loading symmetry, the coating birefringence is related to the principal stresses in the composite by:

$$(\frac{\sigma_x}{E_x})(1+\nu_{xy}) - (\frac{\sigma_y}{E_y})(1+\nu_{yx}) = nf \tag{1.55}$$

Where ν_{yx} is the minor Poisson's ratio, which equals to $\frac{\overline{Q}_{12}}{\overline{Q}_{11}}$.

1.7 Project Objectives

We have pointed out in section 1.2.1 that classical lamination theory does not appear to be obeyed by angle ply laminates. Thus the nominal stiffness of a $[\pm 45]_s$ laminate increases with increasing specimen width at a fixed gauge length (see Figure 1.15). Furthermore, some theoretical descriptions of some edge effects have been available. But test specimen aspect ratio effect appears not yet to have been examined in any detail.

Thus the Khatzibadeh work showed that a long and narrow specimen cannot be used to measure the laminate properties correctly because it cannot represent the composites used in the real structures, such as in the airplane wing skin, where the composite structure is very wide and short. In these structures the free edge effects may be considered to be limited. The composites under such conditions perform differently.

The problem with the long and narrow specimen, such as the ASTM D3039 test coupon, is probably that there is no fiber going across from grip to grip when the lay-up angle is larger than 9^0. In this situation, we do not fully stress the fibers. If we do not break the fibers we do not test the composite.

In general, to measure laminate elastic constants and strengths accurately is very important. Any kind of under estimation may cause danger or over estimation may result in waste of materials. Surprisingly, there is little agreement in the literature about how to relate laminate properties to the lamina then onto the fiber and matrix properties. Perhaps the major reason for this is that experiments on laminates have proved quite difficult to perform. These difficulties are largely due to complications peculiar to composites, such as the edge effects and the gripping effects, the difference in strength between fiber and matrix, and the general sensitivity of composites to stress concentrations.

The objective of this project is to measure the mechanical properties of angle ply laminates as accurately as possible and to develop a simple model to describe the angle ply laminate modulus and strength. This work is based on the works conducted by

Khatibzadeh using wide and short specimens to study the effect of fiber alignment on composite strength. The test results and the modeling are presented in this thesis.

2. EXPERIMENTAL METHOD

2.1 Material and Test Samples

2.1.1 Materials and Laminate Consolidation

Two carbon epoxy prepregs obtained from Hexcel were used in the experiment. The T7G 145-12-F584-9 prepreg was used in making tensile specimens and the R6376-TENAX-HAT-134 prepreg was used in making a compressive specimen. Cut sheets were laid in a steel mold of 89 mm x 127 mm size for short and wide specimens and in another steel mold of 310 mm x 310 mm for ASTM specimens. They were then hot pressed under about 1.6 MPa pressure following the temperature profile recommended by Hexcel. This profile specified heating at 2^0 C/min to 180^0 C. holding for 120 min., then cooling at 8^0C/min to room temperature. The thickness of each laminate was measured after consolidation. They were 1 ± 0.05 mm.

2.1.2 Tensile Specimen

The laminates were then cut using a diamond band saw with water-cooling to produce $[\pm\phi]_{2s}$ tensile specimens. The short and wide specimen sizes were 25 mm, 43 mm, and 100 mm width with 125 mm, 125 mm, and 87 mm length respectively. The ASTM specimens were 25 mm wide and 250 mm long. The specimen thickness was about 1 mm. The gauge length of all the wide and short specimens was kept to 20 mm. The ASTM specimen gauge length was 150 mm. The ϕ used were 0^0,15^0, 30^0, 45^0, 60^0, 75^0, and 90^0. The specimens' edges were then polished using #80 then #120 SiC papers.

Four holes of 11.4mm diameter were drilled in the 100mm width specimens as shown in Figure 2.1.

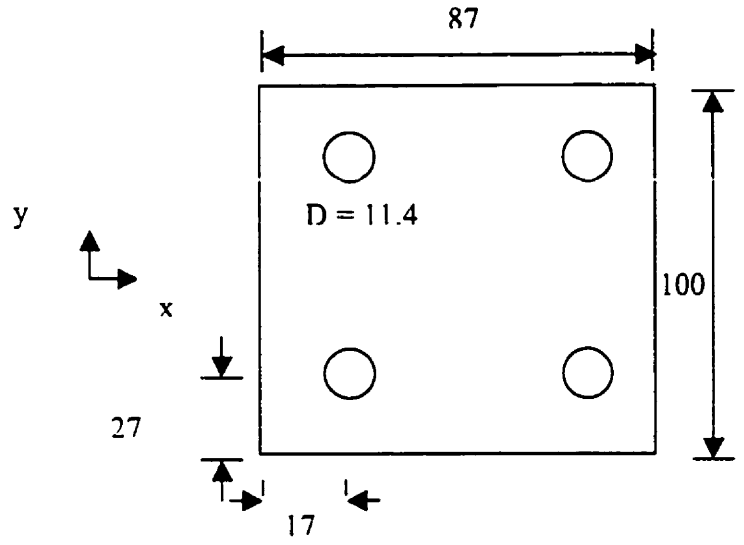

Figure 2.1. 100 mm width specimen (Unit in mm)

A strain gauge, CEA-13-062WT-350, obtained from the Measurements Group, Inc., was bonded onto the middle of the specimen gauge area along the x and y directions, where the load was applied along the x direction. The bonding agent was M-Bond 200 from the same supplier. The specimen surface, where the gauge was bonded, was sanded to remove the mold release agent using #120 and then #500 SiC papers. The surface was then cleaned with tissue paper soaked with acetone. Then the 326-DFV 3 cable, from the same supplier, was fixed to the gauge using rosin core solder.

The short and wide specimens with 43mm and 25mm widths and the ASTM specimens were then end-tabbed. The end tab for short and wide specimens was

aluminum plate with 53 mm long and widths equal to the specimen widths. The same aluminum was also used for the ASTM specimen but the length was 50 mm. The end tab surface was sand blasted before bonding. The specimen surfaces, where the end tab was bonded, were sanded to remove the release agent using the #120 SiC paper. The end tab was then bonded by epoxy with a little pressure applied. The epoxy was cured at room temperature. The specimens are shown in Figure 2.2.

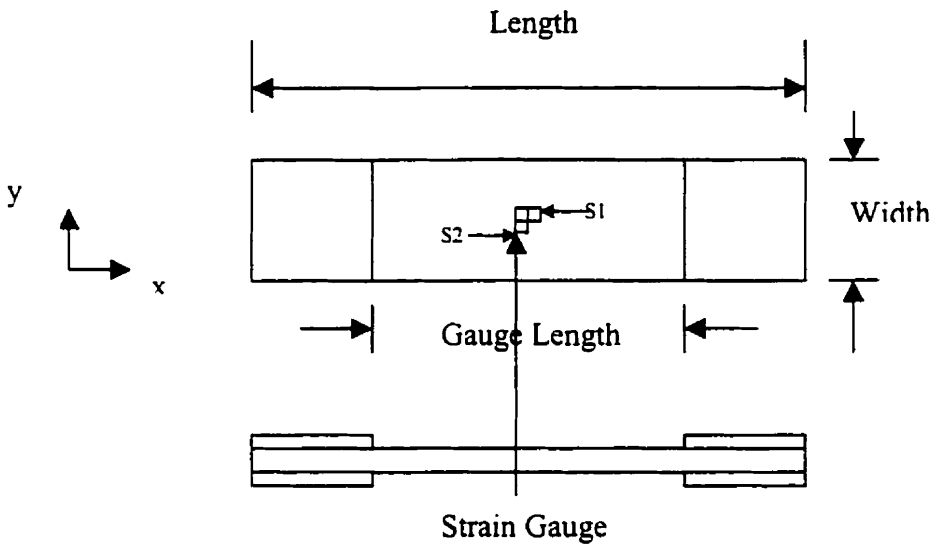

Figure 2.2. Specimen with the strain gauge and end tab

A special clamp was used for the 100 mm width specimens to fit into the test machine grips. This clamp is shown in Figure 2.3. The clamp held the specimen by 4 screws of 9.3 mm diameter tightened by a torque wrench set to about 500 kg-cm.

Another clamp for the 100 mm width specimen was also tried. This clamp is shown in Figure 2.4. It did not hold the sample tightly, and slippage occurred at very low

load. There was no significant difference observed between the two clamps when testing the samples. The detailed dimensions of the two clamps are shown in the Appendix.

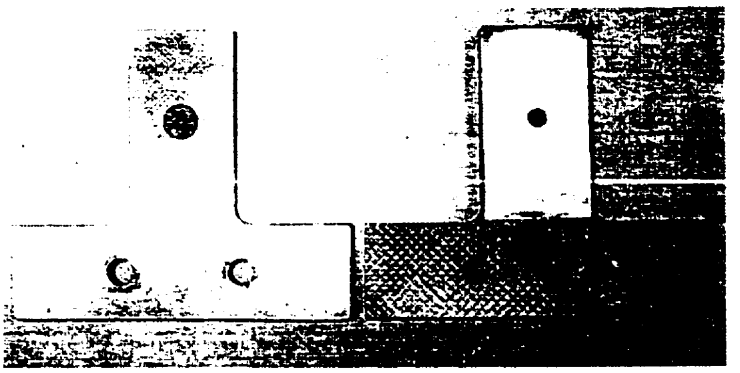

Figure 2.3. Clamps for the 100 mm width specimens

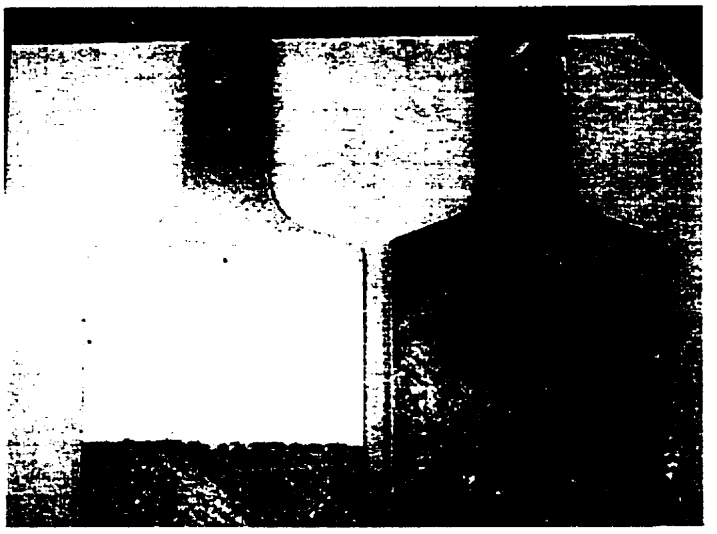

Figure 2.4. Clamps for the 100 mm specimens

2.1.3 Tensile Photoelastic Specimen

A photoelastic coating material, PS-1 sheet, with 0.25mm thickness was used. The coating came from the same supplier that provided the strain gauge. The coating

fringe value, f, was 7570 μm/m fringe. The sheet was cut to 20 mm long and 43 mm wide using a paper cutter. The adhesive for bonding the coating material was PC-1 adhesive from the same supplier.

The specimens used for the photoelastic analysis were 43 mm wide with a strain gauge bonded on one side as specified above. On the other side, a specimen surface was sanded by #120, then #500 SiC paper and cleaned by tissue paper soaked with acetone. The PC-1 adhesive was then applied on the treated surface and the PC-1 coating was bonded. A little pressure was applied to the sample by putting a flat steel bar about 1kg on it, and the sample was left at room temperature for curing for 24 hours. The specimens were then end-tabbed as specified above. The photoelastic specimen is shown in Figure 2.5.

2.1.4 Compressive Specimen

A laminate with $[\pm 15]_{8s}$ lay-up was cut, as specified in 2.1.2, to 63.2mm long and 77.5mm wide. The specimen edges were polished using #120, #320, #500, #800, #1200, #2400 SiC papers, and then were repolished using 1μm OP-Alumina power provided by Struers. The specimen thickness was 3.9 mm.

Three strain gauges, CEA-13-062WT-350, were bonded onto the specimen as shown in Figure 2.6. The bonding method was same as that used in tensile specimens.

A PS-1 photoelastic coating sheet of 35 mm length and the same width as the sample was bonded on the other side of the specimen gauge area as shown in Figure 2.6. The thickness of the coating was 1mm. The coating fringe value, f, was 1892 μm/m fringe. The bonding method was same as that used in the tensile specimens.

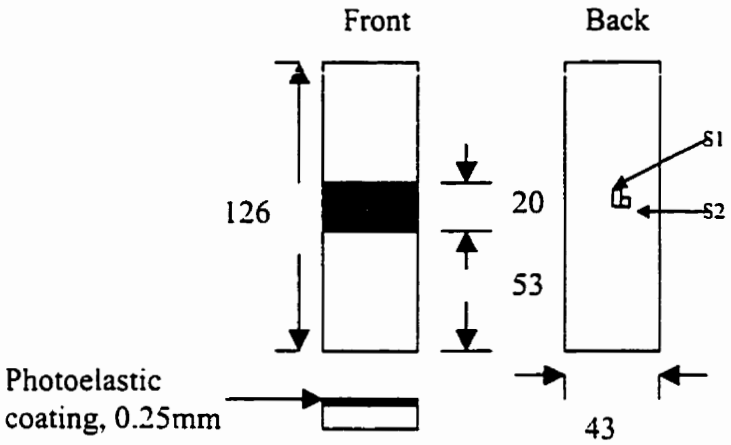

Figure 2.5. Tensile specimen with photoelastic coating

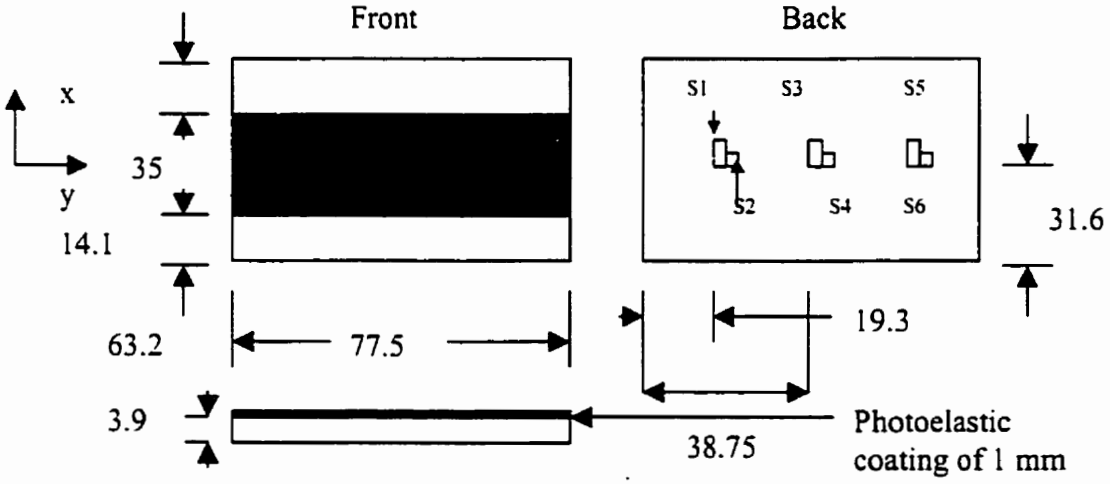

Figure 2.6 Compressive specimen with photoelastic coating

2.2 Mechanical Tests

2.2.1 Tensile Test

The samples were tested in a MTS hydraulic machine at a constant cross head rate under stroke control. The test rate was about 1% strain per minute.

The load was measured by the MTS 100 kN load cell and recorded by an MTS 431 X-Y recorder. The strain was read by two digital strain indicators, one was P-3500 strain gauge indicator and the other was the VISHAY/ELLIS-20 digital strain gauge indicator. The strain was recorded through the indicators by a two-pen Linear 1200 recorder.

The test system, the MTS machine and the strain measurement system, was tested by using three aluminum specimens, which were 150mm long, 25mm wide, and 3.15mm thick, with known modulus of 70GPa and Poisson's ratio of 0.33. The tested modulus was 69.2 ± 0.7 and the tested Poisson's ratio was 0.31 ± 0.01.

The bending of the specimen on the MTS machine was also tested by using ASTM specimens according to ASTM D3039. This standard suggested that the percent bending in the specimens should be less than 3%. The test result was 1%.

The test results were the average from five to six samples. In the case of less than five samples being used, the data were marked. The broken specimens were photographed after the test using Kodak DC2400 digital camera. The fracture surfaces were then measured using a ruler with accuracy of ±1 mm.

2.2.2 Compressive Test

The test was conducted in the Institute for Aerospace Research, NRC. The sample was put between the compressive heads and tested under the loads set manually. The strains from the three strain gauges were read through an 8-channel strain gauge switch box using the P-3500 strain gauge indicator. The maximum load applied on the sample was within the elastic range.

2.3 Photoelastic Analysis

2.3.1 Tensile Test

A circular polariscope was designed and made. The principle of the polariscope design is shown in Figure 2.7.

The sample with the photoelastic coating was mounted in the MTS machine. The loads were set manually. The photoelastic image was recorded by a colour photograph taken at a certain load, and the strain from the strain gauge was recorded at same time.

The maximum stress used in the analysis was about the half of the sample strength. The set-up of the testing is shown in Figure 2.8. About ten photographs were taken for each sample with Kodak 400 color film. The film was then developed by the 1.2.3 Photo Shop.

2.3.2 Compressive Test

The same test sample used in 2.2.2 was used. A 0.05mm thick Teflon film was put between the sample and the compressive head surfaces. A Kodak EOS DCS 5 digital camera then recorded the photoelastic image at certain loads. The strain gauge readings were recorded at the same time as specified in 2.2.2.

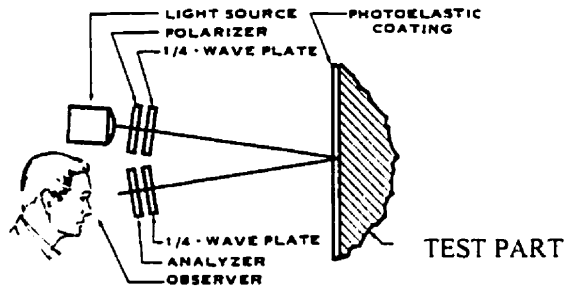

Figure 2.7. Schematic representation of reflection polariscope

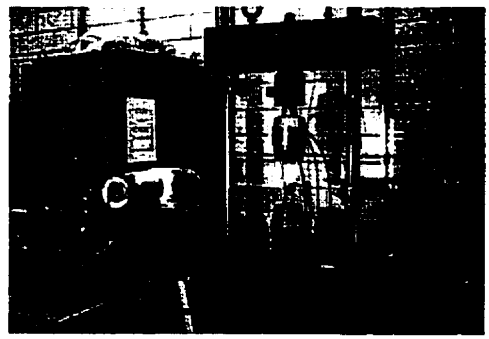

Figure 2.8. Set-up of tensile photoelastic test

3. EXPERIMENTIAL RESULTS

3.1. Stress-Strain Response in the Tensile Test

The test results are shown in Figures 3.1 to 3.7. In each figure, the strain responses in the x direction and the y direction are shown with different widths. Smooth curves are drawn here, the actual responses were jerkier.

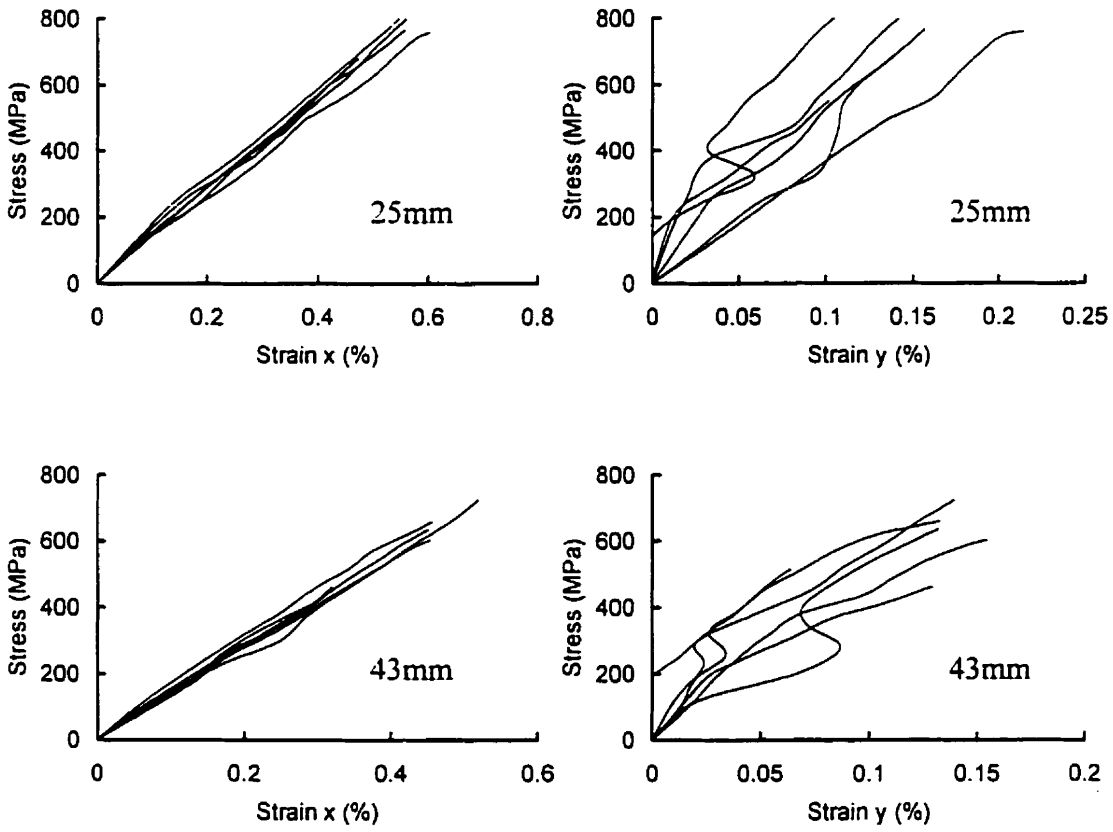

Figure 3.1. Stress-strain responses of $[0]_8$ samples

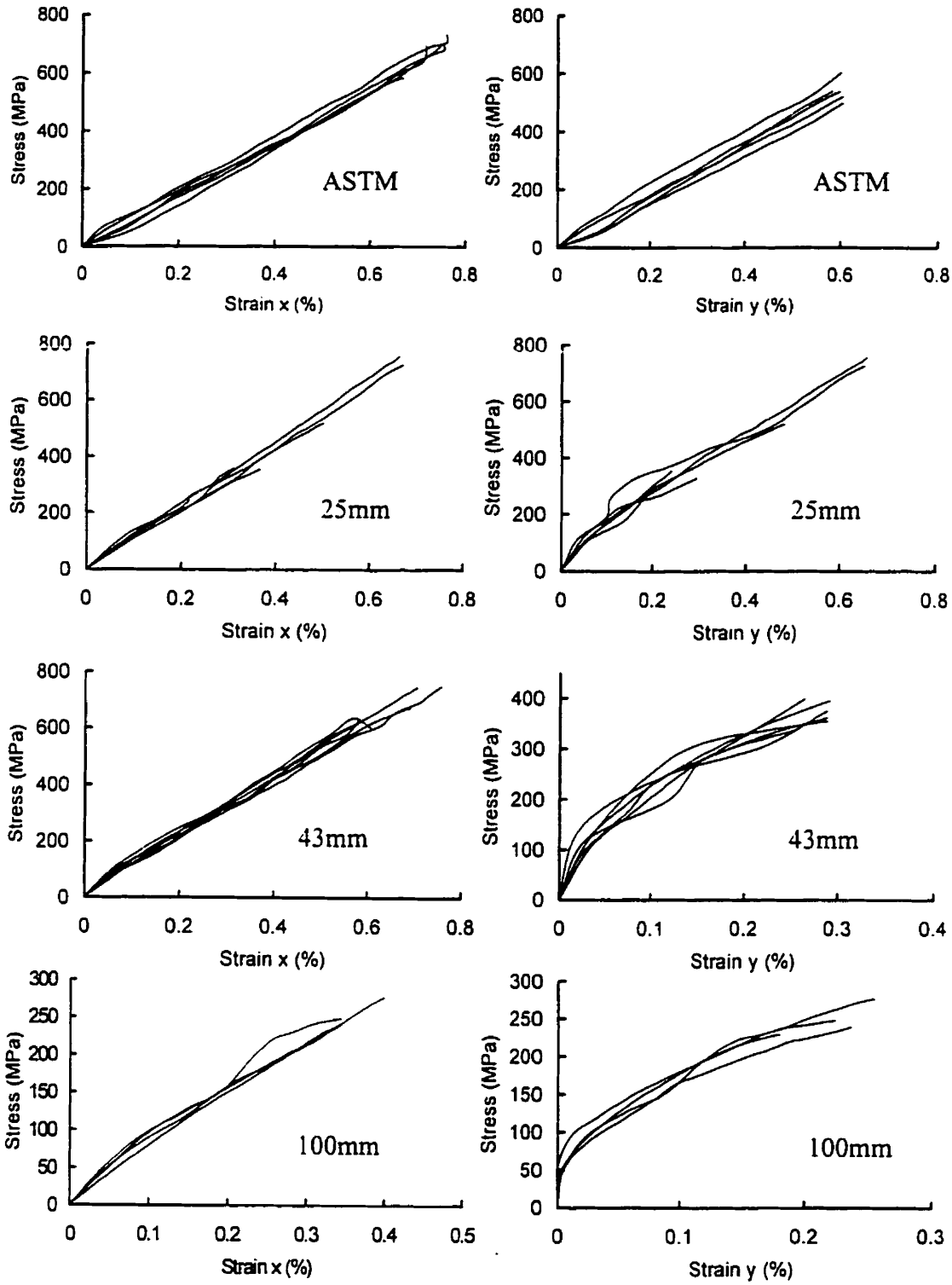

Figure 3.2. Stress-strain responses of $[\pm 15]_{2s}$ samples

Figure 3.1 showed that the stress-strain response in the x direction for the $[0]_8$ laminates was fairly linear for both 25 mm and 43 mm widths. For the 43 mm width both strain and stress were somewhat smaller than for the 25 mm width. The y direction strain responses were far from linear, but sudden changes were accompanied by noise from the specimens of both widths. The y strains were much smaller than the x strains. The 100 mm width samples were tested also but none of them were successful. The samples were pulled out between the sample ends and the holes in the clamp.

For the $[\pm 15]_{2s}$ laminates, shown in Figure 3.2, the ASTM samples showed fairly linear responses both in x and y directions. The x strain responses for both 25 mm and 43 mm samples were moderately linear but with a lower slope than for the $[0]_8$ samples. The y strain responses were less scattered than the $[0]_8$, but the 43 mm width sample had a much higher slope near the origin. Both 25 mm and 43 mm widths gave lower stress at a given strain than the $[0]_8$, although for the $[\pm 15]_{2s}$ the 43 mm sample had y strains which were about half those for the 25 mm samples. The ASTM sample gave even lower stress at a given strain in both x and y directions. Sudden changes in the y strain for the 43 mm width samples were accompanied by cracking sounds. The 100 mm samples also gave roughly linear x stress-strain responses, but the slopes were lower. The y strain slopes were very high initially, but then became lower than those for the 43 mm width.

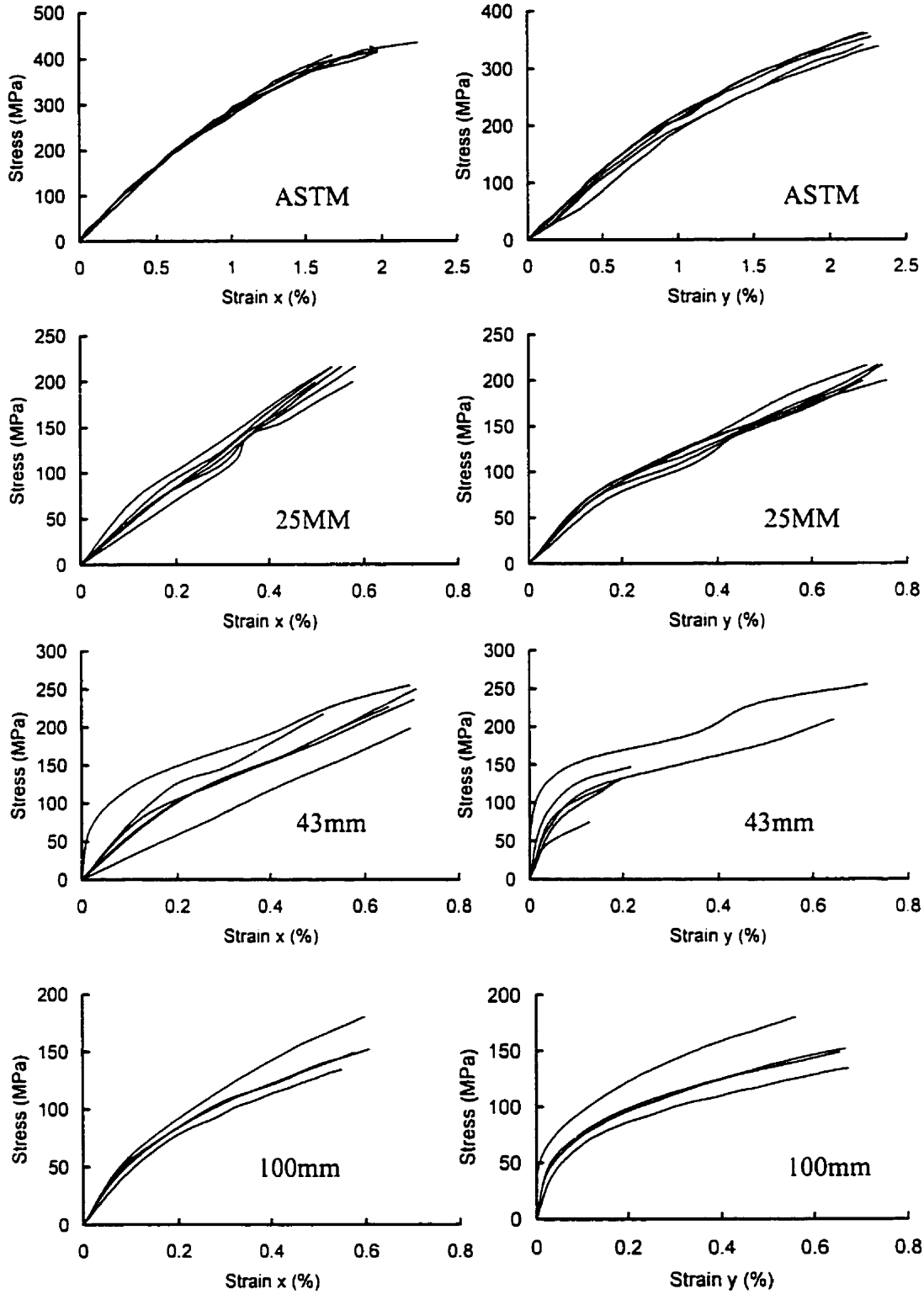

Figure 3.3. Stress-strain responses of $[\pm 30]_{2s}$ samples

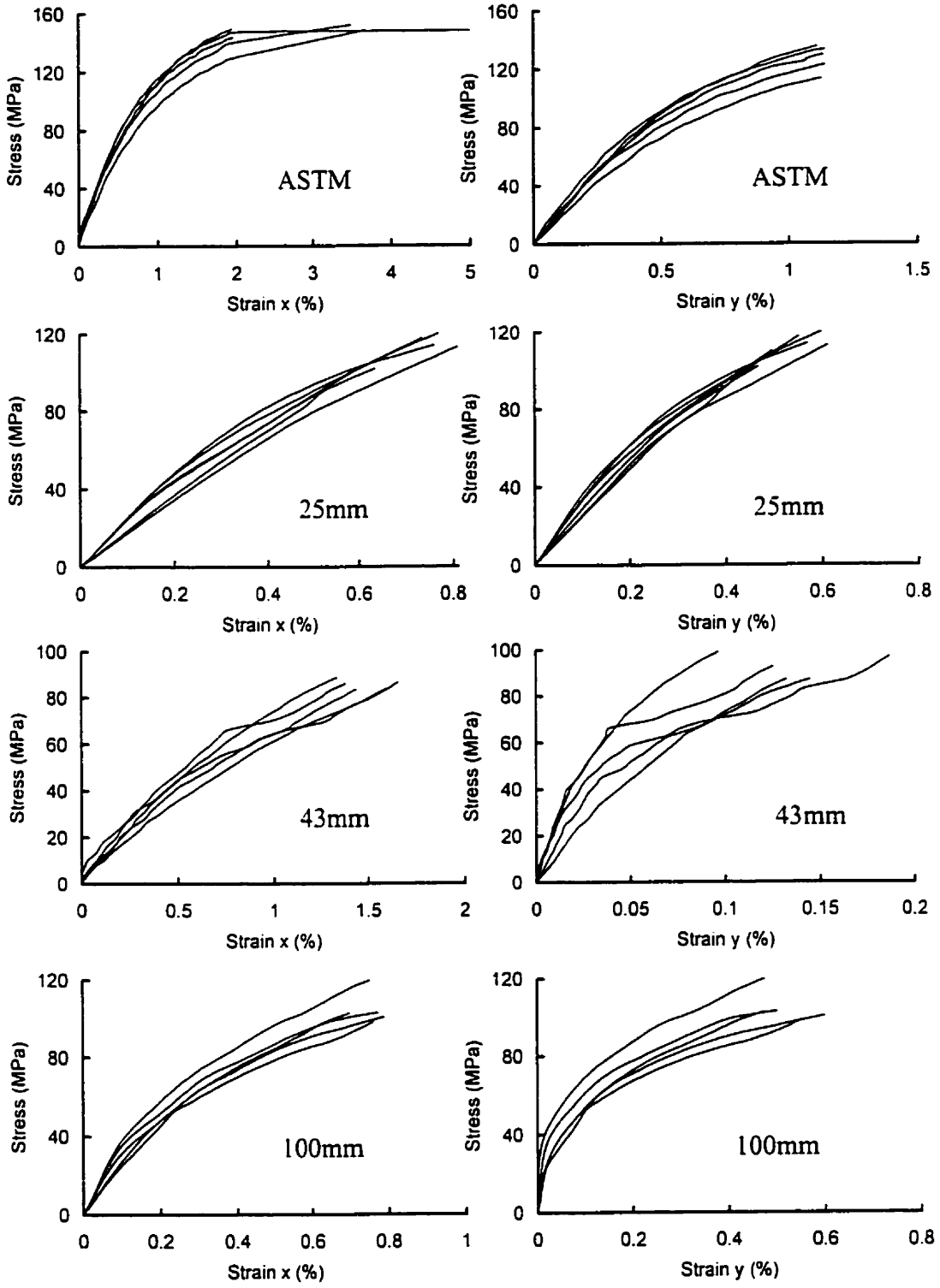

Figure 3.4. Stress-strain responses of $[\pm 45]_{2s}$ samples

In Figure 3.3, which shows the $[\pm 30]_{2s}$ laminates, the stress-strain responses indicated fairly linear relationships in the x direction. The responses had two slopes, the initial slope being the larger. This tendency became clearer with the increasing of sample width in the non-standard samples. Both slopes were significantly smaller than those of the $[\pm 15]_{2s}$. The strains in the y direction had a similar trend as those in the x direction. The slopes in the y direction were much larger than those of the $[\pm 15]_{2s}$. The 43 mm width samples gave more scattered results than the others did, and the sudden changes in the y direction strains were accompanied by cracking sounds. We did not hear these sounds in testing of the ASTM samples. (The stress scales used in Figure 3.3 are different among the different sample widths.)

For the $[\pm 45]_{2s}$ laminates, in Figure 3.4, the x direction stress strain responses showed two slopes linear relations for all the sample widths in which the initial slopes were larger than the second ones. Compared to $[\pm 30]_{2s}$ samples, the lower slopes, both the initial and the second, were observed here in the x direction. In the y direction, moderately linear stress strain relations with two slopes were observed. The slopes near the origin were bigger than the second ones. The y strains were smaller than the x strains under given stresses. Different strain stress scales have been used in the figure. The 43 mm width samples were tested under a load control mode of 2.3 kN/min. (The others were tested under the stroke control mode as specified in Section 2.2.1.) The wider specimens gave more scatter results.

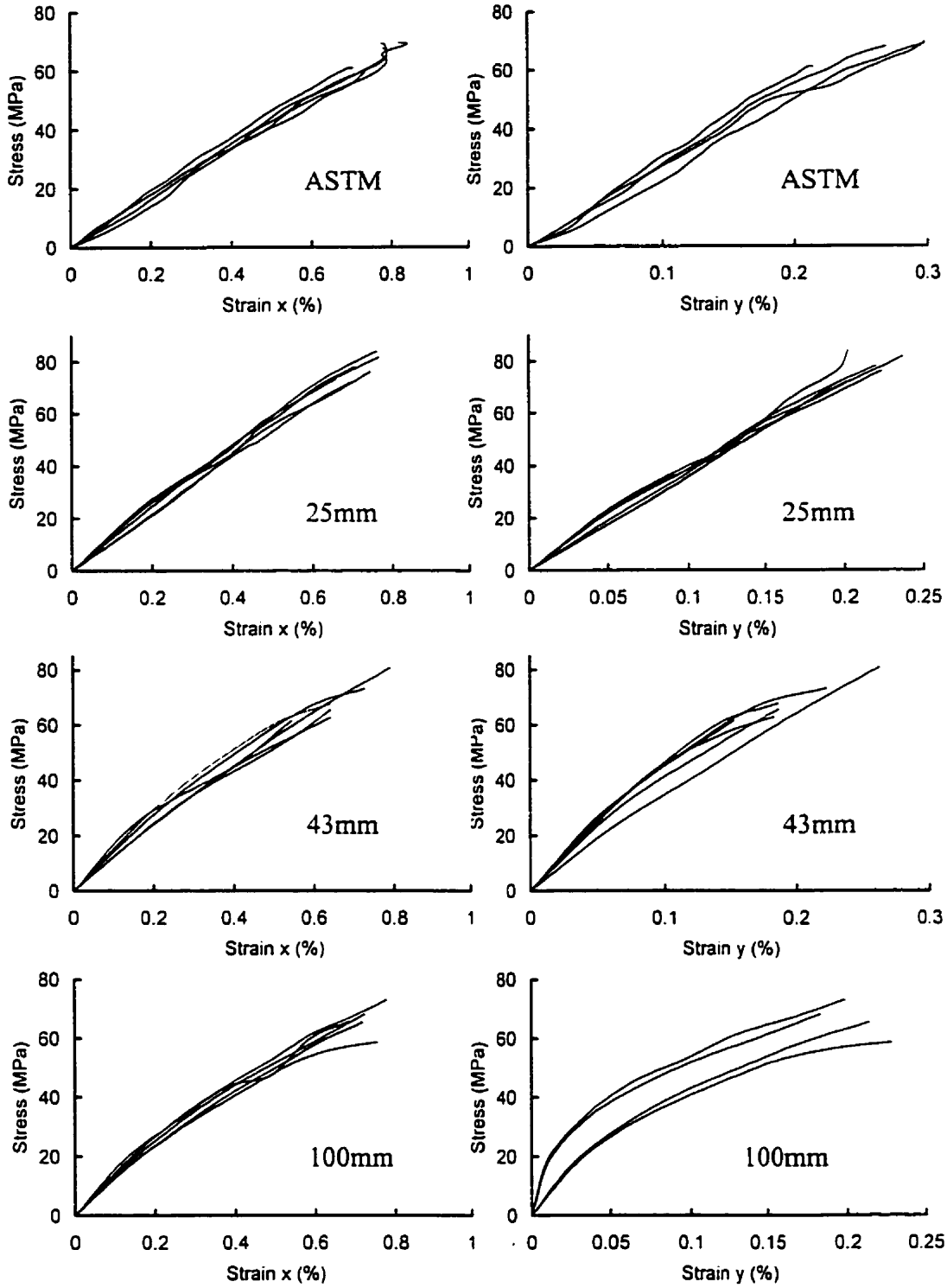

Figure 3.5. Stress strain responses of $[\pm 60]_{2s}$ samples

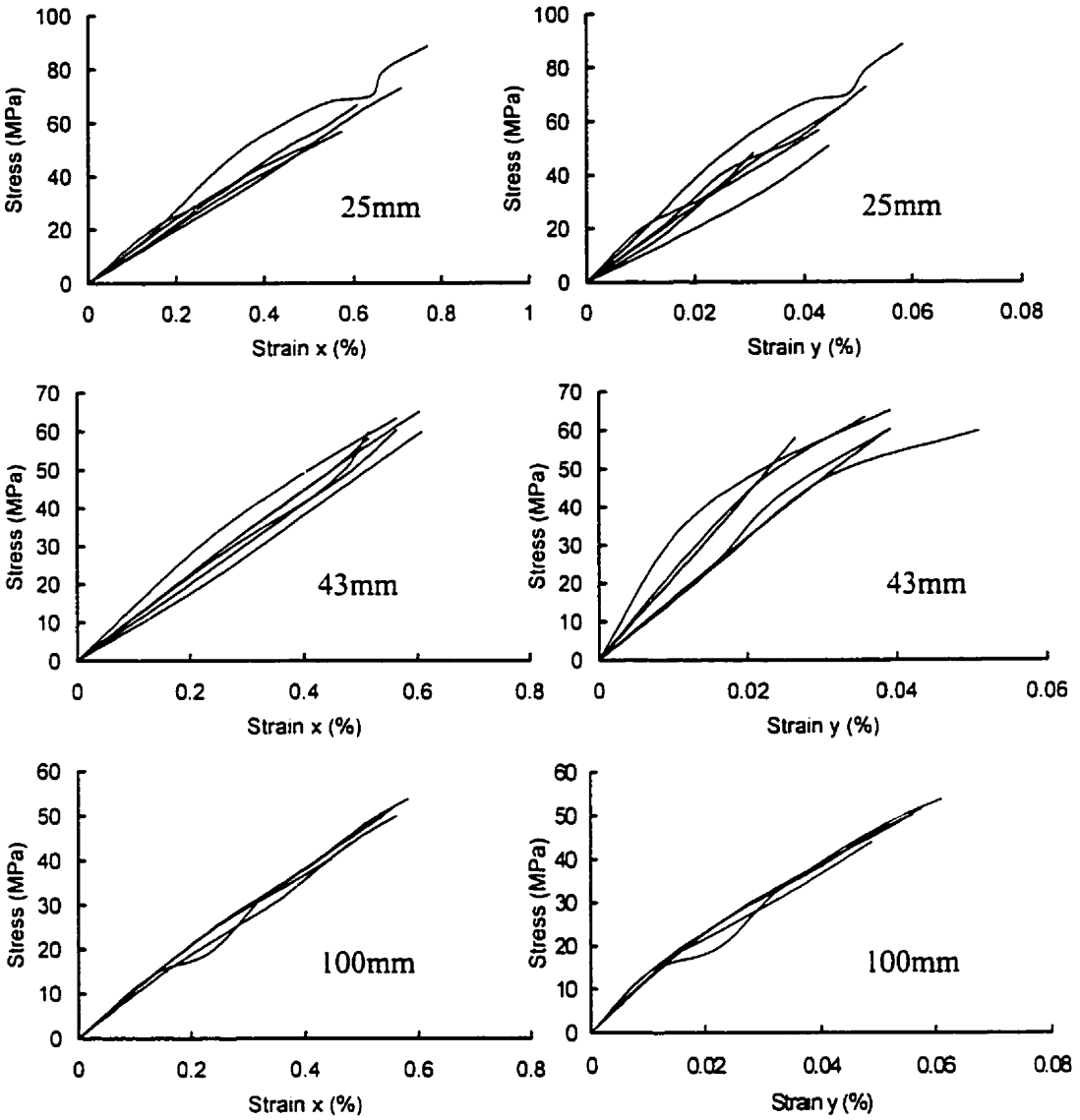

Figure 3.6. Stress strain responses of $[\pm 75]_{2s}$ samples

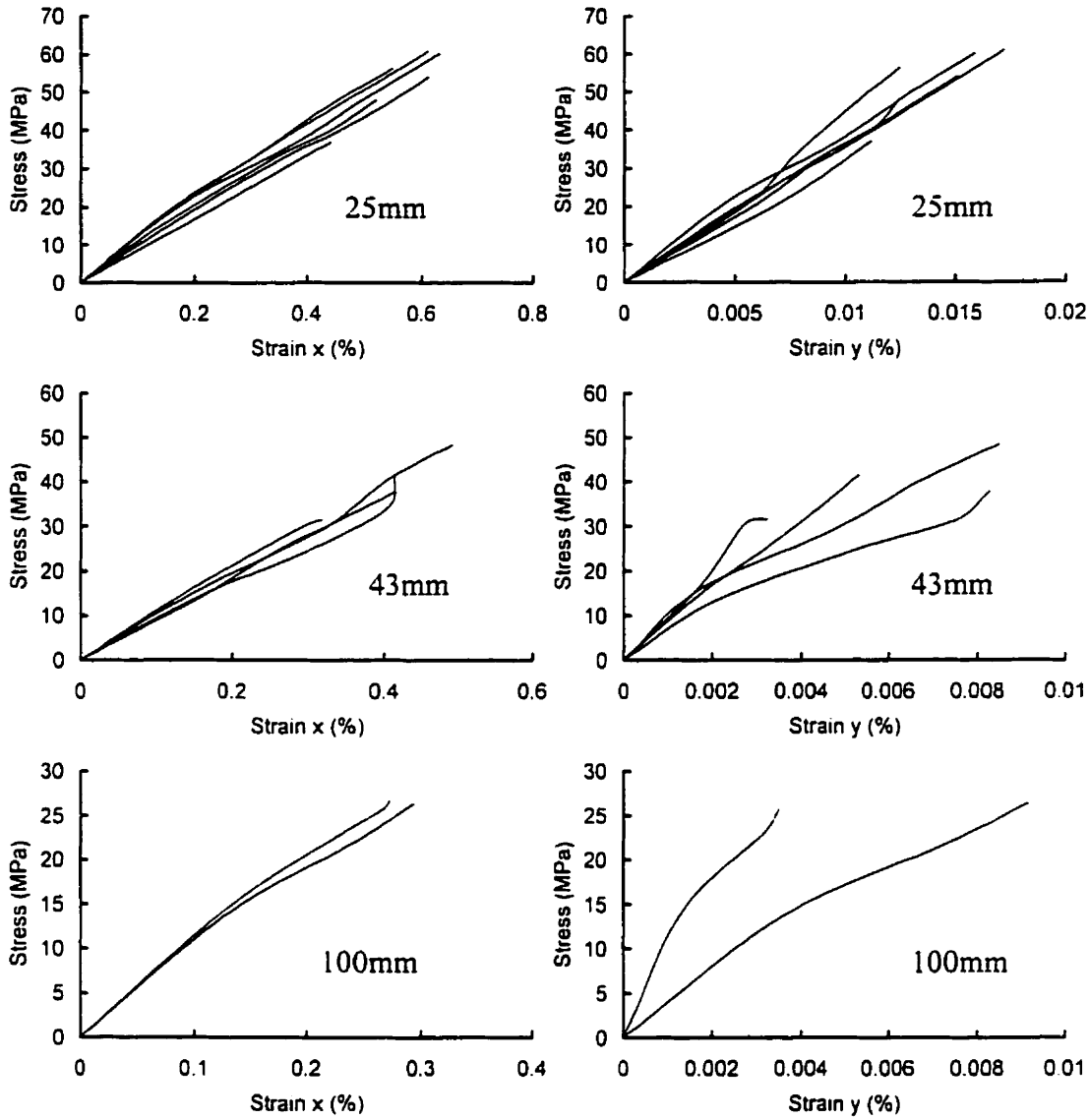

Figure 3.7. Stress strain responses of $[90]_8$ samples

In Figure 3.5, the $[\pm 60]_{2s}$ laminates, fairly linear stress strain relations were observed in the x direction. The ASTM and 25 mm width samples appeared more linear than the 43 mm and 100 mm samples that gave two slopes and the initial slopes were larger than the second ones. The y direction stress strain relationships had a similar trend to those of the x direction. The lines with 2 slopes in the 43 mm and 100 mm samples became more obvious than those in the x direction. Different strain scales have been used in the figure.

The $[\pm 75]_{2s}$ laminates, in Figure 3.6, showed moderately linear stress strain relations for all the widths in the x direction. In the y direction they also showed fair linearity but with some slope changes in the 43 mm and 100 mm samples. The 25 mm and 43 mm samples gave more scattered results than the 100 mm ones. Different stress strain scales have been used in the figure.

In Figure 3.7 the $[90]_8$ laminates showed fairly linear stress strain relations in the x direction in general. The 100 mm samples had two slope curves with the initial slope larger than the second one. The 25 mm samples showed linear stress strain responses in the y direction. The 43 mm samples gave fairly linear response with the slope made smaller, but the results were scattered. The 100 mm samples had similar y stress strain responses as did the 43 mm samples. Six 100 mm width specimens were tested but only two were successful.

3.2. Stress-Strain Response in the Compressive Test

The compressive test results are shown in Figures 3.8 a and b. In Figure 3.8b, 0.05mm Teflon films were placed between the sample and the platens, and the sample was retested after the test. The results are shown in Figure 3.8a. The strain gauge 1, 3, 5 were in the x direction where the load applied. The strain gauge 2, 4, 6 were in y direction. The specimen aspect ratio, the specimen gauge length over the specimen width, was about the same as those of the 43 mm width tensile sample.

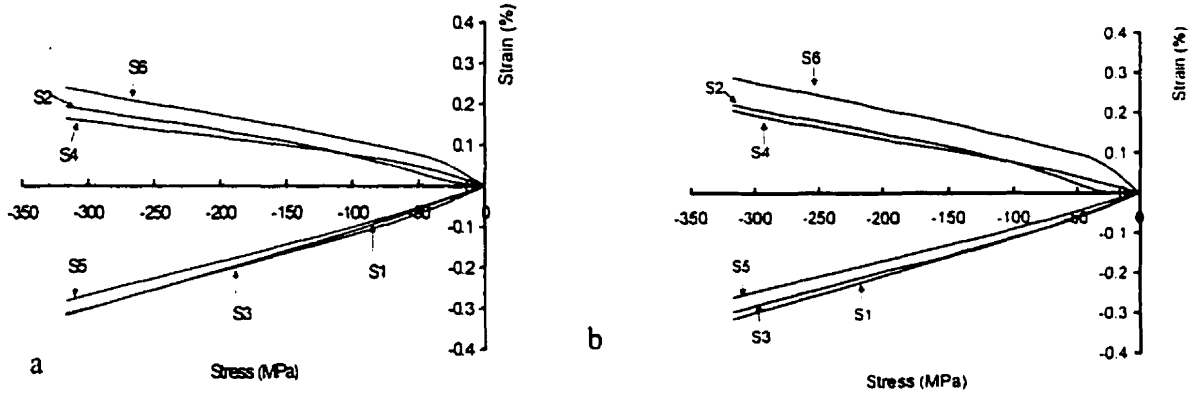

Figure 3.8. Compressive stress strain responses of $[\pm 15]_{6s}$ sample

The stress strain responses in x direction were very similar to the tension response in Figure 3.2. The strain responses in different positions had similar patterns but different values. There was no significant difference between the x strains with and without Teflon film.

However the strain responses in y direction were quite different from the tension, see Figure 3.2, being almost linear except for an initial build up in strain gauge 6 which was at an edge of the specimen. After putting the Teflon film the y strain increased significantly in the case of strain gauge 6 but had only a small increase in the other two.

3.3. Tensile Strength

The angle ply laminates tensile strengths are shown in Figure 3.9 and Table A2 to Table A5 in the Appendix. The $[0]_8$, $[\pm 15]_{2s}$, and $[\pm 30]_{2s}$ short wide samples were tested for strength some days after the elasticity tests. The rest were tested for strength at the same time as the elasticity tests. Note that in this and subsequent figures, the data are offset slightly to avoid overlap.

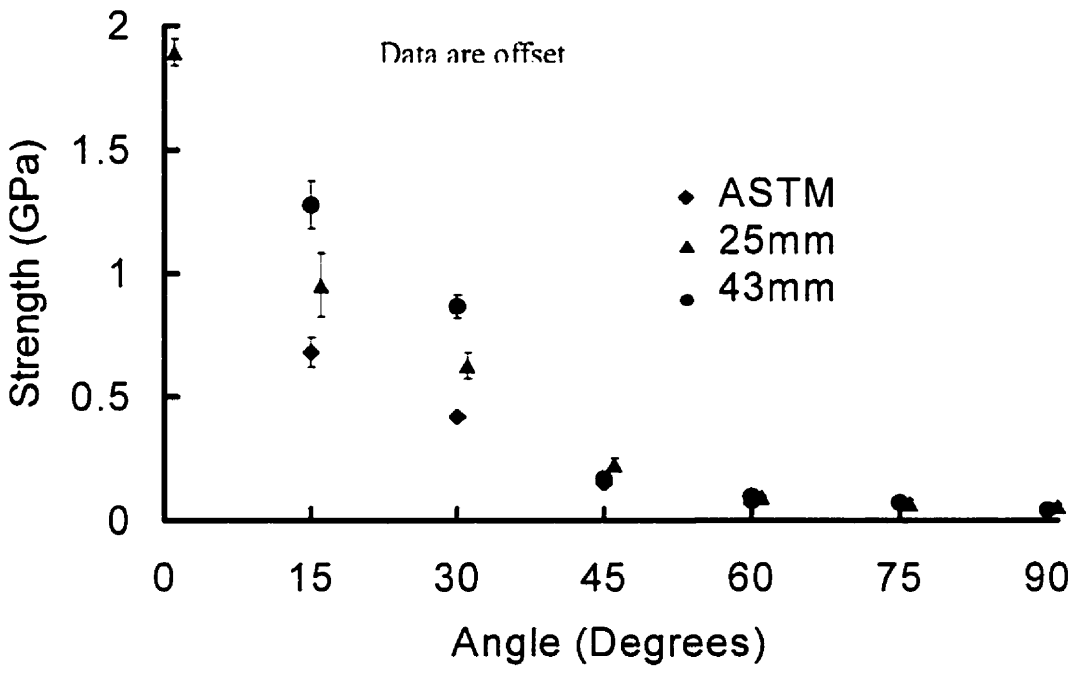

Figure 3.9. Tensile strength of angle ply laminates

The wide specimens had higher tensile strength than the narrow ones when the lay-up angles were less than 60^0. Different width samples gave almost the same strengths at 60^0 and 75^0 lay-up angles, the differences were within test errors. The wide sample gave less strength than the narrow one in the $[90]_8$ lay-up. The $[0]_8$ strength was from the 25 mm width specimens because we could not break the 43 mm samples even when they were notched. The clamp used for the 100 mm width samples could not be used to break the samples. The samples were always pulled out between the edges and the holes. There are no strength data for the 100 mm width samples.

3.4. Ultimate Tensile Strain

The ultimate tensile strains of the angle ply laminates are shown in Figure 3.10 and Table A2 to Table A5 in the Appendix. The strains are the strain gauge readings in the x direction when the specimens were broken.

As in the strength results, the ultimate strain of $[0]_8$ laminates was obtained from the 25 mm width samples. In the lay-up angle $\pm 15^0$, the results from different width samples were quite close to each other and the wide sample had higher ultimate strain. The strains were all less than that in the 0^0. The ultimate strains appeared higher in the $\pm 30^0$ than those in the $\pm 15^0$ but had the same trend, which is that the wide specimen had higher ultimate strain than the narrow one. The ultimate strain difference among the different specimen widths became bigger. The 25 mm width specimens gave an ultrahigh

ultimate strain in the $\pm 45^0$ lay-up, which is about 6%. The 43 mm width specimens gave the lowest. The 25 mm and the ASTM samples gave higher ultimate strains than those in the $\pm 30^0$ while the 43 mm samples gave the lower result. In the $\pm 60^0$, the results were similar to the $\pm 15^0$ but the narrow specimens gave lower ultimate strains while the wider one gave higher result. The differences among the results from different sample widths were small. The $\pm 75^0$ and 90^0 lay-ups gave similar results. The differences between different specimen widths were within the test errors.

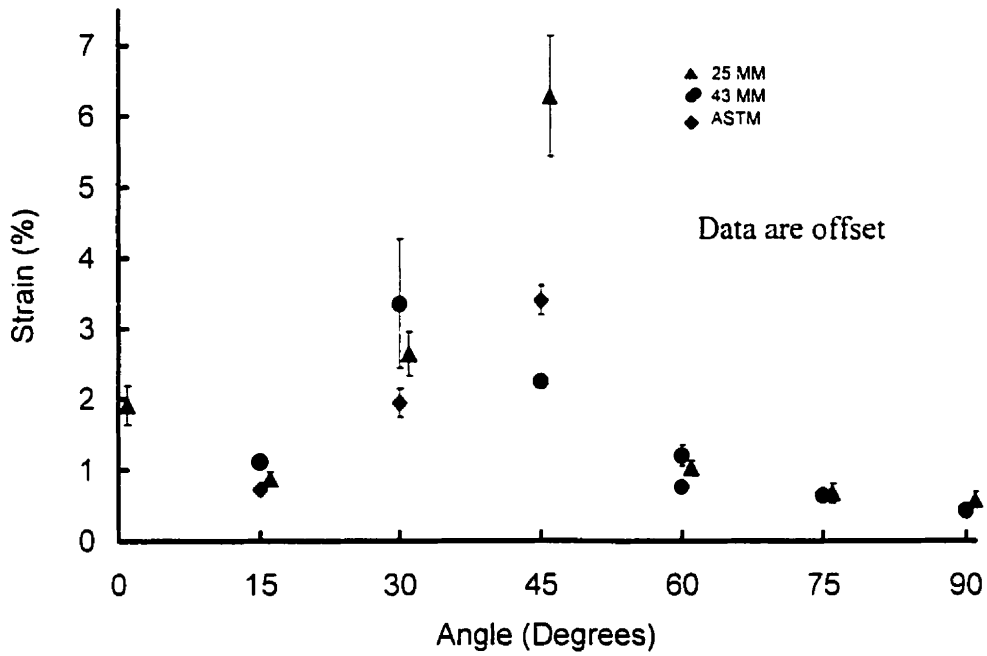

Figure 3.10. Ultimate tensile strains of angle ply laminates

3.5. Fracture Image of the Angle Ply Laminates

The broken tensile specimens are shown in Figures 3.11 to 3.17. The photos were taken after the tensile tests. The clamp tooth prints visible on the end tabs mean nothing since the end tabs were reused. The specimens were clamped so that they kept the right gauge lengths.

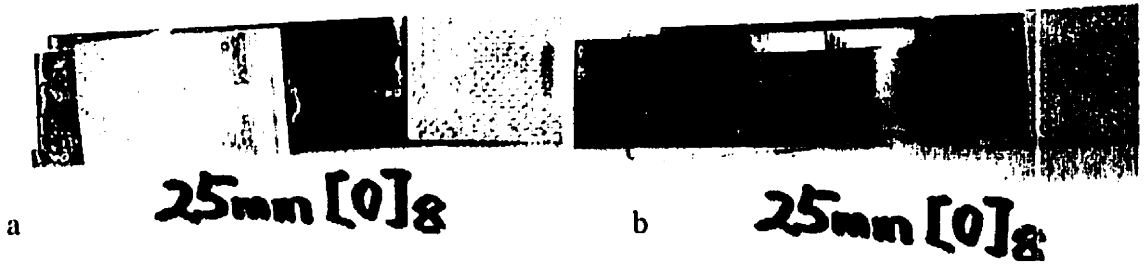

Figure 3.11. Fractures of $[0]_8$ samples

Figure 3.12. Fractures of $[\pm 15]_{2s}$ samples

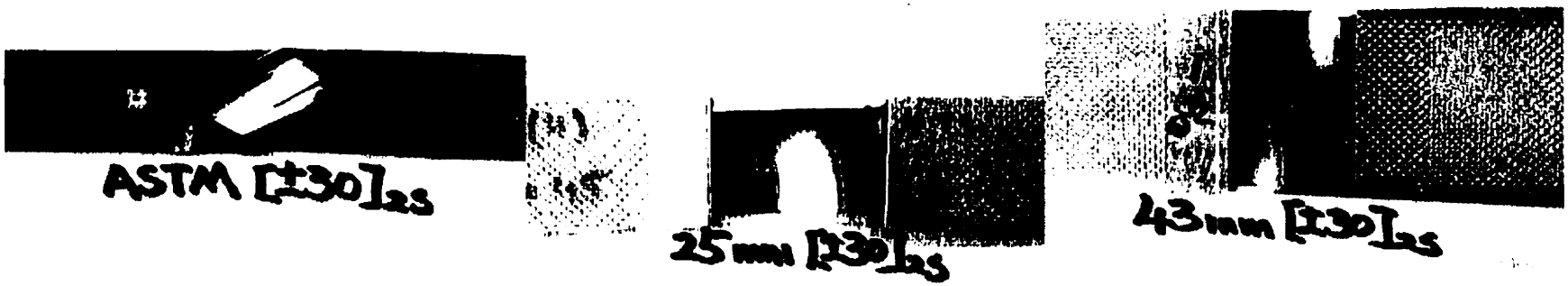

Figure 3.13. Fractures of $[\pm 30]_{2s}$ samples

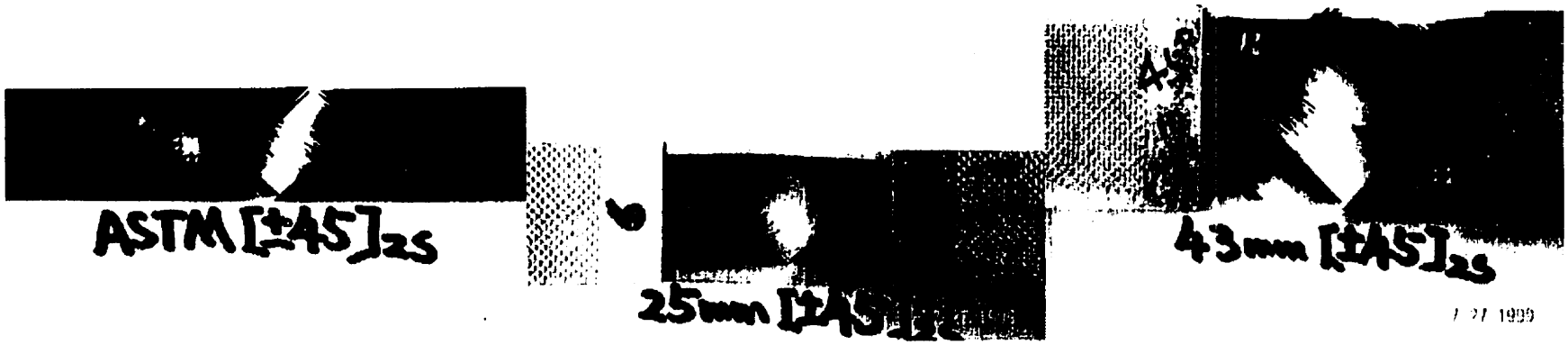

Figure 3.14. Fractures of $[\pm 45]_{2s}$ samples

Figure 3.15. Fractures of $[\pm 60]_{2s}$ samples

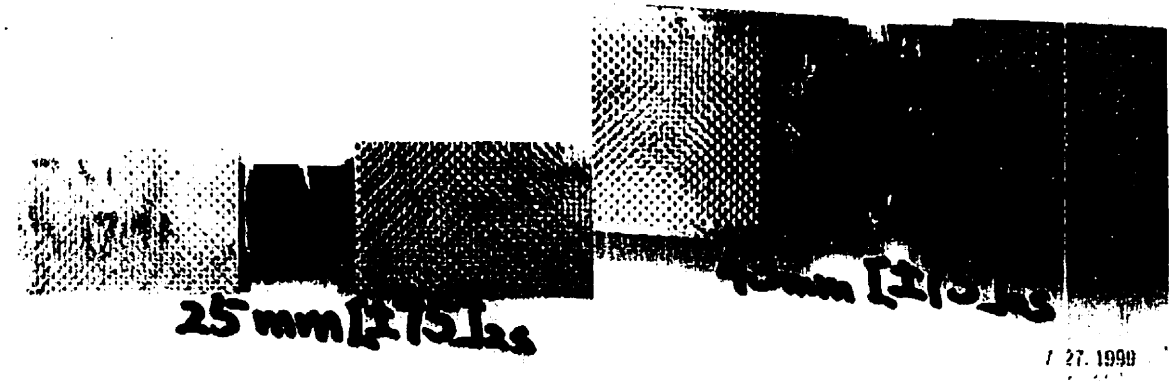

Figure 3.16. Fractures of $[\pm 75]_{2s}$ samples

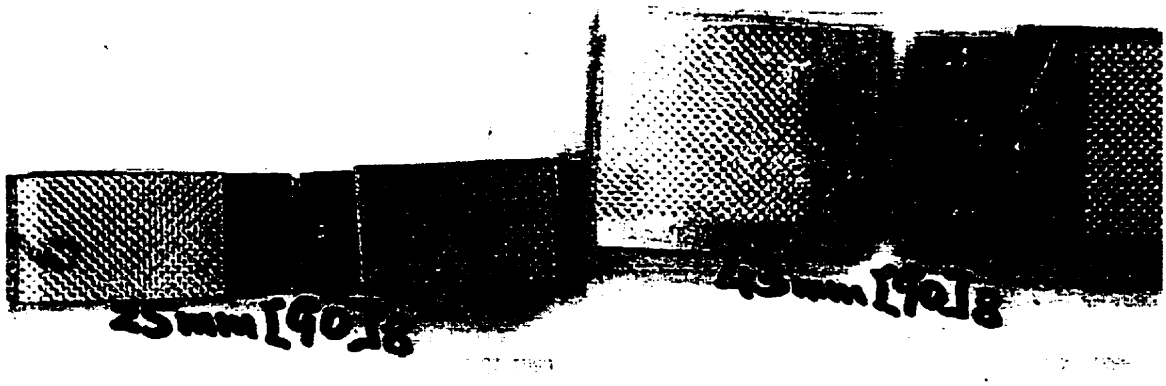

Figure 3.17. Fractures of $[90]_8$ samples

Three different failure patterns were observed in the fractures. They were:

- Total fiber failure. In this pattern, all the fibers were broken.
- Half fiber failure. In this pattern, only the fibers along one ϕ direction were broken. In the other direction fiber was split apart.
- Matrix failure. The failure occurred only in the matrix, no fiber was broken but fibers were split apart.

The observation and the measurements of the sample failure are listed in table 3.1. The measurements were along the specimen width (y direction) where the broken happened.

3.6 Photoelastic Tests

Table 3.2 gives the fringe orders corresponding to the colors seen on the images.

3.6.1. Photoelastic Fringe Pattern in Tension

The photoelastic images in tension are shown in Figures 3.18, and 3.20 to 3.21. Figure 3.19 shows a sequence of photoelastic images for $[\pm 45]_{2s}$ at various stresses. Figure 3.21 shows the images while the laminates were in an entirely elastic region. Figure 3.22 shows the images when the laminates were in the non-elastic region. The whole photoelastic images can be found in the Appendix A2.1. Due to the low printer resolution some of the detailed information have not been present well in the figures.

Table 3.1. Specimen fracture patterns

Lay-up	Specimen width (mm)	Fracture Description	Fracture Measurement		
			Total (mm)	Half (mm)	Matrix (mm)
$[0]_8$	25	Total fiber failure and matrix failure	25	-	-
$[\pm 15]_{2s}$	ASTM	Total fiber failure and half fiber failure	-	25	-
	25	Total fiber failure and half fiber failure	20±2	5±1	-
	43	Total fiber failure and half fiber failure	38±4	5±1	-
$[\pm 30]_{2s}$	ASTM	Half fiber failure	-	25	-
	25	Total fiber failure and half fiber failure	17±2	8±1	-
	43	Total fiber failure and half fiber failure	35±3	8±1	
$[\pm 45]_{2s}$	ASTM	Half fiber failure	-	25	-
	25	Half fiber failure	-	25	-
	43	Half fiber failure	-	43	-
$[\pm 60]_{2s}$	ASTM	Half fiber failure	-	25	-
	25	Half fiber failure	-	25	-
	43	Half fiber failure	-	43	-
$[\pm 75]_{2S}$	25	Half fiber failure	-	25	-
	43	Half fiber failure	-	43	-
$[90]_8$	25	Matrix failure	-	-	25
	43	Matrix failure	-	-	43

The fine horizontal lines appearing on the photo prints were from the printer and were not on the original images. The printer could not print out some very fine details. The images showed the photoelastic coating as being 43mm wide and 20mm long.

The readings from the strain gauge on the back of the specimens, corresponding to the photoelastic images in Figure 3.18, are plotted in Figure 3.19. Because the MTS machine could not hold the load steady, the load or the stresses shown in the photoelastic images in tension were not constant. The readings from the strain gauge kept changing when the machine was held at constant load. Thus an average reading from the strain gauge was taken, especially for the strains in the y direction.

The light source was on the left side of the polariscope and it appeared too strong, so the images did not show the detailed information on the left side. Since the development of the film and the photos was not under our control, the colors appearing in the photos may differ from the true colors. But we still could recognize them since the colors should appear in sequence as listed in Table 3.2.

Table 3.2. Fringe orders corresponding to colors

Color	Fringe Order (N)	Color	Fringe Order (N)
Black	0	Rose Red	1.82
Gray	0.28	Purple	2.00
White	0.45	Green	2.35
Pale Yellow	0.60	Green-Yellow	2.50
Orange	0.80	Red	2.65
Dull Red	0.90	Red/Green	3.00
Purple	1.00	Green	3.10
Deep Blue	1.08	Pink	3.65
Blue-Green	1.22	Pink/Green	4.00
Green-Yellow	1.39	Green	4.15

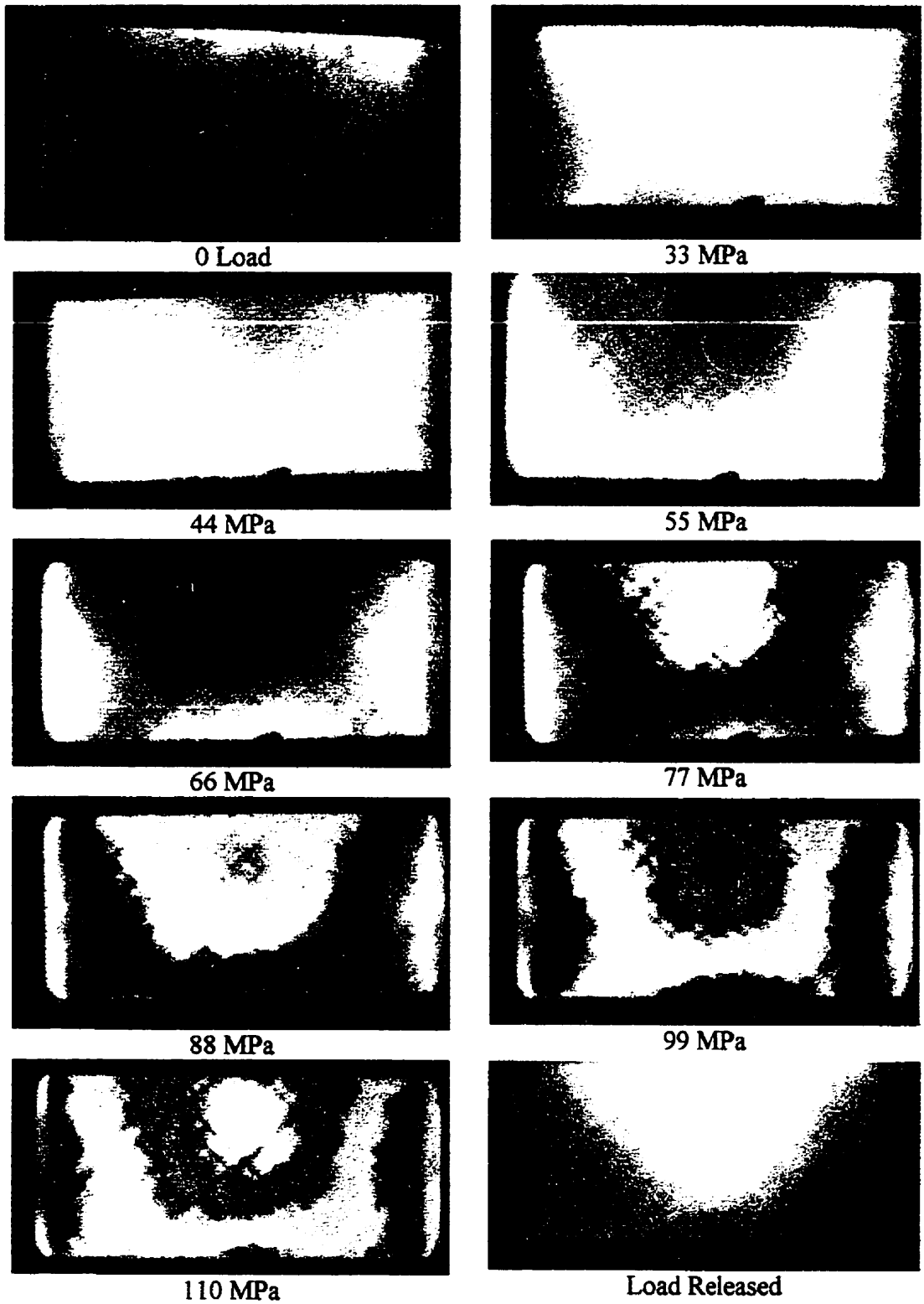

Figure 3.18. Photoelastic fringe patterns of $[\pm 45]_{2s}$ sample

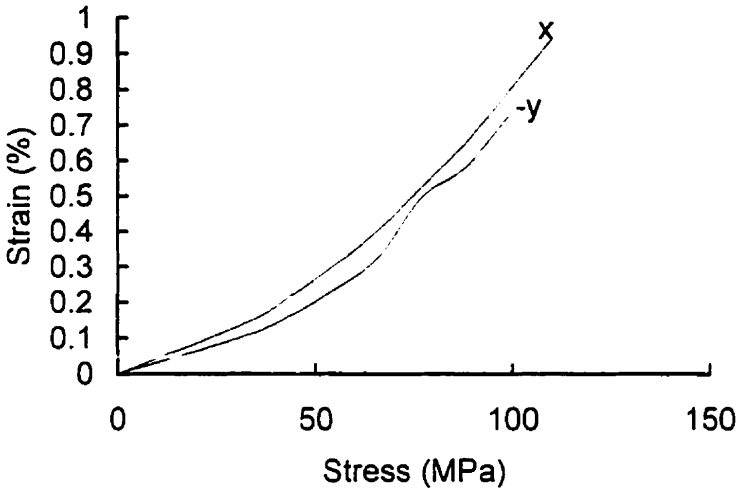

Figure 3.19. Strain gauge readings with the photo images in Figure 3.19

In Figure 3.18, at 33 MPa the strain was roughly uniform, as indicated by no or very little pattern. At higher stresses strain non-uniformity appeared with the highest stress being near the center of the sample near the upper grip. At 66 MPa, the material was showing inelastic behavior (see Fig. 3.4.), and fibers were showing their presence in the pattern, in the dull red and deep blue regions and this continued up to the highest stress. At 66, 77, and 88 MPa, the deep blue color indicates a fringe order of 1.08. The green color appearing at 99 and 110 MPa corresponded to a fringe order of 2.35. The highest fringe order of 2.65 was observed at 110 MPa represented by the red color in the center near the upper grip. When the load was released white color still appeared on the sample indicating the residual stress caused by the plastic deformation.

A similar sequence could be seen at other laminate samples, but very little fiber presence was seen at $[0]_8$ and $[90]_8$.

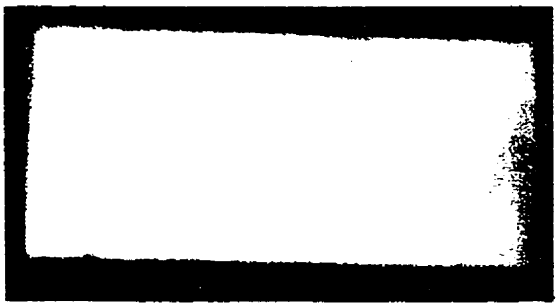

$[0]_8$ with 200 MPa (ε_x=0.144%, ε_v=0.08%)

$[\pm 15]_{2s}$ with 100 MPa (ε_x=0.088%, ε_y= 0.06)

$[\pm 30]_{2s}$ with 80 MPa (ε_x=0.165%, ε_y=0.153%)

$[\pm 45]_{2s}$ with 33 MPa (ε_x=0.147%, ε_v=0.111%)

$[\pm 60]_{2s}$ with 17 MPa (ε_x=0.123%, ε_v=0.143%)

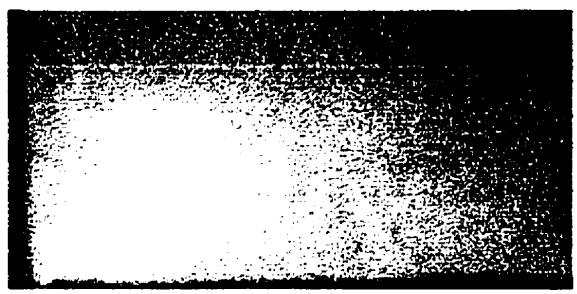

$[\pm 75]_{2s}$ with 25 MPa (ε_x=0.076%)

$[90]_8$ with 17 MPa (ε_x=0.106%)

Figure 3.20. Photoelastic fringe patterns of angle ply laminates within elastic range

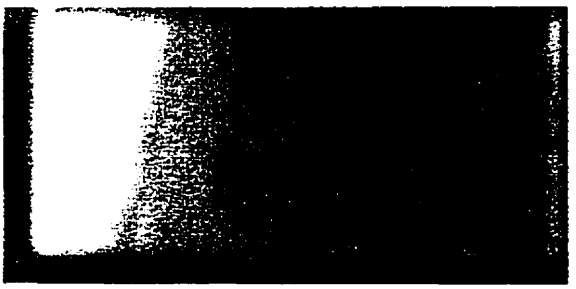

$[\pm 15]_{2s}$ with 350 MPa (ε_x=0.348%, ε_v=0.323%)

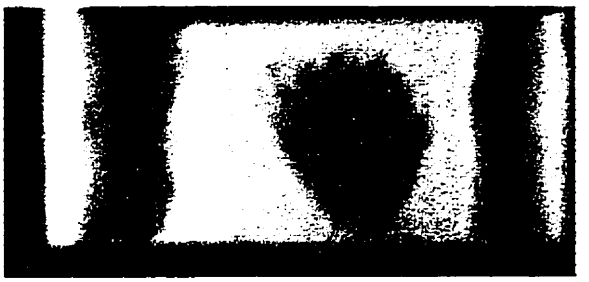

$[\pm 30]_{2s}$ with 200 MPa (ε_x=0.637%, ε_v=0.757%)

$[\pm 45]_{2s}$ with 99 MPa (ε_x=0.769%, ε_v=0.727%)

$[\pm 60]_{2s}$ with 73 MPa (ε_x=0.747%, ε_v=0.285%)

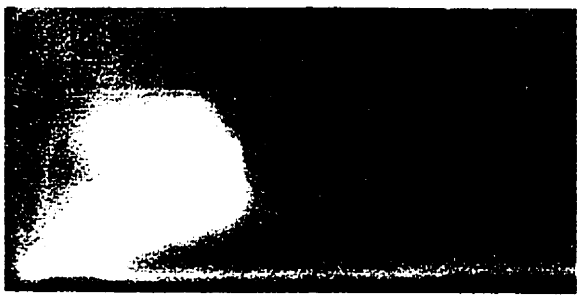

$[\pm 75]_{2s}$ with 72 MPa (ε_x=0.294%)

Figure 3.21. Photoelastic patterns of angle ply laminates in non-elastic range

In Figure 3.20 the strains were uniform in the gauge area. The fringe patterns did not show the fiber presence or then showed little fiber presence. The highest fringe order shown in the figure is about 0.60, represented by the pale yellow color. Some stress concentrations along the upper and bottom edges of the gauge area could be observed in

the $[0]_8$, $[\pm 15]_{2s}$, $[\pm 45]_{2s}$, and $[\pm 75]_{2s}$ samples. The light spot shown on the $[\pm 60]_{2s}$ and $[\pm 75]_{2s}$ samples was due to the reflections of the light source.

When the loads went higher, the sample deformed plastically as shown in Figures 3.2 to 3.6. The fringe patterns indicated non-uniformed stresses had developed in the gauge areas in Figure 3.21. The fiber presence was also shown by the fringe patterns. This was obvious in the $[\pm 15]_{2s}$, $[\pm 30]_{2s}$, $[\pm 45]_{2s}$, and $[\pm 75]_{2s}$ lay-ups. The principal stress directions were along the fiber lay up directions. The highest stress areas were on the right side for the $[\pm 15]_{2s}$, in the middle on the bottom for the $[\pm 30]_{2s}$, in the middle on the top for the $[\pm 45]_{2s}$ and $[\pm 60]_{2s}$, and in the middle for the $[\pm 75]_{2s}$. The highest fringe orders shown were 1.08, 4.15, 2.35, 1.08 and 1.08 for the $[\pm 15]_{2s}$, $[\pm 30]_{2s}$, $[\pm 45]_{2s}$, $[\pm 60]_{2s}$ and $[\pm 75]_{2s}$ respectively. The readings from the strain gauges on the back of the specimen are shown with the fringe patterns.

3.6.2. Photoelastic Fringe Pattern in Compression

In Figure 3.22, the photoelastic fringe patterns in compressive are compared with those in tension for similar stresses. The strain gauge readings in the middle position are listed under the patterns for the compression. The readings from other positions can be found in Figure 3.8.b. The strain readings for the tension fringe patterns are listed under the patterns. The whole images can be found in Appendix A2.2.

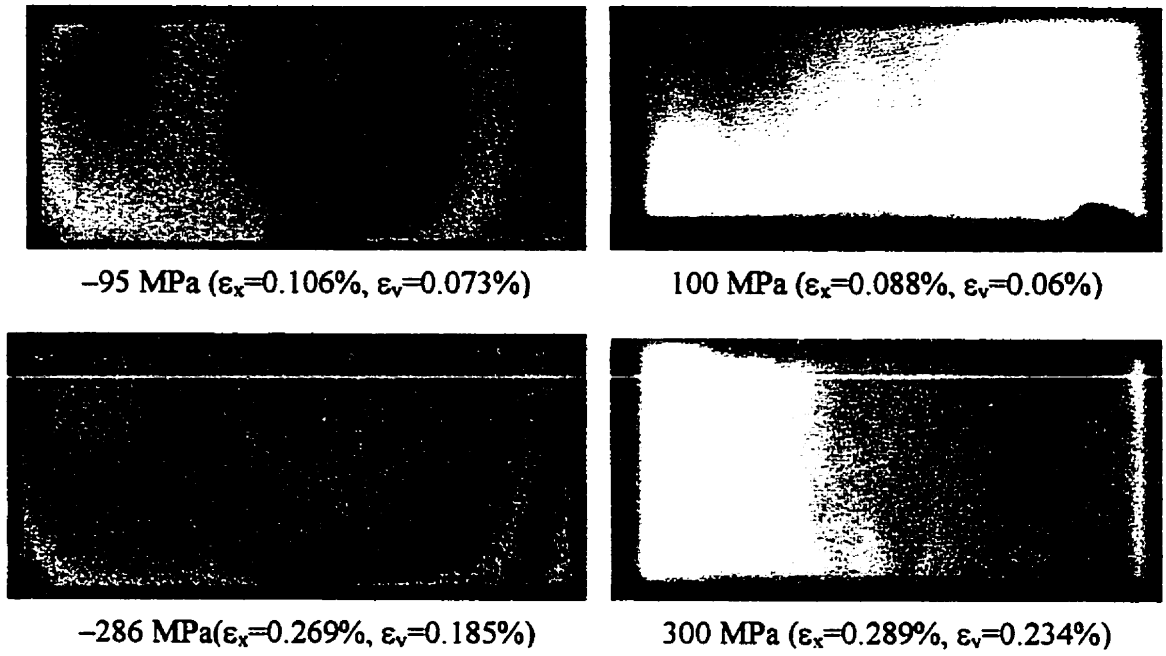

Figure 3.22. Comparison of $[\pm 15]_{2s}$ photoelastic fringe patterns in compression and tension

The tensile and compressive tests gave different fringe patterns as shown in Figure 3.22. When the load were around 100 MPa, the fringe pattern showed more uniform stress developed in the gauge area in the tension than in the compression. No fiber presence was shown in the compression but little fiber presence was shown in the tension. The strains in the x and the y directions were smaller in the tension than those in the compression. The highest fringe orders were 1.39 and 0.45 in the compression and the tension respectively. When the load was around 300 MPa, the fiber presence in tension became more obvious but no such pattern was observed in the compression. The strain readings from the gauges became bigger in the tension than those in the compression. Both compression and tension fringe patterns showed that the principal stresses were along the fiber lay-up directions of $\pm 15^0$.

4. DISCUSSION

In this section we shall establish the significance of the test results before we discuss any of them. We shall then discuss the elastic constants beginning with stress strain relationships of the angle ply laminates, from which the elastic constants, stiffness and Poisson's ratio, will be worked out. After that the yielding of the test samples will be discussed in conjunction with the photoelastic images. Later, angle ply laminate strengths and failure strains will be discussed. Then the model to describe angle ply laminate stiffness and strength will be developed.

4.1. Reliability of the Trends

It is appropriate to check the reliability of the test results before we discuss them. The stiffness discussed here is the stiffness calculated using the initial slope from the origin to just before the first kink or the first sign of curvature in the stress strain curve. The same approach is used to calculate the Poisson's ratio. The values thus calculated are given in Tables A2 to A5 in the Appendix.

4.1.1. Coefficients of Variation

The coefficients of variation for stiffness were mostly about 10% to 15% with the maximum variation about 27% for the 43mm specimens at 30^0, see Figure 4.1. The variations of the apparent Poisson's ratio were much higher, i.e. around 10% to 30% in most cases with the 100 mm specimens giving the highest variations except the 25 mm

specimens at 0^0 which gave about 70%; see Figure 4.2. Note that the ASTM samples were not used for tensile tests of the 0^0, 75^0, and 90^0 laminates. Also the 0^0 laminate was not tested at width of 100 mm.

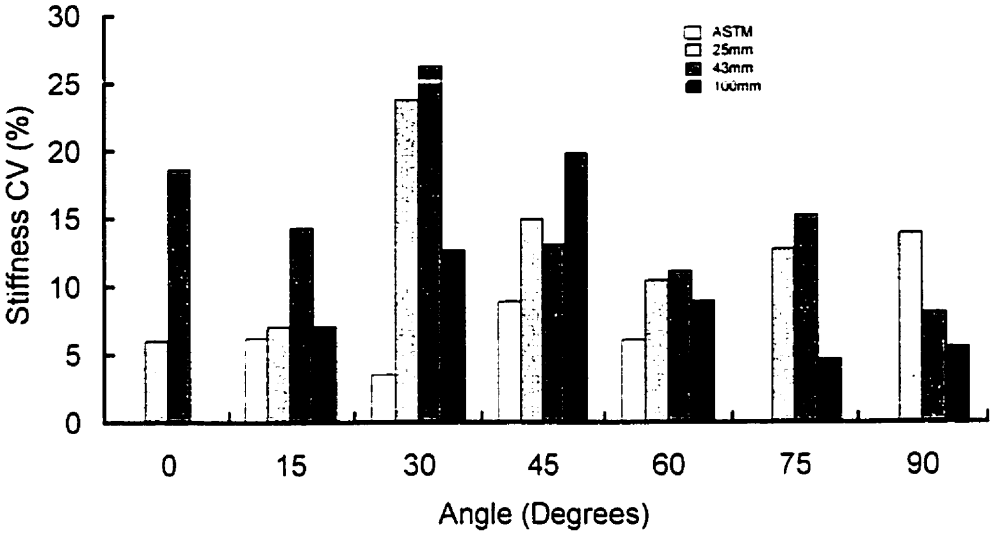

Figure 4.1. Coefficients of Variation for stiffnesses

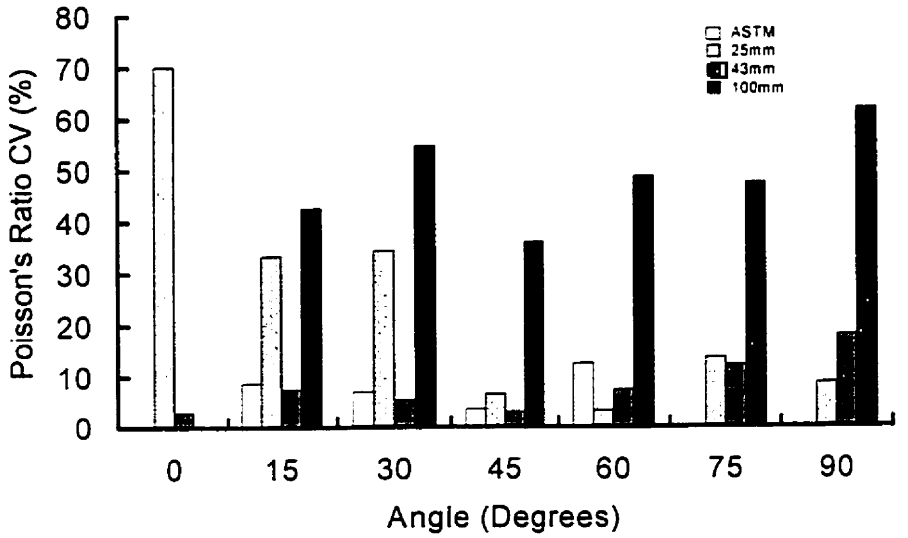

Figure 4.2. Coefficients of variation for apparent Poisson's ratios

The strength coefficients of variation were around 10% to 15% when the lay up angles were less than 60^0. The bigger angles generated higher variations. see Figure 4.3. The failure strain variations were less than 15% to 20% except for the 43 mm specimen at 30^0 which gave about 27%; see Figure 4.4.

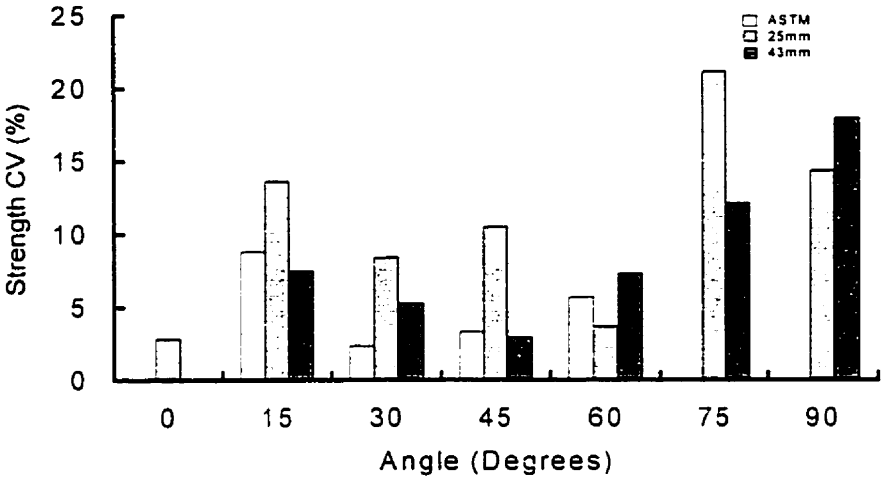

Figure 4.3. Coefficients of variation for strengths

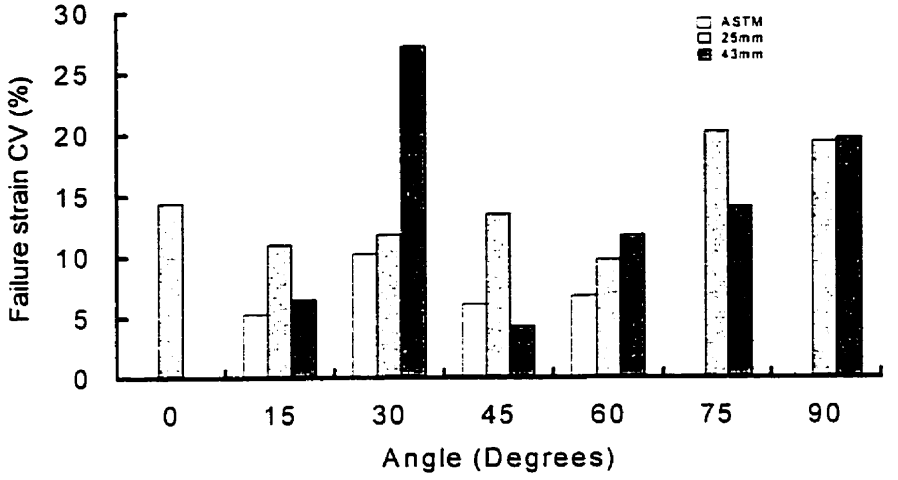

Figure 4.4. Coefficients of variation for failure strains

Since the variations of the test results were rather large, statistical analysis has been carried out to test:

1. whether the effect of specimen width was significant,
2. whether the coefficients of variation of specimens with different widths at any given value of ϕ are significantly different.

These are done in the next two sections.

4.1.2. Significance of Width Difference

We assume that the test errors are normally distributed. Since all the samples were tested on the MTS machine using the same settings, we also assume the testing population variances are the same, but unknown.

We then compare the test results, the mean values, between different specimen widths to verify if the differences between the results were due to the change of specimen width or were purely due to random errors. The comparison was done using the t test [47]. We set 95% confidence level, which means that the result is probably not due to random errors. The results are shown in table 4.1 to table 4.4.

Table 4.1. Significance tests of modulus

Lay-up angles / Comparisons	0	15	30	45	60	75	90
ASTM-25mm	-	Y	Y	Y	Y	-	-
ASTM-43mm	-	Y	Y	Y	Y	-	-
ASTM-100mm	-	Y	Y	Y	Y	-	-
25mm-43mm	N	N	N	Y	Y	N	N
25mm-100mm	-	Y	N	Y	Y	Y	N
43mm-100mm	-	Y	N	N	N	Y	N

Note: Y means the difference is statistically significant; N means the difference is not statistically significant at the 95% confidence level.

Table 4.2. Significance tests of apparent Poisson's ratio

Lay-up angles / Comparisons	0	15	30	45	60	75	90
ASTM-25mm	-	Y	Y	N	N	-	-
ASTM-43mm	-	Y	Y	Y	Y	-	-
ASTM-100mm	-	Y	Y	N	N	-	-
25mm-43mm	N	N	Y	Y	N	Y	Y
25mm-100mm	Y	Y	Y	Y	N	Y	N
43mm-100mm	Y	Y	Y	N	N	Y	Y

Table 4.3. Significance tests of strength

Lay-up angles / Couples	0	15	30	45	60	75	90
ASTM-25mm	-	Y	Y	Y	Y	-	-
ASTM-43mm	-	Y	Y	Y	Y	-	-
25mm-43mm	Y	Y	Y	Y	N	N	Y

Table 4.4. Significance tests of failure strain

Lay-up angles / Couples	0	15	30	45	60	75	90
ASTM-25mm	-	Y	Y	Y	Y	-	-
ASTM-43mm	-	Y	Y	Y	Y	-	-
25mm-43mm	Y	Y	N	Y	N	Y	Y

The results in tables 4.1 to 4.4 confirm that the differences in the test results between the ASTM samples and the short wide samples were due to the change of specimen width and length. The differences among the short wide samples were not all significant.

4.1.3. Uniformity of the Test Results

Again we assume the test errors are normally distributed. We use the F test [47] to compare the uniformity between the test results to see if the test results from one specimen width are more variable than other results from other specimen widths at a given ϕ. With the 95% confidence level, there were no significant differences. Thus the qualities of the test results are all the same.

4.1.4. Possible Sources of the Variances

The variances could have come from fiber misalignment during the hand lay-up process. This included prepreg cutting, and the prepreg lay-up into the mould. Since these were done manually, errors could be introduced into the fiber alignments. Misalignment could have come from the curing process as well. Since the resin flowed in the mould and this might have changed the lay-up angles. Misalignment could also have come from cutting the samples from the molded sheet. However, it is considered that the misalignment caused by all the above was no more than 3 degrees.

The variation could have come from the mechanical testing process. The sample alignment between the MTS clamps was adjusted manually. The alignment relies heavily on the experience of the tester and may vary a small amount among the samples. This could have affected the short specimens more than the long specimens. The strain was recorded by a two-pen recorder. The recorder transferred the analog signals from the strain gauge boxes to the distances that the pens moved. This is not thought to introduce any significant error because the system was checked using aluminum, which has a known Young's modulus and Poisson's ratio and these are close to the values measured in these test.

The variations in apparent Poisson's ratios were very big. This was probably caused by the cracking which happened during the tests, especially for the longitudinal tests of the 25 mm specimens. Strains in the y direction were strongly affected by the cracking. The 100 mm specimens also had big variations. This was probably due to the special grip used. Here there could be variations in how well the screws were tightened, even although a torque wrench was used for this.

The wider samples generated smaller strength variations than the narrow ones when the fiber failure was the dominant failure mode, i.e. when the ϕ smaller than 45^0. For ϕ bigger than 45^0, the wider specimen gave the greater strength variations. This could have been because the failure was more fiber matrix interface dependant and more depended on the matrix itself. Here bigger volume and more interfaces were involved

with wider samples. The higher variation with the 43 mm specimens at 30^0 was because some of the specimens were broken in the end tabs.

4.2. Elastic Constants

4.2.1 Stress-Strain Relationships in Tension

The stress-strain relationships in the y direction of the angle ply laminates were not linear when the ply angles were less than 45^0. In $[0]_8$ laminate the y strain responses were not steady as shown in Figure 3.1.

Cracking sounds were heard during the test of 25mm width $[0]_8$ specimens. These sounds were also heard when 43mm specimens, with lay up angles from 0^0 to 30^0, were tested. Sudden changes in the y strains were observed accompanying the sounds. In Figure 4.5 the x and the y strains are shown when the first sudden changes in y strains happened.

Although the scatter made the trend less significant here, the narrow specimens normally gave higher first cracking strains. This indicated that Poisson's stress generated by the grips was less when the specimens' widths were reduced.

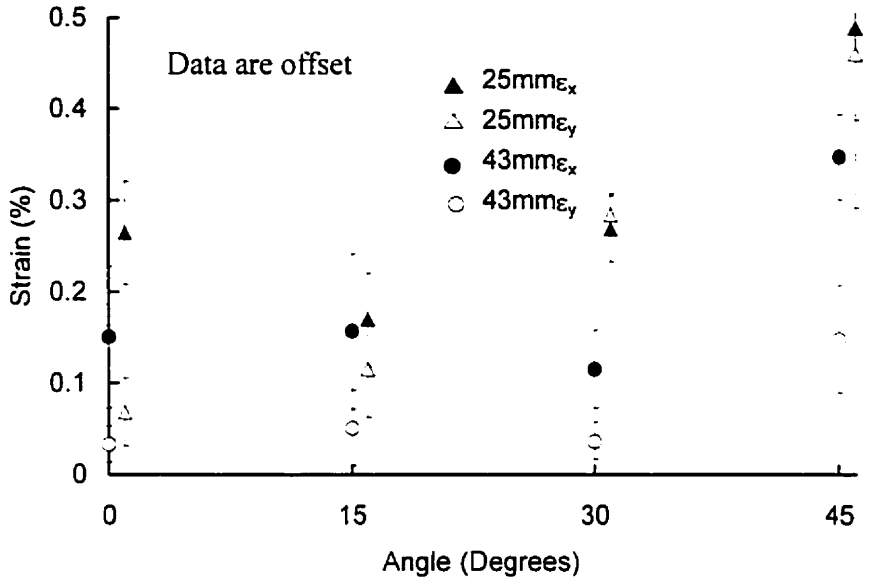

Figure 4.5. Strains when the cracking happened

Due to the very short gauge lengths used in the specimen, the end constraints prevented Poisson's shrinkage, which caused Poisson's stress in the y direction. When the ε_y approached the ultimate strains in the y direction, cracking would be initiated and developed. When the cracking happened, the strains in the y direction became unsteady.

The strain gauge was bonded in the middle of the specimen. The cracking would be initiated anywhere in the gauge area along the fiber directions. Thus the strain gauge would have different responses according to where the cracking happened. The y strains could escalate if the cracking began under the gauge. The y strain could also drop down temporarily if the cracking happened outside the areas which were not covered by the gauge, because the stress in the y direction could be released by the cracking occurring at that time.

The cracking was initiated along the fiber direction as shown in Figure 4.6. The cracks along the zero degree lay-up did not affect the modulus value too much for the $[0]_8$ because they were localized along the x direction. For the rest of the lay-ups, the specimens softened since the cracks went across the x direction. This was indicated by the two slope stress strain curves in the test of the specimens when $\phi \leq 45^0$. On the other hand, the $[0]_8$ had a linear stress strain curve up to finial failure.

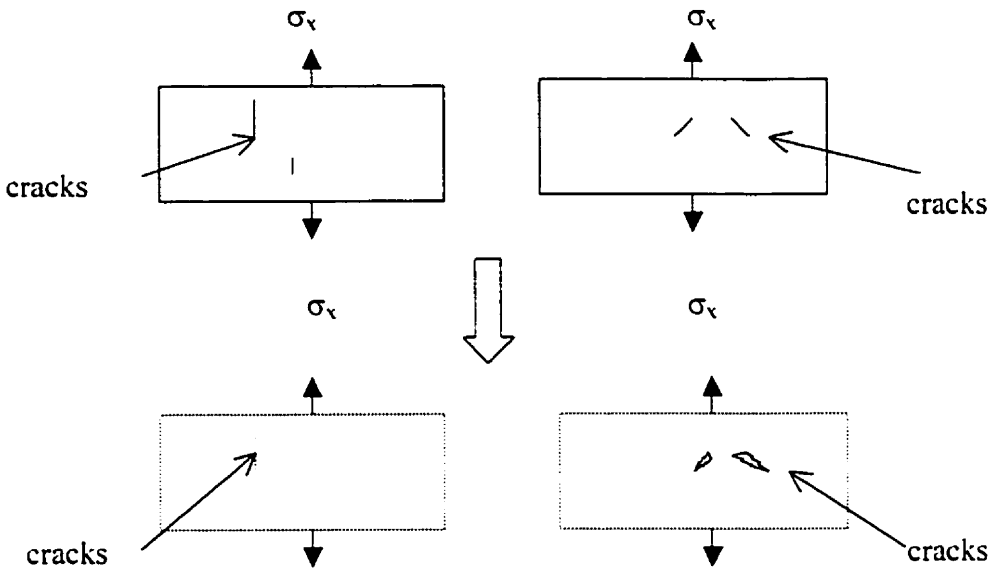

$[0]_8$ $[\pm\phi]_{2s}$

Figure 4.6. Cracks developed along the fiber directions

4.2.2 The Stress-Strain Relationship in Compression of $[\pm 15]_{6s}$ Laminate

The compressive specimen had a similar aspect ratio, gauge length over width, as the 43 mm specimens in tension. The compression sample did not produce very linear

stress strain curves; Figure 3.8. Moreover, the three strain gauges gave somewhat different readings, while strain gauge 1, 2, and 3, 4, were fairly close, strain gauges 5, 6 were significantly different from the rest. This is probably because of uneven loading. Using a Teflon film only helped a little, the stress strain curves were very similar and the right hand side strain gave about the same differences as that without the Teflon film. There was slightly increase in Poisson' ratio, from 0.56±0.13 to 0.76±0.10, but this was probably not significant. There was almost no change in the Young modulus, from 110±7 to 116±9 GPa. The stiffness was a little lower than the tensile value, which was 141±20 GPa, and the Poisson's ratio was higher than the tensile value, i.e. 0.33±0.13. Again the results were barely significantly different. Thus the compressive results were roughly in agreement with the tensile, but uneven loading reduced the precision.

4.2.3 The Stiffness of the Angle Ply Laminates

Since the stress-strain relationships showed inelasticity in the x direction for most of the lay-up angles, the initial slopes from the origin to the first kink or first noticeable curvature were used to calculate the stiffness. These stiffnesses are shown in Figure 4.7 and Tables A2 to A5 in the Appendix. In the figure the theoretical curves of E_x, $\bar{Q}_{11}$, and $\frac{1}{\bar{S}_{11}}$ are also shown. These stiffnesses are calculated based on the classical lamination theory. We input E_1=151 GPa, which is our test result from the 25 mm $[0]_8$ specimen. This value is very close to the value provided by Hexcel, 143±9 GPa. We input E_2=10.7 GPa, which is the test result from the 25 mm $[90]_8$ specimen. We use 25 mm $[\pm 45]_{2s}$

specimens' tensile result to calculate the G_{12} using $G_{12} = \frac{E_x}{2(1+\nu_{xy})}$. This comes to 5.3GPa. This value is very close to G_{12} values obtained with carbon epoxy tubes [34] and by Iosipescu method [48]. We assume ν_{12} is 0.27 which is a most widely used carbon/epoxy composite Poisson's ratio value [4].

The stiffness results showed that the wider specimen was stiffer than the narrow one. The only exception was the $[\pm 15]_{2s}$ in which the 100 mm sample appears to be giving a lower result. This was probably due to the non-uniformity of stressing. The fixture holding the specimen was probably not stiff enough to fully load the outer edges of the sample. Thus most of the loading flowed through the center as shown in the photoelastic image in Figure A11 in the Appendix. The more massive grip assembly could perhaps have solved this problem, but unfortunately allowed excessive slippage. Further work on better gripping systems for wider test specimens is recommended.

The end constraints provided by the grips seem to be not fully effective. Perfect restraint would give moduli on the upper curve in Figure 4.7, marked $\bar{Q}_{11}$. The lower curve, labeled E_x, gives the moduli where there is no end constraint. The measured results from short and wide specimens are close to the E_x. The ASTM specimens gave the results significantly lower than the E_x but above the $\frac{1}{\bar{S}_{11}}$, which should be the Young's moduli of lamina under off axis loading.

If we followed the ASTM standard D3039, in which it is suggested to use the strain range of 25% to 50% of the laminates ultimate strain, we obtained the stiffness shown in Figure 4.8 and Tables A6 to A8 in the Appendix. The theoretical data of $\bar{Q}_{11}$, E_x, and $\frac{1}{S_{11}}$ are also shown in the figure, based on the same data as those used for in Figure 4.7. The laminate moduli are all underestimated in Figure 4.8 because of the bi-modal nature of the stress-strain curves. The evidence shows that the ASTM standard recommendation appears not to work very well for the elastic property measurements. Following the standard would yield somewhat low values for the moduli for angle ply laminates.

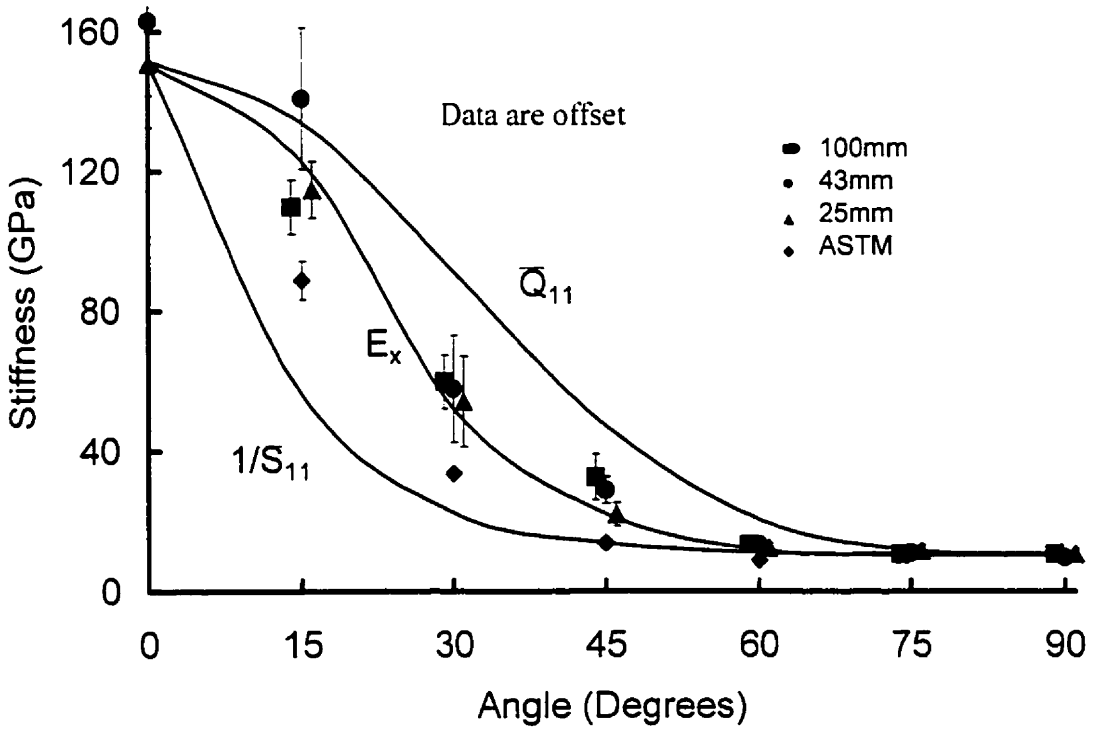

Figure 4.7. Stiffness using initial slopes

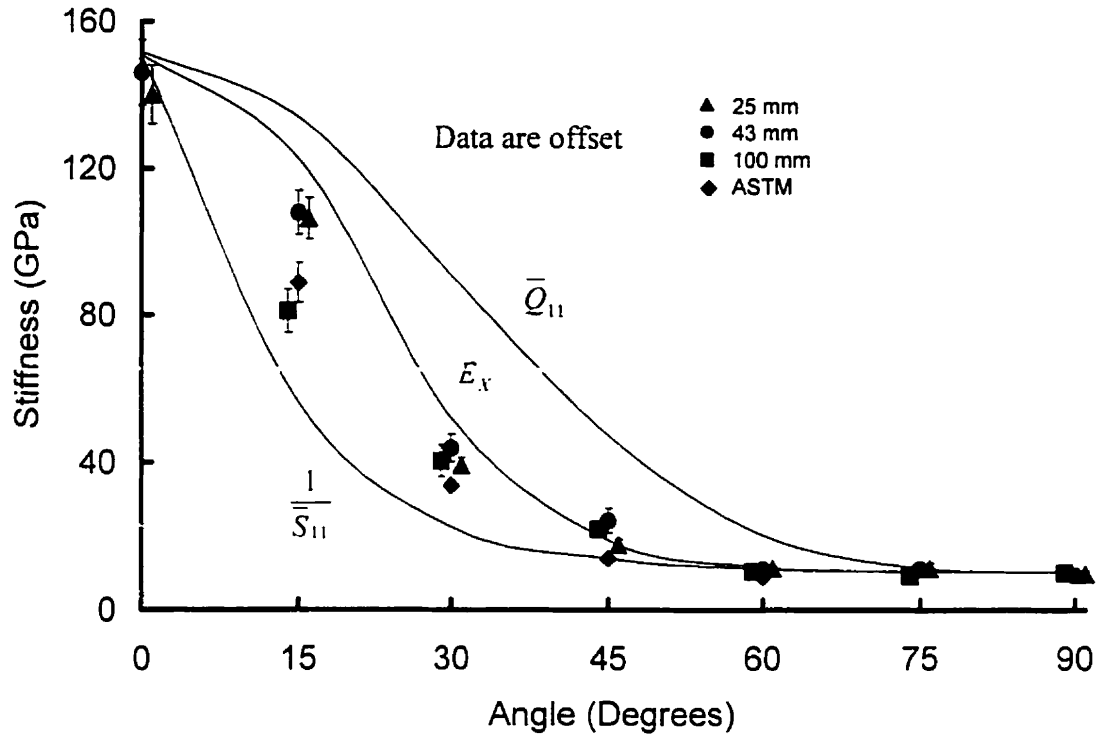

Figure 4.8. Stiffness using ASTM D3039 criterion

4.2.4. Modeling of Stiffness for ASTM Specimen

We model the ASTM specimens' stiffness using an empirical approach. According to the loading conditions we can divide the ASTM specimen into two regions, as shown in Figure 4.9a. Region I is the area where the fibers go into one of the clamps. Region II is the area where no fibers go into the clamps. Since Region II is expected to be much softer than the region I, we call region II the supersoft region. Because the strain gauge was bound in the middle of the sample, the test is measuring the Young's modulus and Poisson's ratio of the supersoft region.

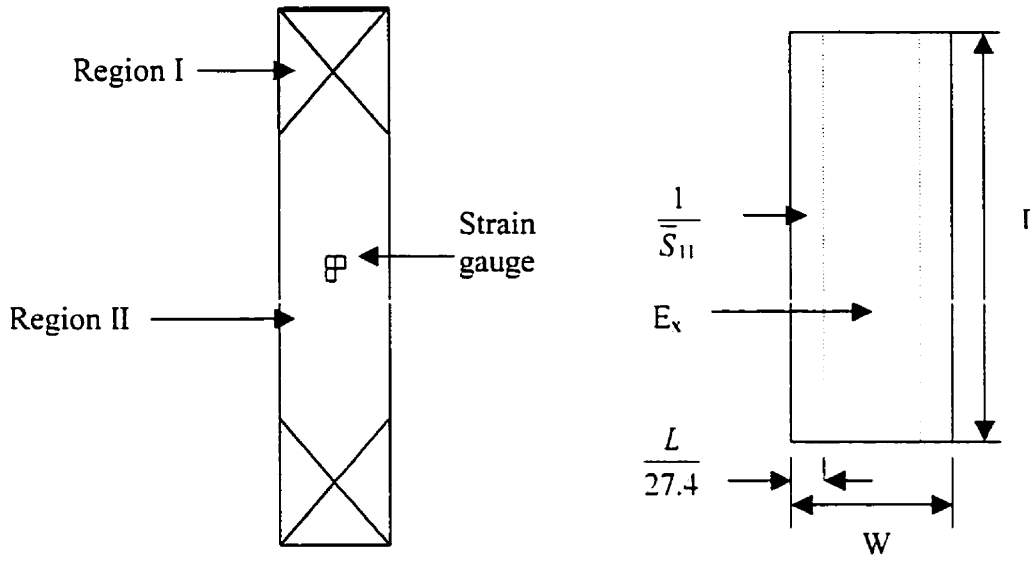

Figure 4.9. ASTM specimen

We use Tsai's early results to model the ASTM sample assuming that the modulus he measured was actually $\frac{1}{S_{11}}$ (see Figure 1.13: which shows that it was $\frac{1}{S_{11}}$ within the experimental error). Suppose that we can divide the ASTM specimen into edge regions with modulus $\frac{1}{S_{11}}$, and center region with modulus E_x as shown in Figure 4.9b. Further suppose that the specimen aspect ratio of the two edge regions added together is equal to Tsai's specimen aspect ratio. which is 13.7. Thus the width of each region is $L/27.4$ as shown in Figure 4.9.

The empirical equation for ASTM specimen stiffness is then:

$$E_{ASTM} = \left(\frac{L}{13.7W}\right)\frac{1}{\bar{S}_{11}} + \left(1 - \frac{L}{13.7W}\right)E_x \qquad (4.1)$$

Figure 4.10 shows the comparison of theoretical results from the equation 4.1 and the test results. The equation fits the test data quite well.

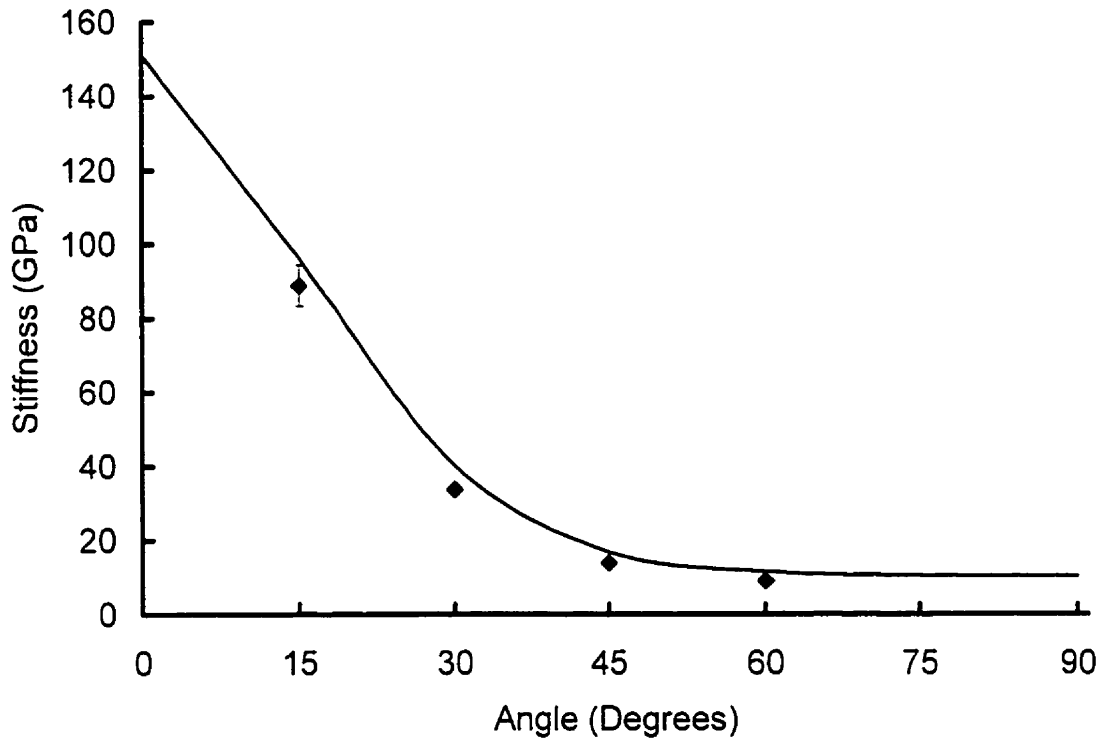

Figure 4.10. Comparison of equation 4.1 with test results

4.2.5. Modeling of Stiffness for Short Wide Specimen

The edge softening effect probably arises from the load not being directly applied to the fibers emerging from the specimen edges, as shown in Figure 4.11. This effect is assumed to account for the reduction of both laminates stiffness and strength. The edge

softening effect is different from the edge effect that causes edge delamination. Figure 4.11 divides the specimen into three regions according to the fiber loading conditions. These regions are:

- Supersoft region (II): no fibers go into the grips
- Soft region (III): the fibers go into one of the grips
- Stiff region (IV): the fibers go across the grips

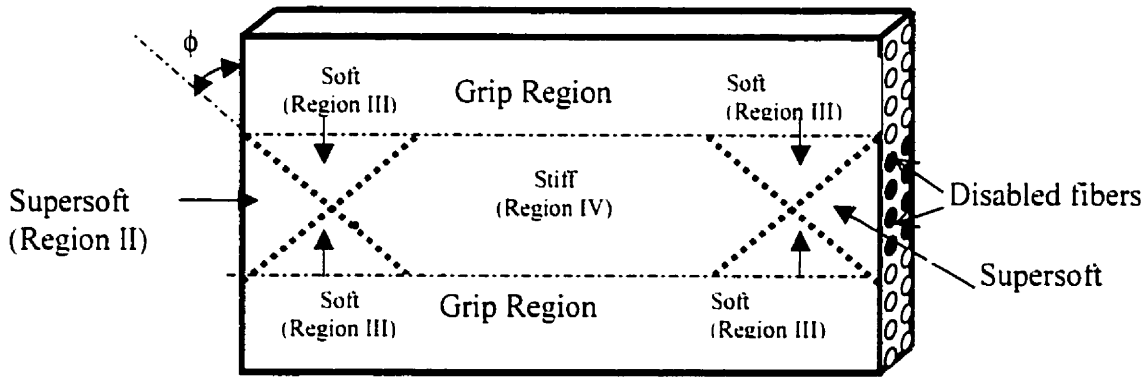

Figure 4.11. Test sample divided into three regions and grip region.

The different loading conditions for the fiber in the angle ply laminates can be simplified as shown in Figure 4.12 which is meant to represent the case for all widths and angles. The black color represents fiber and the clear part represents matrix. In Region II, we assume the possible stiffness value is the same as the value expressed by equation 4.1. In Region VI, we use the upper bound of the stiffness is $\overline{Q}_{11}$, which assumes $\varepsilon_y = 0$. In Region III when the angle is small, the fibers go a long way into grips, giving greater

stiffness, while when the angle is large, the fibers go into the edge sooner, giving smaller stiffness. For this region we use E_u, where $E_{ASTM} < E_u < \bar{Q}_{11}$.

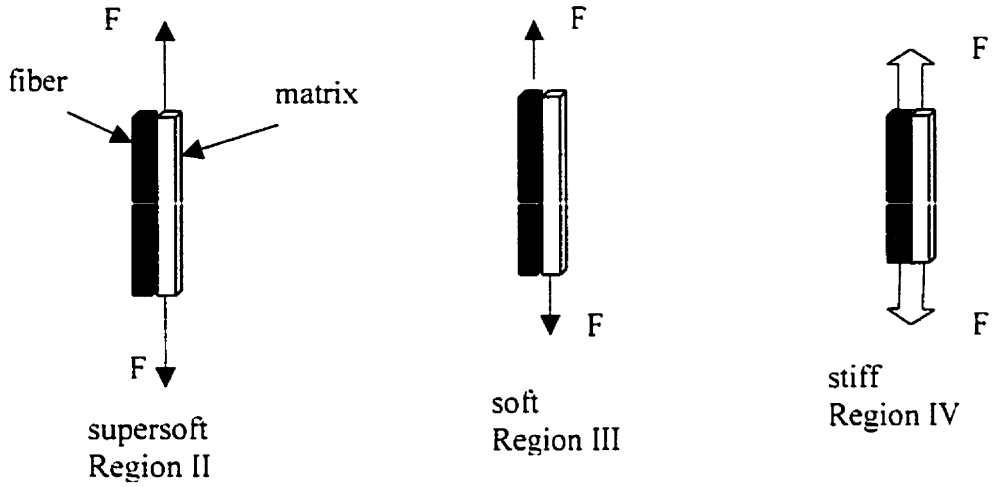

Figure 4.13. Simplified loading situation of different regions

Since the specimen shown in Figure 4.12 is symmetric, we only take the top half edge region to model the stiffness of the edge regions; see Figure 4.14. This is, for convenience of calculation, divided in two parts, one which has modulus E(1) and the other having E(2)

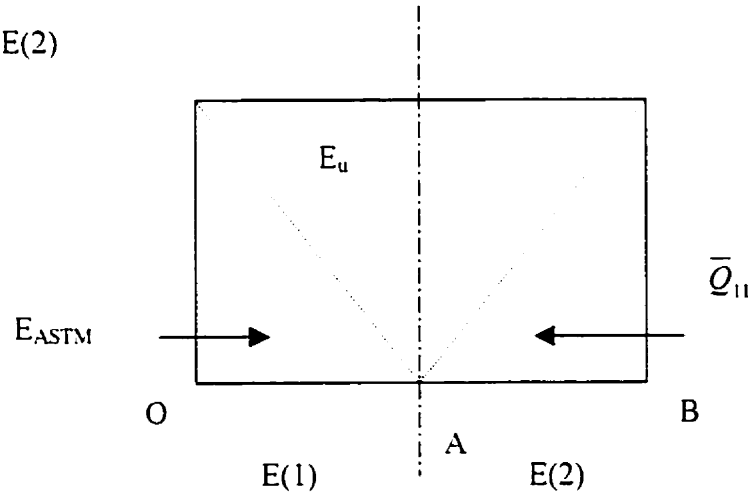

4.14. One half of the edge region of a short wide sample

Let us estimate E(1) first. The area is shown in Figure 4.15. The load is applied along the x direction. We divide the specimen into strips with width dy.

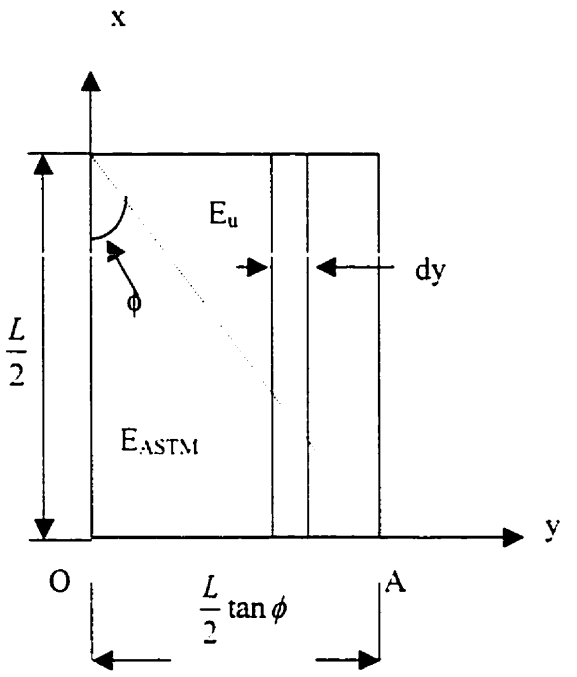

Figure 4.15. The E(1) area

To estimate E(y), the modulus of the strip, we use a series model, apply a stress σ_x and add the displacements to get the total displacement as:

$$\frac{L\sigma_x}{2E(y)} = \left(\frac{L}{2} - x\right)\frac{\sigma_x}{E_u} + x\frac{\sigma_x}{E_{ASTM}} \tag{4.2}$$

thus

$$\frac{1}{E(y)} = \frac{\left(1 - \frac{2x}{L}\right)}{E_u} + \frac{2x}{LE_{ASTM}} \tag{4.3}$$

but since

$$x = \frac{L}{2} - y\cot\phi \tag{4.4}$$

Using equation 4.4. equation 4.3 becomes

$$E(y) = \left[\left(\frac{2y}{LE_u \tan\phi} + \left(1 - \frac{2y}{L\tan\phi}\right)\frac{1}{E_{ASTM}}\right)\right]^{-1}$$

(4.5)

To estimate E(1) we use the parallel model. which means we sum the moduli for each element of dy. i.e. we integrate E(y) with respect to y

$$E(1) = \frac{2}{L\tan\phi}\int_0^{\frac{L}{2}\tan\phi}\left[\frac{2y}{LE_u\tan\phi} + \left(1 - \frac{2y}{L\tan\phi}\right)\frac{1}{E_{ASTM}}\right]^{-1} dy \tag{4.6}$$

Equation 4.6 has the form

$$E_{(1)} = \int_0^{x_m}\frac{dx}{a+bx} = \frac{1}{b}\left[\ln(a+bx)\right]_0^{x_m} \tag{4.7}$$

where

$$a = \frac{1}{E_{ASTM}}, \quad b = \frac{2}{L\tan\phi}\left(\frac{1}{E_u} - \frac{1}{E_{ASTM}}\right) \tag{4.8}$$

Integrating equation 4.6, using the limits, and re-arranging the resulting equation, we have

$$E(1) = \frac{\ln(E_u \ E_{ASTM})}{E_A^{-1} - E_u^{-1}} \tag{4.9}$$

We can derive E(2) in a similar way. Figure 4.15 shows the E(2) area.

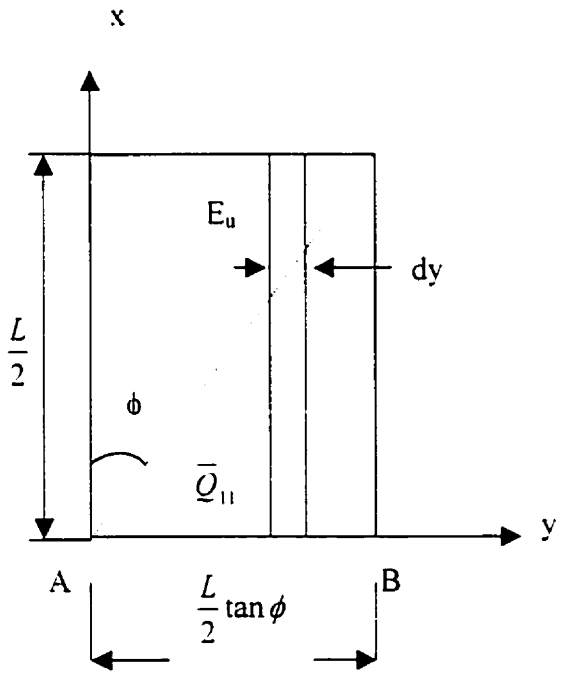

Figure 4.15. The E(2) area

As before we add the deformations to obtain:

$$\frac{L\sigma_x}{2E(y)} = \left(\frac{L}{2} - x\right)\frac{\sigma_x}{E_u} + x\frac{\sigma_x}{\bar{Q}_{11}} \tag{4.10}$$

Since

$$\tan\phi = \frac{y}{x} \tag{4.11}$$

we can rearrange the equation 4.10, this gives

$$E(y) = \left[\left(1 - \frac{2y}{L\tan\phi}\right)\frac{1}{E_u} + \left(\frac{2y}{L\tan\phi\bar{Q}_{11}}\right)\right]^{-1} \tag{4.12}$$

Again using the parallel model, we estimate E(2) by integrating these E(y) as:

$$E(2) = \frac{2}{L\tan\phi}\int_0^{\frac{L\tan\phi}{2}}\left[\left(1 - \frac{2y}{L\tan\phi}\right)\frac{1}{E_u} + \left(\frac{2y}{L\tan\phi\bar{Q}_{11}}\right)\right]^{-1} dy \tag{4.13}$$

Equation 4.13 also has the form of Equation 4.7. We integrate equation 4.13, using the limits, and rearranging the resulting equation, this gives

$$E(2) = \frac{\ln\left(E_u\ \bar{Q}_{11}\right)}{\bar{Q}_{11}^{-1} - E_u^{-1}} \tag{4.14}$$

The stiffness of the edge region shown in Figure 4.13 is the combination of E(1) and E(2) in parallel. Since the areas of E(1) and E(2) are the same, the modulus of the edge region, E_{edge}, is simply the mean of E(1) and E(2), i.e.

$$E_{edge} = \frac{1}{2}\left[\frac{\ln E_u - \ln E_{ASTM}}{E_{ASTM}^{-1} - E_u^{-1}} + \frac{\ln E_u - \ln \bar{Q}_{11}}{\bar{Q}_{11}^{-1} - E_u^{-1}}\right] \tag{4.15}$$

The stiffness of the short wide specimen is the combination of two edges and the center part with stiffness $\bar{Q}_{11}$. Let ϕ_c be the critical angle above which no fiber goes across the clamps. Thus $\phi_c = \arctan(W/L)$. Adding the stiffness in proportion to the widths involved gives, for the case where $\phi \le \phi_c$:

$$E_x = \frac{2L\tan\phi}{W} E_{edge} + \left(1 - \frac{2L\tan\phi}{W}\right)\bar{Q}_{11} \tag{4.16}$$

Substitute the equation 4.15 into Equation 4.16, and let $s = L/W$, where s is the sample aspect ratio. This gives the short wide specimen effective modulus:

$$E_x = s\tan\phi\left[\frac{\ln E_u - \ln E_{ASTM}}{E_{ASTM}^{-1} - E_u^{-1}} + \frac{\ln E_u - \ln \bar{Q}_{11}}{\bar{Q}_{11}^{-1} - E_u^{-1}}\right] + (1 - 2s\tan\phi)\bar{Q}_{11} \tag{4.17}$$

When $\phi > \phi_c$, there is no stiff region, region IV, in the specimen. Although, there are different combinations of the region II and region III, in this case it is adequate to use the E_{edge}, equation 4.15, to describe the specimen modulus since the differences among the $\bar{Q}_{11}, E_x, and \frac{1}{\bar{S}_{11}}$ are very small at the angle $\phi > \phi_c$. Thus for $\phi > \phi_c$

$$E_x \approx \frac{1}{2}\left[\frac{\ln E_u + \ln \bar{S}_{11}}{\bar{S}_{11} - E_u^{-1}} + \frac{\ln E_u - \ln \bar{Q}_{11}}{\bar{Q}_{11}^{-1} - E_u^{-1}}\right] \tag{4.18}$$

Because E_u must be somewhere between the modulus of region III and that of region IV, we will assume it is the mean value, i.e.

$$E_u = \frac{1}{2}(\bar{Q}_{11} + E_{ASTM}) \tag{4.19}$$

Using equations 4.1, 4.17, 4.18, and 4.19, we can calculate short wide specimen stiffness and compare the theoretical results with the test data. The comparison is shown in Figure 4.16. The model fits the test data moderately well.

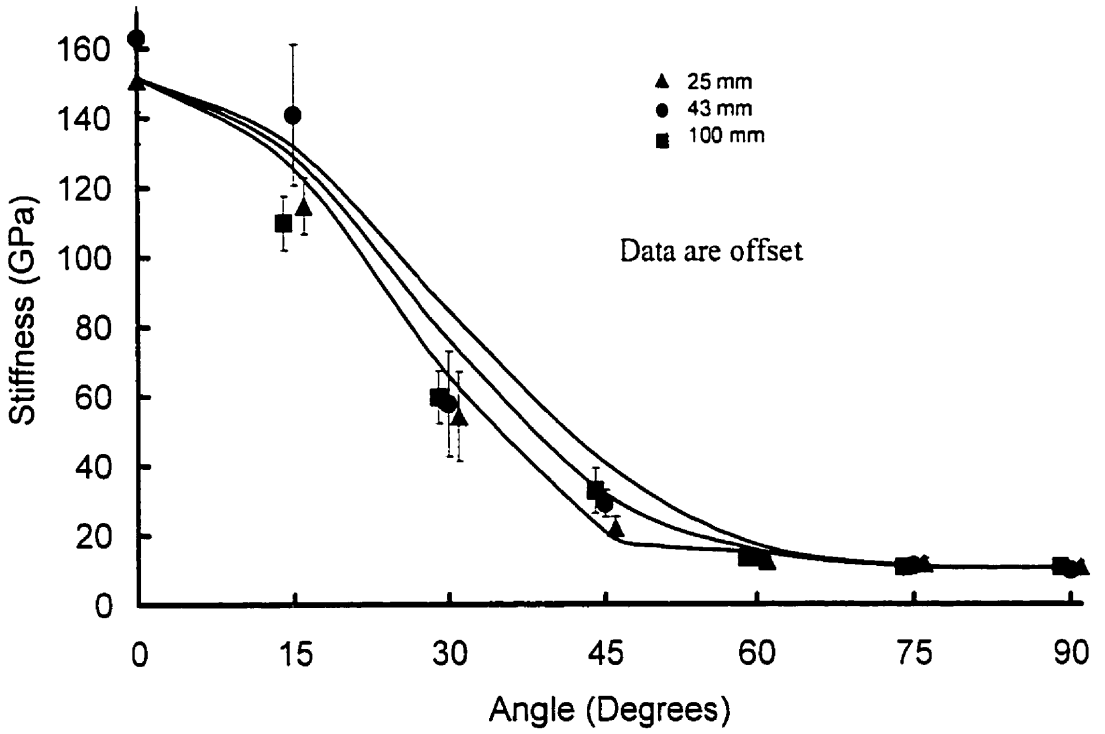

Figure 4.16. Comparison of equation 4.17 with test results (Supersoft: E_{ASTM})

Furthermore if we assume the supersoft region has the modulus of $\frac{1}{\bar{S}_{11}}$ instead of E_{ASTM}, we use $\frac{1}{\bar{S}_{11}}$ in the equation 4.17 and 4.19. This also gives a moderately good fit for the experimental data as shown in Figure 4.17.

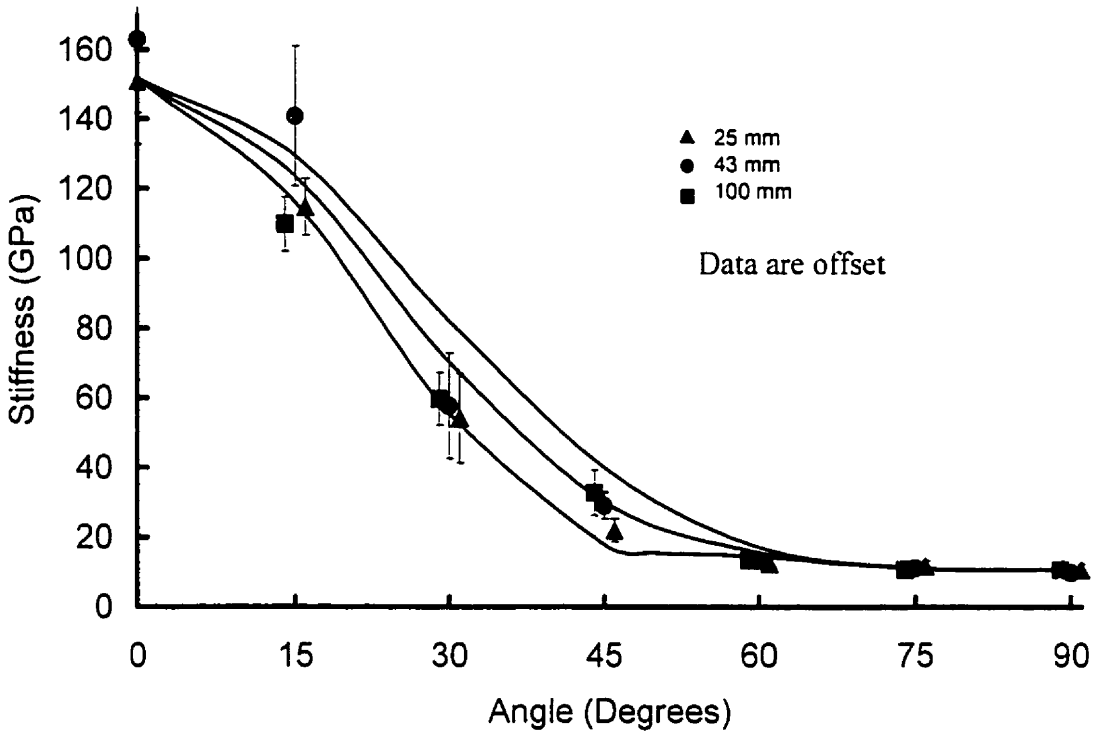

Figure 4.17. Comparison of equation 4.17 with test results (Supersoft: $1/\bar{S}_{11}$)

4.2.6 The Principal Poisson's Ratio

Since the $\sigma_Y \neq 0$ due to the Poisson's stress, the Poisson's ratios measured from the short wide specimen were not Poisson's ratio but apparent Poisson's ratio. The

principal apparent Poisson's ratios estimated from the initial slopes are shown in Figure 4.18, which is from the initial slopes. In Figure 4.19, the apparent Poisson's ratios were calculated according to the ASTM 3039 criterion. The theoretical Poisson's ratios, calculated from classical laminate theory based on the properties used in Figure 4.7, are shown by the curves in the figures.

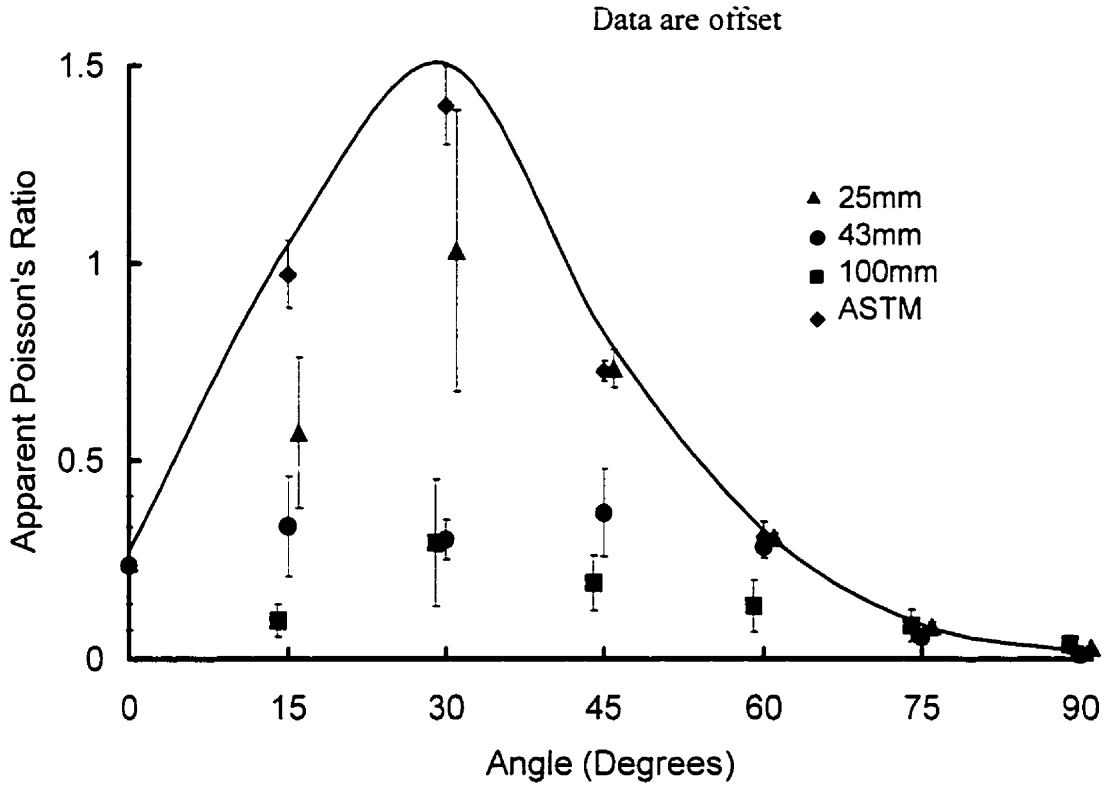

Figure 4.18. Apparent Poisson's ratios using initial slopes

The grips did constrain the specimens as shown by the low values of the apparent Poisson's ratios in Figures 4.18 and 4.19. The narrow specimen always gave the highest apparent Poisson's ratios and the widest specimen gave the smallest values. The measured Poisson's ratios of the ASTM samples are very close to the theoretical values but the rest are much less than the theoretical ones when the lay-up angles are less than thirty degrees. When the lay-up angles increased, the 25mm sample approached the

theoretical value at forty-five degrees, and all the samples agreed with the theoretical values at seventy-five and ninety degrees.

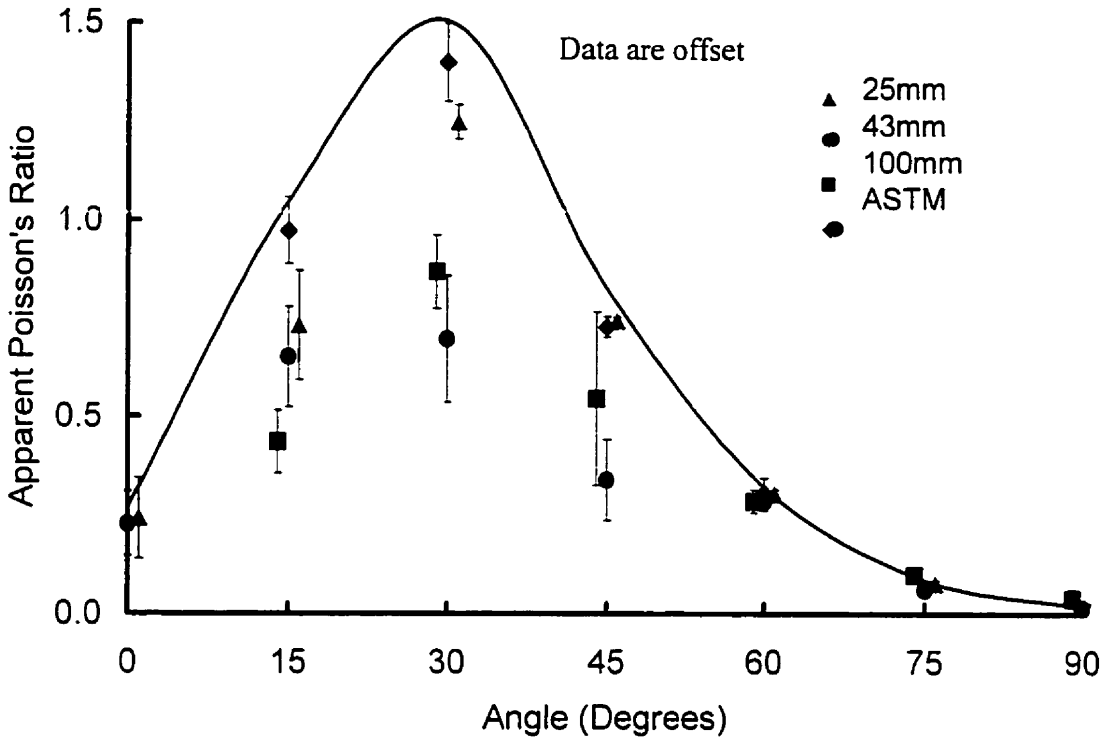

Figure 4.19. Apparent Poisson's Ratios using ASTM D3039 criterion

By using the higher strain of 25% to 50% to calculate the apparent Poisson's ratio, as suggested by the ASTM standard, we got higher results (see Figure 4.19). The 25mm and the 43mm samples had a similar trend to those in Figure 4.18 but the 100mm samples were not always the lowest values. This was probably due to the different clamping conditions between the 100mm specimens and the 25mm and 43mm ones.

4.3. Yielding

We observed non-elastic deformation both in the stress strain curves and in the photoelastic images for wide and short specimens in tension. This was probably due to the cracks developed in the specimens as discussed before. These cracks were caused by the Poisson's stress. The upper and lower bound for Poisson's stress in a tensile test are $\varepsilon_y = 0$ (upper), and $\sigma_y = 0$ (lower), which could ideally be achieved with very big specimen aspect ratio and very small aspect ratio respectively. In practice with specimens having finite length, as with our 20mm gauge length specimens, we have $\sigma_y > 0$. We can thus estimate σ_y from the difference between the measured Poisson's ratios and the theoretical values from the lamination theory. Assuming, for simplicity, that the deformations along the specimen sides are uniform, the Poisson's stress σ_y can be expressed as:

$$\sigma_y = E_y (\nu_{th} - \nu_{exp}) \varepsilon_x \tag{4.20}$$

where ν_{th} and ν_{exp} are the theoretical Poisson's ratio and measured apparent Poisson's ratio respectively, thus

$$\frac{\sigma_y}{\sigma_x} = \frac{E_y}{E_x} (\nu_{th} - \nu_{exp}) \tag{4.21}$$

where σ_x is the applied stress.

Poisson's stresses for the 25 mm, 43 mm and 100 mm width specimens, estimated using equation 4.21, are shown in Figure 4.20. The curve in the figure shows the Poisson's stress when the specimens are totally constrained, i.e. equation 4.21 with $\nu_{exp}=0$.

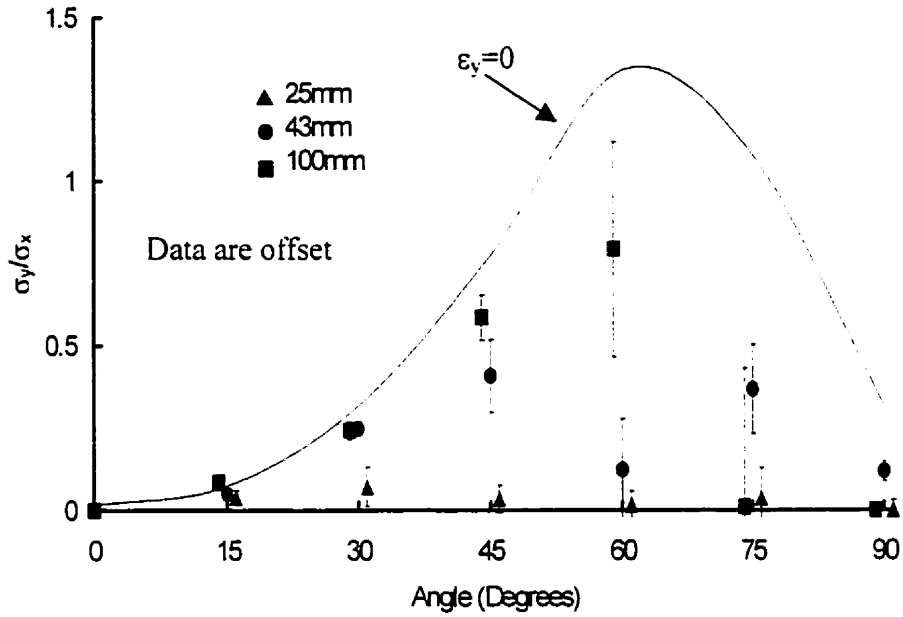

Figure 4.20. Poisson's stresses

As expected, the wider specimen generated higher Poisson's stress. The 100 mm specimen gave the highest Poisson's stress at 60^0, while the 43mm specimens had two peak values at 45^0 and 75^0. The 25 mm specimen had the peak value at about 30^0.

The photoelastic image, figures 3.19, 3.21, 3.22, and 3.23, indicated non uniformity of strain differences in the specimens during the loading. As long as the

difference between the maximum principal strains is constant, no fringes or other details appears. This can be seen in the pictures at low applied strains.

When the specimens were loaded beyond the elastic range, the colour patterns showed that non-uniform strains developed in the gauge area. The fiber presence was also apparent in the patterns. The higher strain differences appeared in the areas where the fibers were most highly stretched. These areas included fibers which went across the grips. The plastic deformation was confirmed in most cases, by the colour patterns remaining after the loads were released.

The comparison of the stresses in the stress strain curves when the first kink or sign of curvature happened and the stresses when the fiber presence was observed in the photoelastic image, both for the 43 mm specimens, are listed in the table 4.5. From the table, we can see the results correlated quite well remembering that the photos were taken at large stress intervals. Moreover the strain gauge results give the first indication of inelasticity while the photoelastic results indicating the yielding of the material.

Table 4.5. Comparison of stresses when non-elastic deformation happened

ϕ (Degrees)	Stress-strain curve (MPa)	Photoelastic image (MPa)
15	102±7	150
30	63±10	80
45	30±2	44

We observed different colour patterns in the compression of the $[\pm 15]_{6s}$ specimen. The strain distribution was not uniform in the plastic range (see Figure 3.23). This was probably due to non-uniform contacts between the platens and the specimen since by the results from strain gauges in the different position were different. The stress strain plot from the strain gauges were not linear (see Figure 3.8a). However, when re-stressed (Figure 3.8b) the stress strain plots followed the same path, indicating that any non-elastic effects were reversed on de-stressing. While the appearance of the fibers in the photoelastic patterns in tension may indicate some matrix plasticity around fibers, the absence of a similar pattern in compression suggests that the inelastic compressive process may be different.

We also observed yielding in ASTM $[\pm 45]_{2s}$ specimens (Figure 3.4). According to Rotem and Hashin [49], the 45^0 angle ply laminate has a unique failure mechanism and it exhibits ductile behavior. They back lighted their glass/epoxy specimen, 19 mm wide and 220 mm long, and observed initiation of yielding or inelasticity coincident with the appearance of a dark line following one of the fiber directions. The crack did not developed very much. Instead new cracks appeared criss-crossing the whole specimen. The number of the cracks increased with the elongation until interlaminar yielding started, which caused bundles of fibers to move and change orientation. They measured an angle change of 2^0 at failure. Other lay-ups, $[\pm 30]_{2s}$ and $[\pm 60]_{2s}$, did not do this. Instead only few dark lines appeared and extended locally, started on edges in the $[\pm 30]_s$ and in the specimen of $[\pm 60]_{2s}$, until one of them caused the specimen failed.

4.4 Strengths and Ultimate strains

4.4.1. Strength

The strengths of the angle ply laminates are shown in Figure 3.9. In Figure 4.21 the comparisons of the tested strengths with Khatzibadeh-Piggott (marked KP) and Tsai-Wu predictions, as listed in equations 1.1 and 1.45, are shown.

In the Tsai-Wu criterion (1.45) the σ_{1u} and σ_{2u} are 1.9 GPa and 0.06 GPa respectively, which are from our test results. The τ_{12u} is 0.06 GPa, which is from the $[\pm 45]_{2s}$ 25 mm sample test results, using $\tau_{12u} = \frac{\sigma_{\phi u}}{2}$. The compressive strength σ_{1cu} and σ_{2cu} are taken as σ_{1u} and $6\sigma_{2u}$ respectively. The experimental factor F_{12} is taken as 0.5. Two different loading regimes are applied to the Tsai-Wu criterion which give the limiting cases of:

1). $\sigma_y = 0$

2). $\varepsilon_y = 0$.

As can be seen in Figure 4.7, the Tsai-Wu criterion significantly underestimates the angle ply laminate strengths for $\phi=15^0$, 30^0, and 45^0, whichever loading case is used. With $\varepsilon_y=0$, the theoretical curve is further away from the experimental values. The Tsai-Wu criterion has been widely used in composite designs. This criterion only works well when no fiber is being fully stretched, as in the case of using narrow and long specimens such as in Tsai's early work [8]. Based on our test data, many composite structures used in the aircraft industry are over designed if the strength design criterion is used.

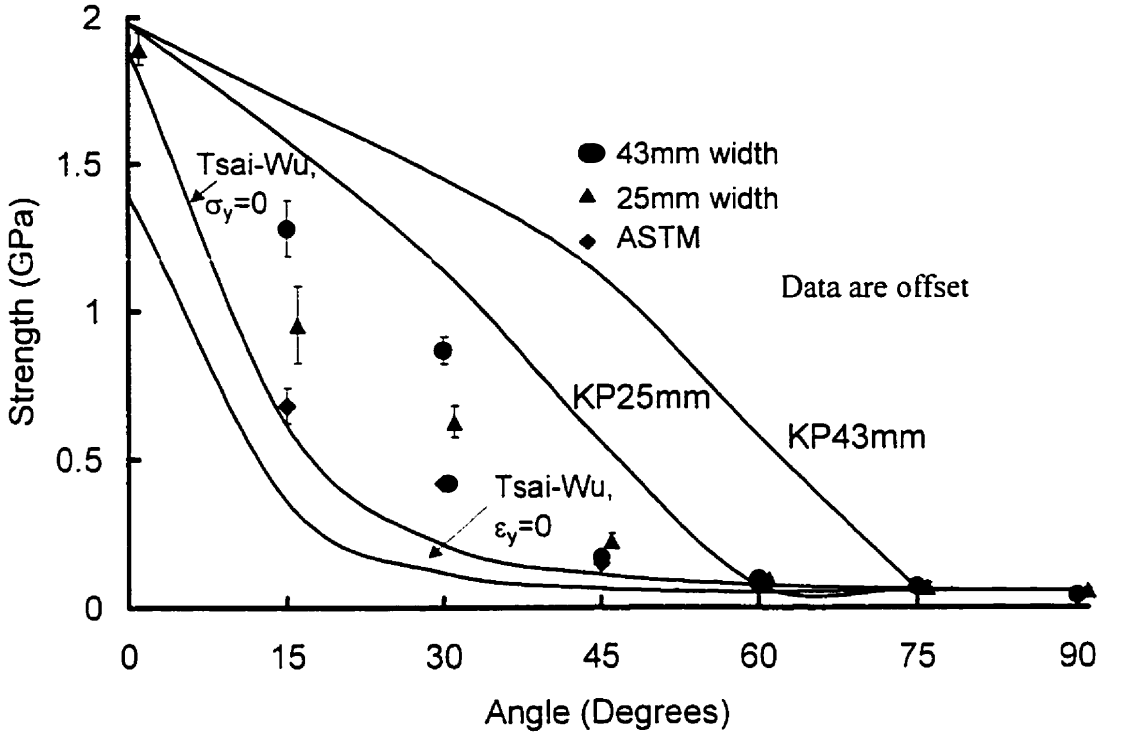

Figure 4.21. Failure criteria compared with test results

Based on same parameter used by Khatzibadeh [50], which is $\phi_0=48^0$, and $\sigma_{1u}=1.9$GPa, which is our test value, equation 1.1 tends to over-estimate the strength as shown in the figure, marked KP25mm and KP43mm. However, the ϕ_0 is an adjustable parameter which we can adjust as shown later in the modeling section.

4.4.2 Ultimate Strains

The angle ply ultimate strains of the laminates were shown in Figure 3.10 and are repeated here for convenience, in Figure 4.22.

The 25mm $[\pm 45]_{2s}$ specimen gave a very high failure strain of more than 6%. Rotem and Hashin [49] observed similar strains with glass epoxy $[\pm 45]_s$ angle ply laminates. They also observed that the laminate angle changed by about two degrees during the test. This is called the "scissors effect". It is due to the matrix not being stiff enough to hold the fibers firmly. The fibers rotated in a scissoring cutting.

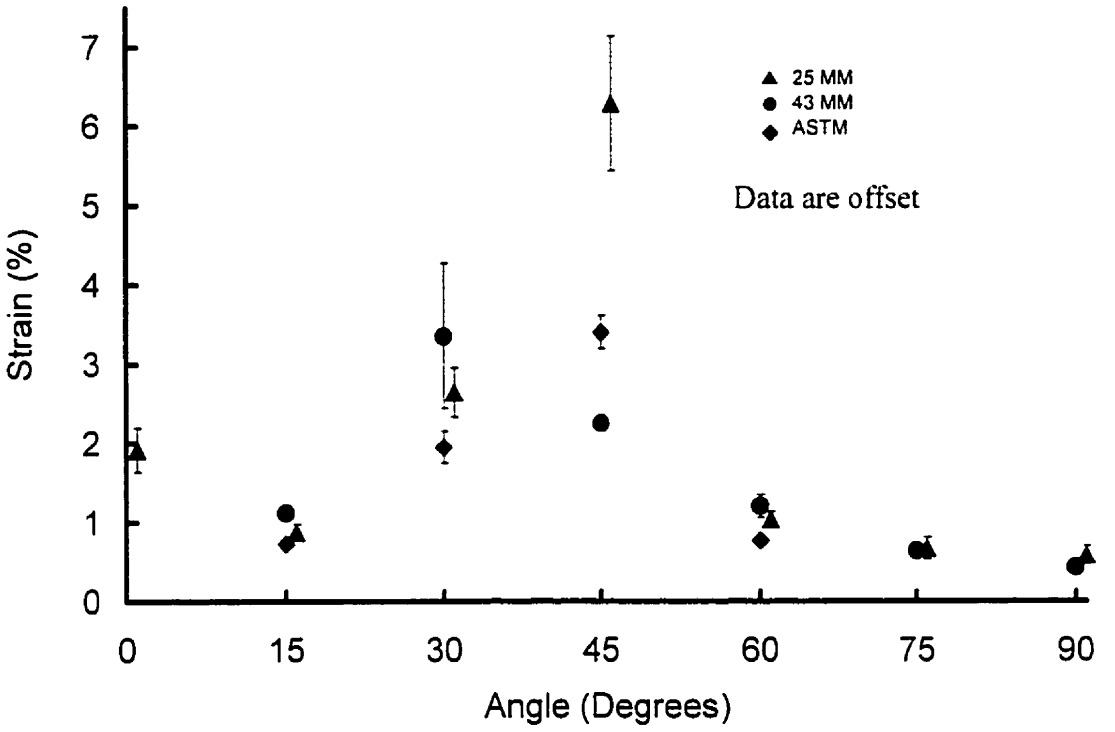

Figure 4.22. Ultimate strain of the angle ply laminate

At ϕ equals 15^0, 30^0, and 60^0 the wider specimen gave higher ultimate strains than the narrow ones, while at ϕ equals 75^0, and 90^0 the narrow specimen gave higher results. At ϕ equals 45^0, the 25 mm specimens generated the highest ultimate strain, the ASTM gave the second higher result, while the 43 mm specimen gave the lowest. This can be related to the failure mechanism of the laminates. When the angles were less than 60^0, but

not equals to 45^0, the edge effect probably initiated the failure. The wider the specimen, the less the effect was. This is different from the observations of Rotem and Hashin [49] in which the edge effect was important up to $\phi<40^0$ for their long and narrow specimen. When $\phi>60^0$, failure initialized from the center. They obtained a unique result at $\phi=45^0$, basically in agreement with our results for $[\pm45]_{2s}$ laminates. These involved a unique failure mechanism as discussed before; i.e. the gradual initiation of small cracks which did not develop. The yielding process they observed, if occurred here, does not depend on the specimen's width, since there is no width trend shown in Figure 4.22.

4.4.3. Modeling for Strength

We model the angle ply laminate strength based on the edge softening. We assume that fibers contribute to the laminate strength fully when they are broken. If the fibers are not broken, they do not make any contribution.

We model the short and wide specimen first. As shown in Figure 4.23, we assume that the initial fracture was generated at one of the corners, marked A, which was considered to be the weakest point. The fracture developed from the corner along the fiber direction to the point C where the three regions, stiff, soft, supersoft, joined. At that point the fracture further developed across the specimen to point D.

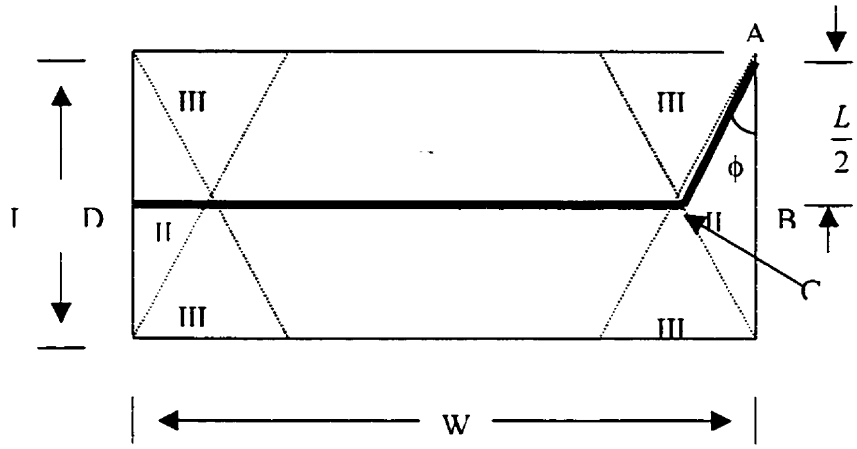

Figure 4.23. Fracture surface of short wide specimens

Table 4.6 lists the calculated half fiber broken lengths BC, using $BC = \frac{L}{2}\tan\phi$, (see Figure 4.23) compared with the measured half fiber broken lengths. From the table we can see that the calculated values are very close to the measured ones for ϕ=15^0 but not so good for ϕ=30^0. However, they are close enough that it seems reasonable to use this equation for BC.

Table 4.6. Calculated BC compared with measured ones

Laminate Angle (Degrees)	15	30
Calculated Length (mm)	5.4	11.5
Measured Length of 25mm Sample (mm)	5±1	8±1
Measured Length of 43mm Sample (mm)	5±1	8±1

The fracture along the fiber direction (AC) broke half of the fibers. The fracture across the specimen (BD) broke all of the fibers. This failure model is based on a brittle failure nature. From the fracture image shown in Figure 3.11 to 3.18 we can see it is true for the ϕ equals 15^0 and 30^0.

As suggested by Khatibzadeh and Piggott [20], composite strength can be estimated by using equation 1.1, which is reprinted here for convenience:

$$\sigma_{cu} = \sigma_{1\phi}\left(1 - \frac{\tan\phi}{\tan\phi_0}\right) + \tau_{cu}/\cos^2\phi\tan\phi_0 \qquad (4.22)$$

where ϕ_0 is an adjustable parameter that $\phi_0 \le \phi_c$. The first term is the strength of the stiff region while the second term is the strength of the supersoft region. They further proposed that

$$\sigma_{1\phi} = V_f\sigma_{fu\phi} + V_m\sigma_{mu} \qquad (4.23)$$

where V_f and V_m are fiber and resin volume fractions respectively. σ_{mu} is resin strength, and $\sigma_{fu\phi}$ is the strength of fibers crossing cracks obliquely at an angle ϕ and.

$$\sigma_{fu\phi} = \sigma_{fu0}f(\phi) \qquad (4.24)$$

where σ_{fu0} is the normal fiber strength.

Using a data fitting technique, they suggested that

$$f(\phi) = \frac{1}{2}\left[1 + \left(1 - \frac{\phi}{\phi_h}\right)^{\frac{1}{3}}\right] \qquad (4.25)$$

agreed with their experimental results well enough to be used to make approximate predictions. In equation 4.24, ϕ_h is the half strength angle at which $\sigma_{fu\phi} = \frac{1}{2}\sigma_{fu0}$. For

carbon fibers they found ϕ_h=40^0. Although they developed equation 4.23 to 4.25, they did not use them but to used that assuming $\sigma_{1\phi} = \sigma_{1u}$ was adequate to fit their test results.

We combine equations 4.22 to 4.25 and have composite strength as

$$\sigma_{\phi u} = \left(1 - \frac{\tan\phi}{\tan\phi_0}\right)\left\{\frac{1}{2}V_f\sigma_{fu0}\left[1 + \left(1 - \frac{\phi}{\phi_h}\right)^{\frac{1}{3}}\right] + V_m\sigma_{mu}\right\} + \tau_{cu}/\cos^2\phi\tan\phi_0 \quad (4.26)$$

The 45^0 lay-up is a special case since it exhibits ductile behavior. So we cannot use equation 4.26 to model the 45^0 lay up. When ϕ=45^0, we use the maximum strength criterion. $\sigma_{\phi u} = \frac{\sigma_{2u}}{\sin\phi\cos\phi}$ (1.42). Whenϕ>45^0, we use $\sigma_{\phi u} = \frac{\sigma_{2u}}{\sin^2\phi}$. The material properties needed for evaluation of the equations are listed in Table 4.7. The V_f, σ_{mu}, and σ_{fu0} were provided by Hexcel. The σ_{1u} and σ_{2u} are our test results from the 25 mm specimens. We use ϕ_h=45^0 for both sample widths and ϕ_0=45^0 and 35^0 for the 43 mm samples and 25 mm samples respectively. We use ϕ_h and ϕ_0 as adjustable parameters; this is because testing a laminate is probably different from testing single fibers. Figure 4.24 shows the results calculated from equations 4.26 and 1.42 compared with the test results. The equations fit the experimental data fairly well.

Table 4.7. Properties of the composite materials

V_f (%)	σ_{fu0} (GPa)	σ_{2u} (GPa)	σ_{mu} (GPa)
55	4.24	0.06	0.07

We next model the strength for the ASTM samples. Since half of the fibers were broken in all the $[\pm\phi]_{2s}$ ASTM specimens ($0^0<\phi<90^0$), we use equations 4.23 to 4.25, divided by two. Figure 4.25 shows the comparison of the equation with the test data. The model fits the data fairly well.

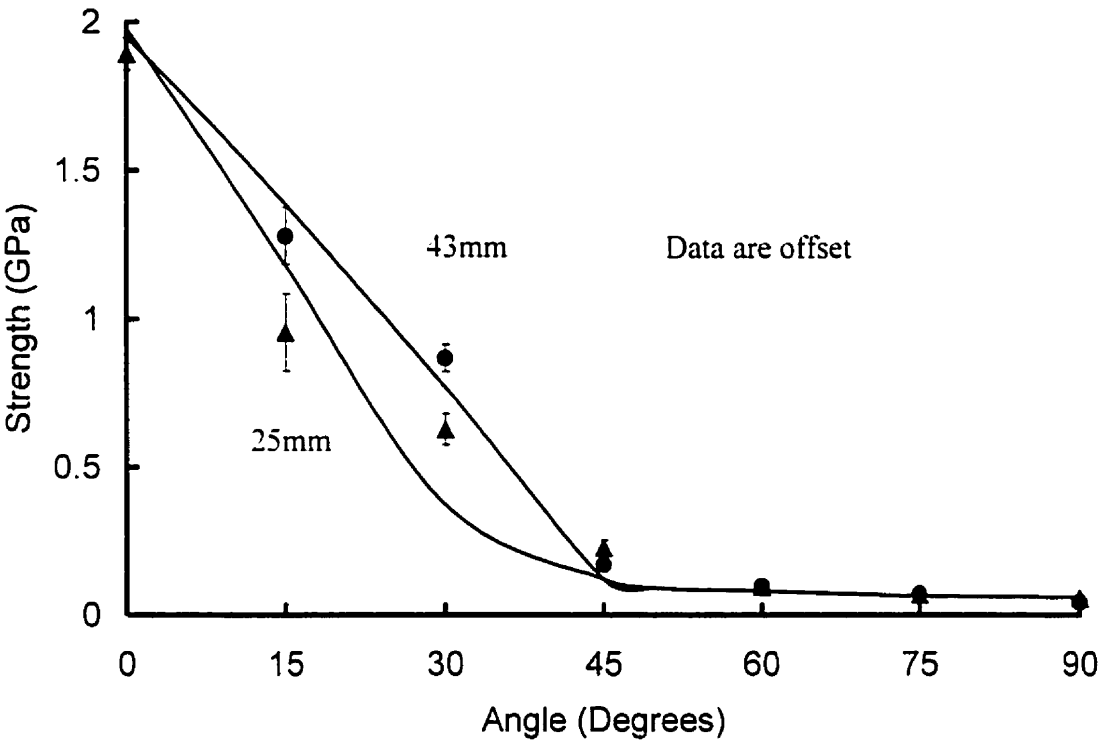

Figure 4.24. Strength model compared with test data

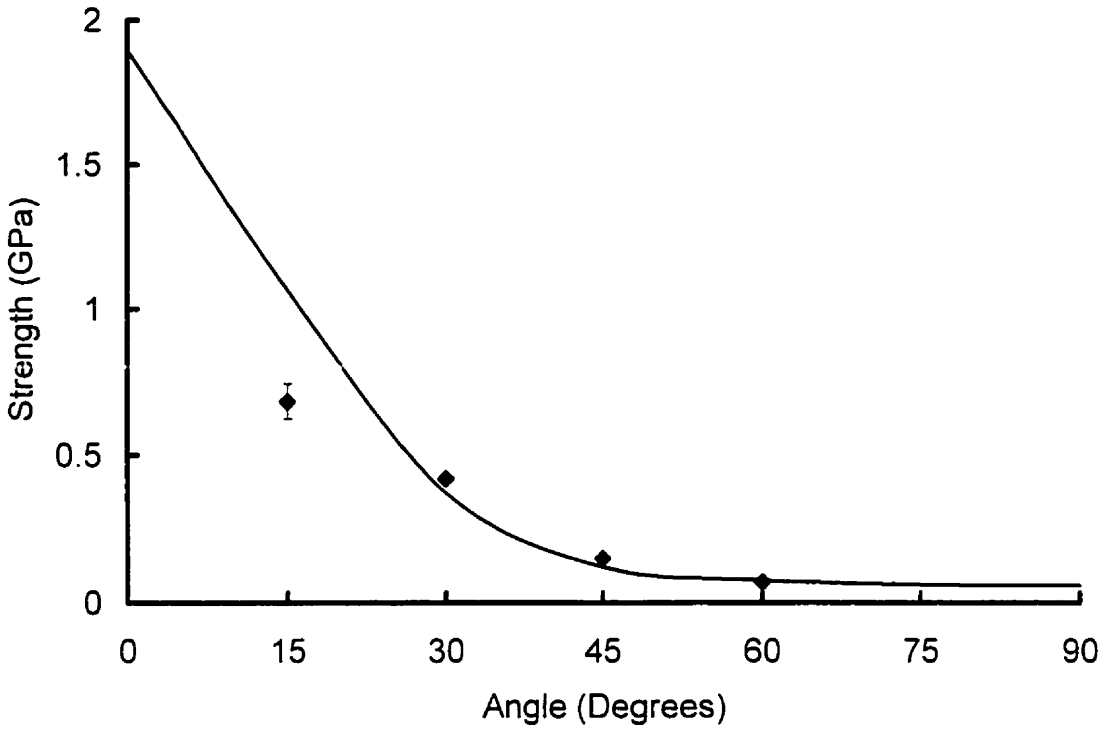

Figure 4.25. Strength model compared with test data (ASTM samples)

4.5. New Understanding of Composites

Traditionally we have treated composites as orthotropic or nonisotropic materials that have different properties in three mutually perpendicular directions or have material properties that are different in all directions. We believed that the composite properties could be estimated from the constituents, fibers and matrix, and the way they are combined together. We considered a composite as a whole body when we carried a mechanical analysis and did not connect the composites' properties with its shape.

Our current results show that the properties of a laminated composite not only depend on the constituents and the lay-up angles, but also depend on the size and shape.

This tells us that a composite is not a material but a structure and should be treated as such.

The lay-up angles and constituents provide the upper and lower stiffness boundaries for angle ply laminates. i.e. $\bar{Q}_{11}$ *and* $\frac{1}{\bar{S}_{11}}$ respectively. The true stiffness. within these boundaries. depends also on the shape. i.e. whether or not the fiber is directly loaded. One problem with the application of classical lamination theory. which was not noticed previously. is when we transfer the laminate stiffness from E_1. E_2. G_{12}. to E_x. E_y. G_{xy}. we not only transfer the stresses and strains but also transfer a hidden assumption that a ply is homogeneous. This homogenization can only be transferred when the ply is infinitely wide and long which is not true in the real world.

This is also true for the angle ply laminates' strength. There is no size-independent composite strength. except for the combination of 0^0 and 90^0 lay-ups. Since the shape factor and the failure mechanism have been involved. the strength we measured is the strength which belongs to a certain composite structure. i.e. a composite structure strength. The constituent properties provide the upper and lower boundaries for which the mixture laws may be used. These are the σ_{1u} and σ_{2u} respectively. When the lay up angles are not a combination of 0^0 and 90^0. the lay-up angles and the shape of the structure have to be involved. This implies that we cannot estimate the strength of a particular piece of composite correctly if we treat the composite as a material. Moreover. the failure mechanism is a key issue for understanding the composite strength. For angle ply laminates. when the lay-up angles are less than $\pm 45^0$. the failure is caused by the fibers

being highly stressed and flexed. The failure mechanism of the $\pm 45^0$ laminate appears to be in agreement with Rotem and Hashin mechanism, i.e. the onset of failure is due to lamina cracking. The specimen does not fail but continues to sustain the load. Cracking occurs progressively in various domains [49].

We believe we can obtain angle ply laminates' stiffness and strength values which approach the true values with our flat sample. The criterion here should be the degree to which we have succeeded in stressing the fibers. Earlier work on flat laminates [20] appears to have been successful in measuring the strength, since, when the specimens failed, a very large fraction of the fibers were broken. In this work, fewer fibers were broken. However, the use of notches to achieve the higher result meant that accurate values of elastic constants could not be obtained.

4.6. Implications for Design

Design software relies heavily on classical laminated plate theory, since most designs require specific stiffness values. This work, and the work on tubes already available, confirms that these designs can be used with confidence, so long as the edge effect and gripping effects are not too great. Edge softening effects seriously reduce stiffness for any angle ply component that has a width less than its length, while gripping effects are likely to constrain any angle ply component that has a length less than its width.

However, major companies, such as Boeing, do not use angle ply designs for civilian aircraft. The possibility of designing your material, much vaunted in the early days, and still to be found in many fiber composite texts, e.g. [39], has barely been realized. The main structure used is based on combinations of 0^0, 45^0, and 90^0 layers. This has the drawback that the 90^0 layer tends to split rather easily, thus limiting its usefulness. Angle ply laminates are notable by their absence, for the probable reason that the Tsai-Wu criterion is a general stress interaction criterion that is said to be used in industry. This can underestimate the strength of an angle ply laminate by more than a factor of 3.

The equivalent of angle ply laminates is widely used in the pressure vessel industry, where they have been shown to have excellent properties. They have been proven to be even better under biaxial than under uniaxial stresses. These are potentially more efficient designs than the aforementioned civilian aircraft standard. However, the question of gripping constraints leading to premature cracking needs to be addressed. Nevertheless, it is high time that the design software was reformed to agree with actual strength properties.

5. CONCLUSIONS

Our short wide sample tests gives values which agree well with classical lamination theory boundaries for the principal modulus E_x but not for Poisson's ratio. The best result for E_x are at a length/width ratio of about one half.

A serious edge softening existed in the specimens. The edge softening reduces laminate stiffness and strength. Edge softening is different from the well known edge effects which is caused by edge delamination.

The ASTM D3039 method is not capable of giving reliable moduli except for the 0/90 combinations. Furthermore, initial slopes should be used for determining whether moduli agree with lamination theory. The mean slope between one quarter and one half of the ultimate strain, as recommended in the standard, may however, be useful for design purpose.

The "industry" failure criteria are seriously in error and should not be used in composite design. Nor should ASTM D3039 method be used to estimate the strength or stiffness for any structure with other than 0^0 or 90^0 plies. Notched wide flat sample tests appear to be the best option here. However pressurized tube tests should be carried out to provide confirmation data.

An edge softening model has been set up. Angle ply laminate stiffnesses can be well estimated by using the model. Angle ply laminate strengths can also be fairly well estimated by using the model.

6. REFERENCES

1. P. C. Powell, "Engineering with Fiber-Polymer Laminates", Chapman & Hall, **9**, (1994)
2. M. F. Ashby, "Technology of the 1990's: Advanced Materials and Predictive Design", Philosophical Transactions of the Royal Society of London, **A322**, 393-407, (1987)
3. A. A. Griffith, "The Phenomena of Rupture and Flow in Solids", Philosophical Transactions of the Royal Society, **221A**, 193-198, (1920)
4. R. F. Gibson, "Principles of Composite Material Mechanics", **8**, McGraw-Hill (1994)
5. R. H. Pater, J. Arimond, "Polymer Composite Applications for Motor Vehicles (SP850)", R. H. Pater and J. Arimond (ed.), 44-46, SAE International, USA, (1991)
6. D. D. Dial, M. S. Howeth, "Advanced Composites Cost Comparison", 16th National SAMPE Symposium and Exhibition, Anaheim, California, (1971)
7. M. R. Piggott, "Load-Bearing Fiber Composites", Pergamon, 123, (1980)
8. S. Tsai, NASA **CR224**, (1965)
9. "Standard Test Method for Tensile Properties of Polymer Matrix Composite Materials", ASTM D 3039/D 3039M -95a, (1996)
10. G. Kress, "Width Influence on Stiffness Measurements of Multidirectional CFRP under Uniaxial Load", Comp. Eng., **2**, 83-90, (1992)
11. J. F. Clarke, R. A. Duckett, P. J. Hine, I. J. Hutchinson, I. M. Ward, et al. "Negative Poisson's Ratios in Angle-Ply Laminates: Theory and Experiment", Composites **Vol.25 No.9**, 863-868, (1994)
12. P. J. Hine, R. A. Duckett, I. M. Ward, " Negative Poisson's Ratios in Angle-Ply Laminates", J. of Materials Science Letters **16**, 541-544, (1997)
13. M. Khatibzadeh and M. R. Piggott, "The Effect of Width on the Mechanical Properties of Angle Ply Laminates", Comp. Sci. Tech., **58**, 497-504, (1998)
14. J. M. Whitney and N. J. Pagano "Shear Deformation in the Heterogeneous Anisotropic Plates", J. of Applied Mechanics Dec., 1031-1036, (1970)
15. N. J. Reddy , " A Simple High-Order Theory for Laminated Composite Plates" . J. of Applied Mechanics **51**, 745-752, (1984)
16. W. Becker and G. Kress, " Stiffness Reduction in Laminate Coupons due to the Free-edge Effect". Comp. Science & Technology **52**, 109-115, (1994)
17. Q. Sh. Bai, S. Murakami, Y. Kanagawa, "A Laminate Theory Incorporating the Effect of Interlaminar Deformation", J. of Composite Materials **Vol. 30 No. 20**. (1997)
18. M. B. Snell, "Strength and Elastic Response of Symmetric Angle-ply cfrp", Composites, **9**, 167-76, (1978)
19. C. T. Sun, B. J. Quinn, "Evaluation of Failure Criteria Using Off-axis Laminate Specimens", 7th Proc. Amer. Soc. for Composites, Oct, 97-105, (1992)
20. M. Khatibzadeh and M. R. Piggott, "The Effect of Fiber Alignment on Composite Strength: II. The Strength of Angle-ply Laminates", Composite Science and Technology **56**, 1443-1451, (1996)

21. P. D. Soden, R. Titching, P. C. Tse, "Experimental Failure Stresses for ±55 Filament Wound Glass Fiber Reinforced Plastic Tubes under Biaxial Loads", Composites, **Vol. 20, No.2 Mar.**, 125-135, (1989)
22. P. D. Soden, R. Kitching, P. C. Tse, Y. Tsavalas, "Influence of Winding Angle on the Strength and Deformation of Filament-Wound Composite Tubes Subjected to Uniaxial and Biaxial Loads", Composite Science and Technology **46**, 363-378, (1993)
23. J. Highton, A. B. Adeoye, P. D. Soden, " Fracture Stresses for ±75 Degree Filament Wound GRP Tubes under Biaxial Loads", J. of Strain Analysis, **Vol. 20 No. 3**, 139-150, (1985)
24. N. J. Pagano, J. M.Whitney, "Geometric Design of Composite Cylindrical Characterization Specimens", J. of Composite Material **4**, 360, (1970)
25. J. M. Whitney, N. J. Pagano, R. B. Pipes, "Design and Fabrication of Tubular Specimens for Composite Characterization", Composite Materials Testing and Design (2nd Conf.) ASTM STP497, 52-67, (1971)
26. I. M. Daniel, " Analysis of Tubular Specimen for Biaxial Testing of Composite Laminates", Proceedings of 3rd International Conference on Composite Materials (Paris), 840-885, (1980)
27. G. R. Toombes, S. R. Swanson, "Biaxial Testing of Composite Tubes", Experimental Mechanics, June, 186-193, (1985)
28. L. V. Smith, S. R. Swanson, "Design of a Cylindrical Specimen for Biaxial Testing of Composite Materials", J. of Reinforced Plastic and Composites **Vol. 16 No. 6**, 550-565, (1997)
29. S. R. Swanson, A. P. Christoforou, "Response of Qusai-Isotropic Carbon/Epoxy Laminates to Biaxial Stress", J. of Composite Materials **Vol. 20 Sept.**, 457-471, (1986)
30. S. R. Swanson, M. J. Messick, Z. Tian, "Failure of Carbon/Epoxy Lamina Under Combined Stress", J. of Composite Materials, **Vol. 21** July, 619-630, (1987)
31. S. R. Swanson, B. C. Trask, "An Examination of Failure Strength in [0/±60] Laminates under Biaxial Stress", Composite **Vol. 19, No. 5** Sept., 400-406, (1988)
32. S. R. Swanson, A. P. Christoforou, G. E. Colvin, Jr., "Biaxial Testing of Fiber Composite Using Tubular Specimens", Experimental Mechanics Sept., 238-243, (1988)
33. S. R. Swanson, B. C. Trask, "Strength of Quasi-Isotropic Laminates under Off-Axis Loading", Composite Science and Technology **34**, 19-34, (1989)
34. S. R. Swanson, G. R. Toombes, "Characterization of Prepreg Tow Carbon/Epoxy Laminates", J. of Engineering Materials and Technology, **Vol. 111** April, 150-153, (1989)
35. R. C. Tennyson, D. MacDonald, A. P. Nanyaro, "Evaluation of the Tensor Polynomial Strength Criterion to the Failure Analysis of Composite Materials", J. of Composite Material, **Vol. 12**, 63-75, (1978)
36. R. C. Tennyson, G. E. Wharram, G. Elliott, "Application of the Cubic Strength Criterion to the Failure Analysis of Composite Laminates", Fracture of Composite Materials, edited by Sih G. C. and Tamuzs V. P., 53-66, (1982)

37. Jinbo Bai, P. Seeleuthner, P. Bompard, "Mechanical Behavior of ±55 Filament-wound Glass-Fiber/Epoxy-resin Tubes: I. Microstructural Analysis, Mechanical Behavior and Damage Mechanisms of Composite Tubes under Pure Tensile Loading, Pure Internal Pressure, and Combined Loading", Composite Science and Technology **57**, 141-153, (1997)
38. Jinbo Bai, G. Hu, P. Bompard, "Mechanical Behavior of ±55 Filament-wound Glass-Fiber/Epoxy-resin Tubes: II. Micromechanical Model of Damage Initiation and the Competition between Different Mechanisms", Composite Science and Technology **57**, 155-164, (1997)
39. G. Hu, Jinbo Bai, E. Demianouchko, P. Bompard, "Mechanical Behavior of ±55 Filament-wound Glass-Fiber/Epoxy-resin Tubes: III. Macromechanical Model of the Macroscopic Behavior of the Tubular Structures with Damage and Failure Envelope Prediction", Composite Science and Technology **58**, 19-29, (1998)
40. R. M. Jones, "Mechanics of Composite Materials",(2nd ed.) Taylor & Francis, Inc. (1998)
41. R. M. Jones, "Mechanics of Composite Materials", Hemisphere Publishing Co., New York (1975)
42. P. D. Soden, M. J. Hinton, A. S. Kaddour, "A Comparison of Predictive Capabilities of Current Failure Theories for Composite Laminates", Composite Science and Technology **58**, 1225-1254, (1998)
43. M. J. Hinton, P. D. Soden, "Predicting Failure in Composite Laminates: The Background to the Exercise", Composite Science and Technology **58**, 1001-1010, (1998)
44. R. B. Pipes and N. J. Pagano,"Interlaminar Stresses in Composite Laminates under Uniform Axial Extension", J. of Composite Materials, **4**, 538-548, (1970)
45. R. B. Pipes and I. M. Daiel, "Moire Analysis of the Interlaminar Shear Edge Effect in Laminated Composite", J. of Composite Materials, **4**, 255-259, (1971)
46. J. M. Whitney, I. M. Daniel, R. B. Pipes, "Experimental Mechanics of Fiber Reinforced Composite Materials", The Society for Experimental Mechanics, (1984)
47. L. Charles, "Statistical Design and Analysis of Engineering Experiments", New York: McGraw Hill, 100-110, (1973)
48. W.R. Broughton, M. Kumosa, D. Hull, "Analysis of the Iosipescu shear test as applied to unidirectional carbon fiber reinforced composite", Composite Science and Technology, **38**, 299-326, (1990)
49. A. Rotem, Z. Hashin, "Failure Modes of Angle Ply Laminates", J. of Composite Materials, **9**, 191-206, (1975)
50. M. Khatibzadeh, "The Strength of Angle-Ply Laminates and Composites with Misaligned Fibers", Master Thesis, Department of Chemical Engineering and Applied Chemistry, University of Toronto, (1997)
51. J. Echaabi, F. Torchu, "Failure Mode Dependent Strength Criteria for Composite laminates", J. of Reinforced Plastic and Composite, **V. 16, No. 10**, (1997)
52. T. E. Matikas, N. J. Pagano, "Recent Advances in Composite Science", Composite, **29B**, 91-98, (1998)

53. R. G. C. Arridge, P. I. Barham, C. J. Farell, and A. Keller. "The Importance of End Effects in the Measurement of Highly Anisotropic Materials," J. of Material Science, **11**, 788, (1967)
54. Horgan, C. O., "Saint-Venant End Effects in Composites", J. of Composite Materials, **16**, 411-422, (1982)
55. Piggott M. R. and Dai S. R. "Proceeding of the American Society for Composites", Dearborn, MI, .91-98, (1997)
56. Horgan, C. O., "Some Remarks on Saint-Venant's Principle for Transversely Isotropic Composites" , J. of Elasticity, **2(4)**, 335-339, (1972)
57. Choi, I. and Horgan, C. O., "Saint-Venant's Principle and End Effects in Anisotropic Elasticity", J. of Applied Mechanics, **44**, 424-430, (1977)
58. J. A. Kies, "Maximum Strains in the Resin of Fiber Glass Composites". U.S. Naval Research Laboratory Report No. 5752, (1962)

7. LIST OF NOMENCLATURE

Where possible, standard nomenclature has been used. Duplication could not be avoided entirely, but each symbol is described fully in the appropriate part of the thesis. This symbol system is adopted from [7].

A	extensional stiffness; always has subscripts indicating directions e.g. A_{ij}
B	bending-extensional coupling stiffness; always has subscripts indicating directions, e.g. B_{ij}
C	stiffness; always has subscripts indicating directions e.g. C_{ij}
D	bending stiffness; always has subscripts indicating directions e.g. D_{ij}
E	Young's modulus; usually has subscripts indicating directions or materials, e.g. E_x, E_1, E_f, E_m
F	strain concentration factor
F	Tsai-Wu failure criterion factor; always has subscripts indicating directions, e.g. F_{12}, F_{11}
G	shear modulus; always has subscripts indicating directions, e.g. G_{xy}
L	specimen gauge length
M	moment of force; always has subscripts indicating directions, e.g. M_x
N	resultant force; always has subscripts indicating directions, e.g. N_x
Q	reduced stiffness; subscripts indicate directions
$\bar{Q}$	transformed reduced stiffness; subscripts indicate directions
S	compliance; subscripts indicate directions
$\bar{S}$	reduced compliance; subscripts indicate directions
T	temperature
[T]	transformed matrix for rotation of axes
V	volume fraction; subscript indicates material or form
W	specimen width
b	width of strips
d	tube diameter
f	fringe value
h	specimen thickness
k	number of laminate layers
n	fringe order or a variable number
s	specimen aspect ratio L/W
u	displacement in x direction
v	displacement in y direction

w	displacement in z direction
z	distance from laminates mid plane; subscripts indicates layers
x	direction
y	direction
z	direction
α	thermal deformation coefficient
β	coefficient of moisture expansion
Δ	difference
ε	strain; subscripts indicate directions or material, or limit
ϕ	angle of axis rotation
γ	shear strain; subscripts indicate shear plane or material
κ	laminate middle surface curvature; subscripts indicate directions
λ	stress decay length over which the stress decays to 1/e of the value of the stress at end
ν	Poisson's ratio: subscripts indicate directions or material
σ	tensile stress: subscripts indicate direction or material, or limit
τ	shear stress: subscripts indicate direction or material, or limit
ξ	experimental factor for strength

Subscripts

0	indicates neutral surface or a number
1, 2, 6	direction or number
c	compressive or critical values
exp	experiment
f	fiber
m	matrix
s	symmetric
th	theoretical
u	ultimate
x	direction
y	direction
z	direction
ϕ	direction

Superscripts

0	indicates neutral surface or a number
c	coating material
s	specimen
T	thermal

8. APPENDIX

A.1 Testing Method

A.1.1. Test Instrument

Load Cell:	MTS 10 TONS Load cell
Load Recorder:	MTS 431 Recorder
Strain Indicator:	P-3500 Strain Indicator
	VISHAY / ELLIS-20 Digital Strain Indicator
	Both from the Measurement Group Inc.
Two Pen Recorder:	Linear 1200

A.1.2. Clamps

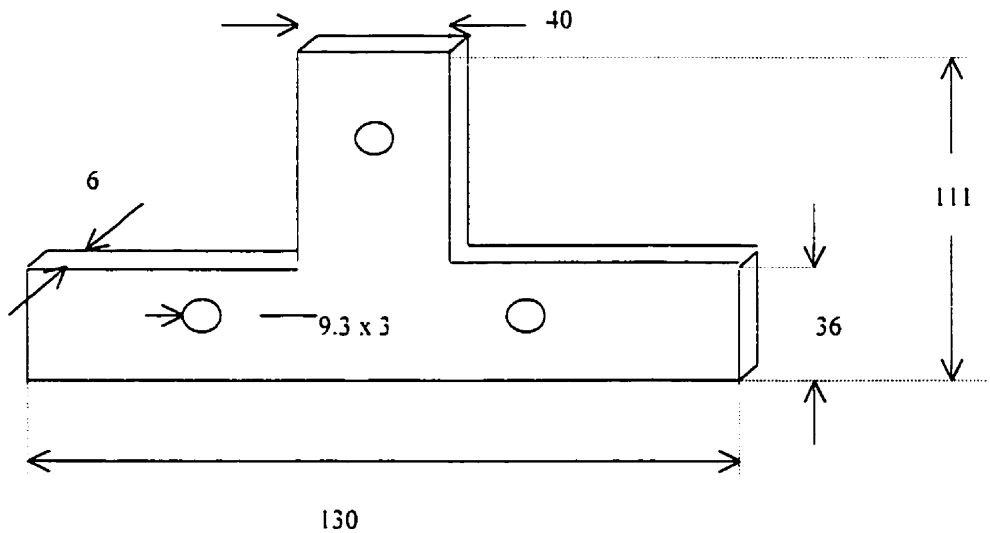

Figure A1. Clamp for 100mm width specimens (Unit in mm)

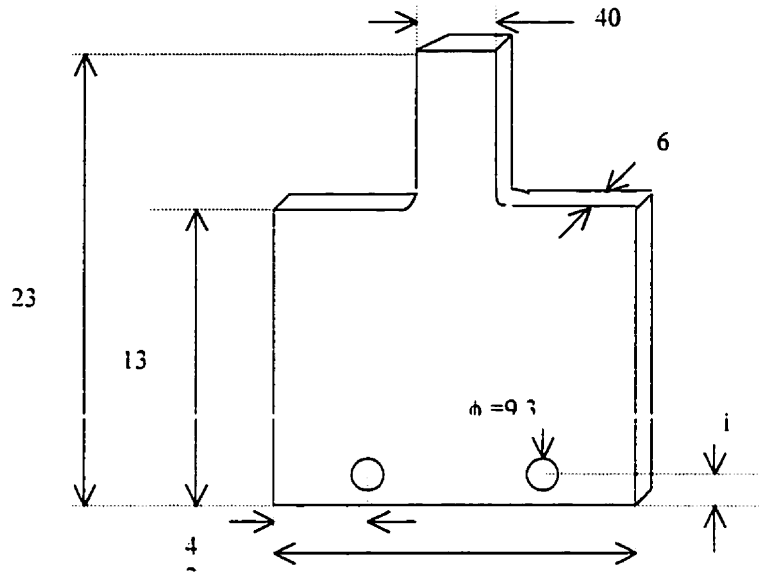

Figure A2. The other clamp for the 100mm width specimens (Unit in mm)

A.2 Photoelastic Analysis

Table A1. Isochromatic Fringe Characteristics

Colour	Approximate Relative Retardation (nm)	Fringe Order (N)
Black	0	0
Gray	160	0.28
White	260	0.45
Pale Yellow	345	0.60
Orange	460	0.80
Dull Red	520	0.90
Purple	575	1.00
Deep Blue	620	1.08
Blue-Green	700	1.22
Green-Yellow	800	1.39
Orange	935	1.63
Rose Red	1050	1.82
Purple	1150	2.00
Green	1350	2.35
Green-Yellow	1440	2.50
Red	1520	2.65
Red/Green	1730	3.00
Green	1800	3.10
Pink	2100	3.65
Pink/Green	2300	4.00
Green	2400	4.15

A.2.1. Photoelastic Fringe Pattern in Tension

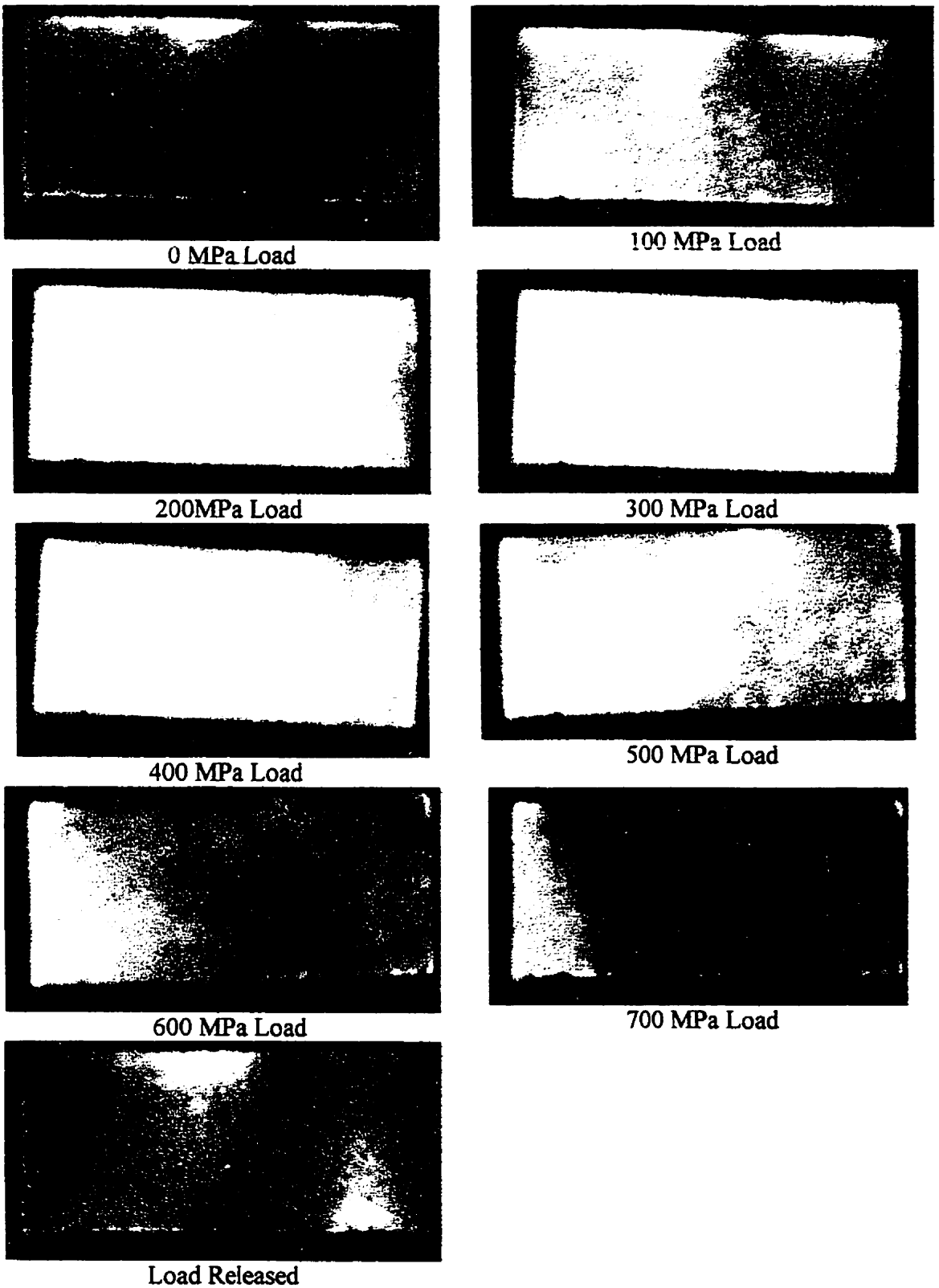

Figure A3. Photoelastic fringe patterns of $[0]_8$ sample

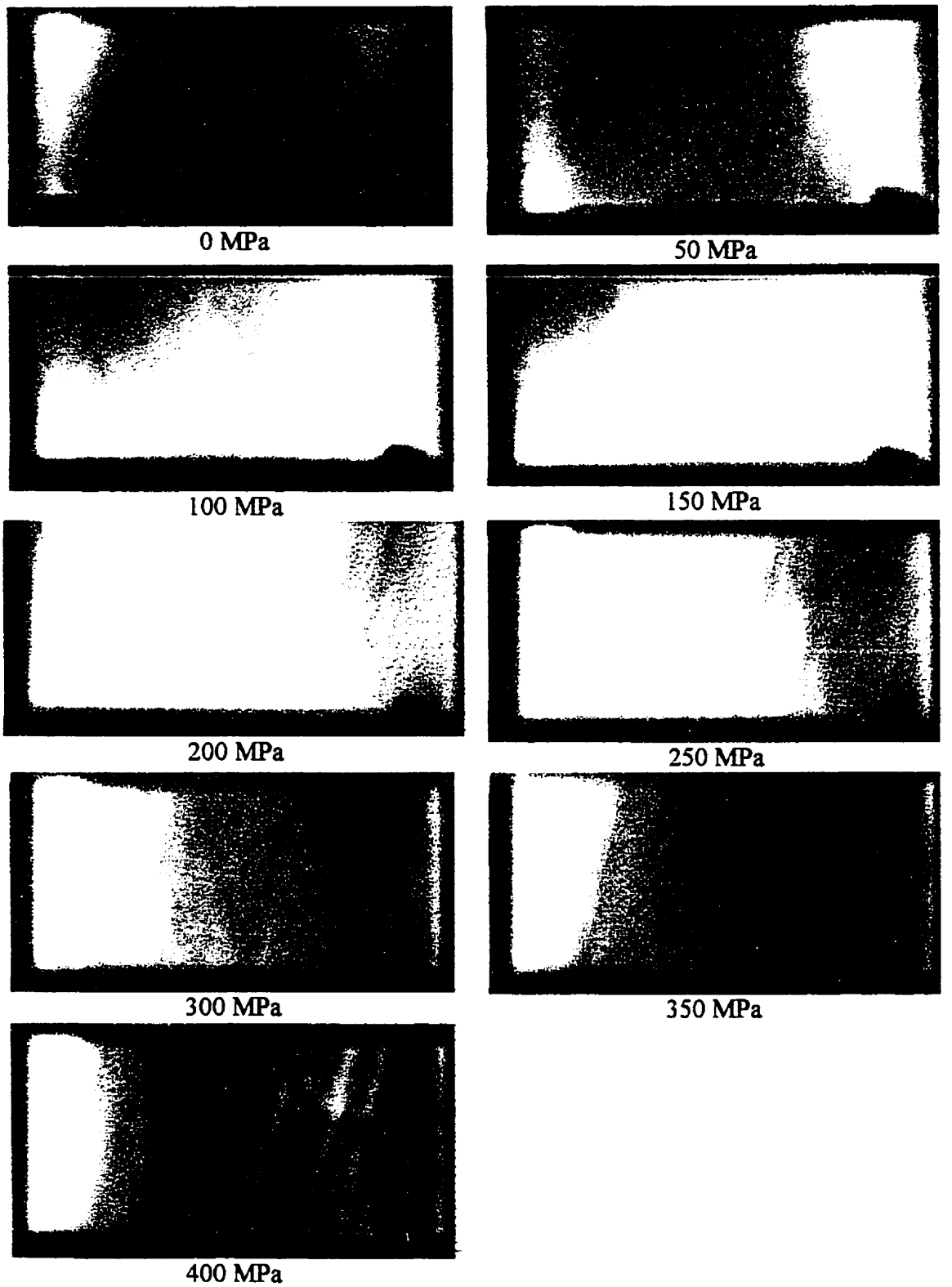

Figure A4. Photoelastic fringe patterns of $[\pm 15]_{2s}$ sample

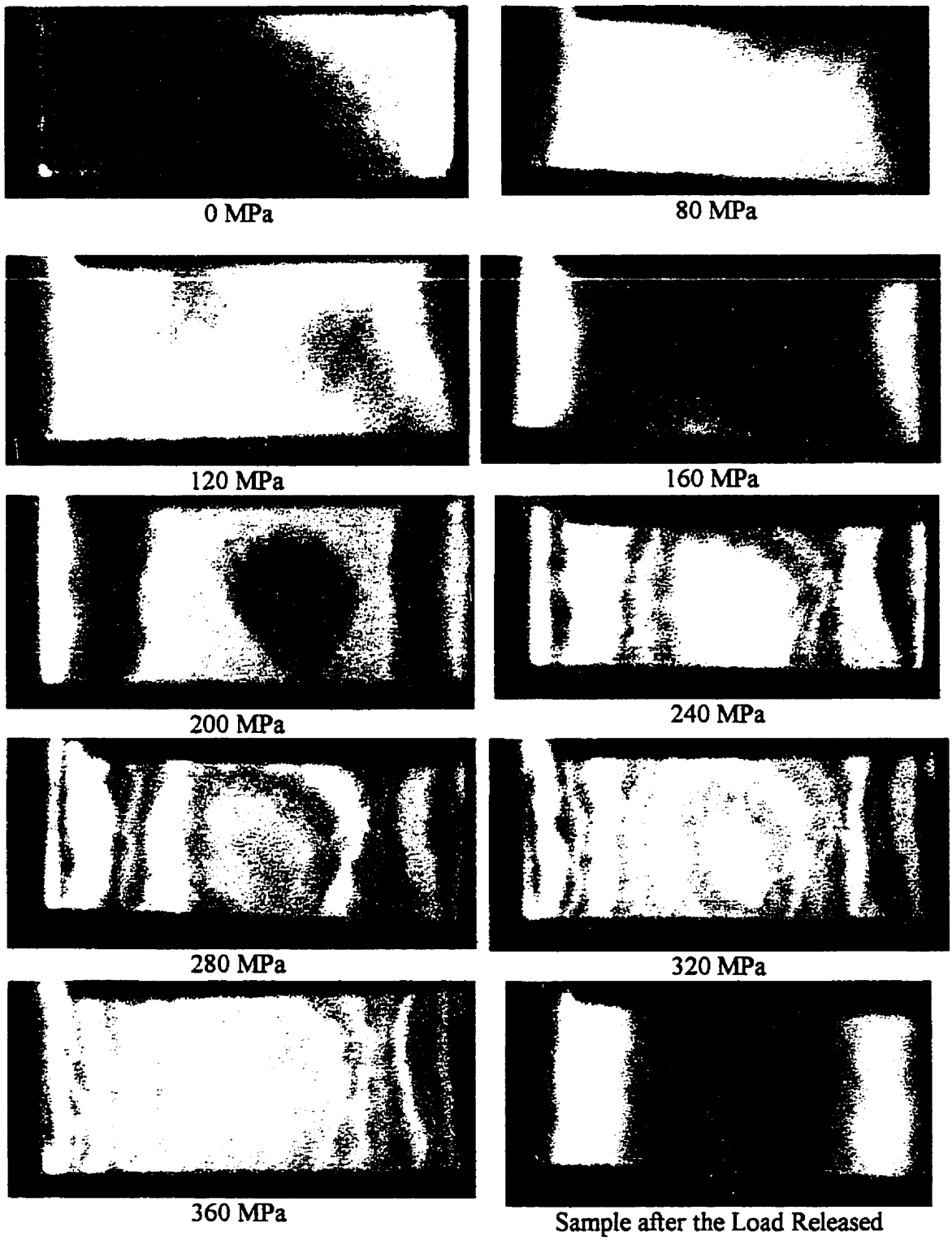

Figure A5. Photoelastic fringe patterns of $[\pm 30]_{2s}$ sample

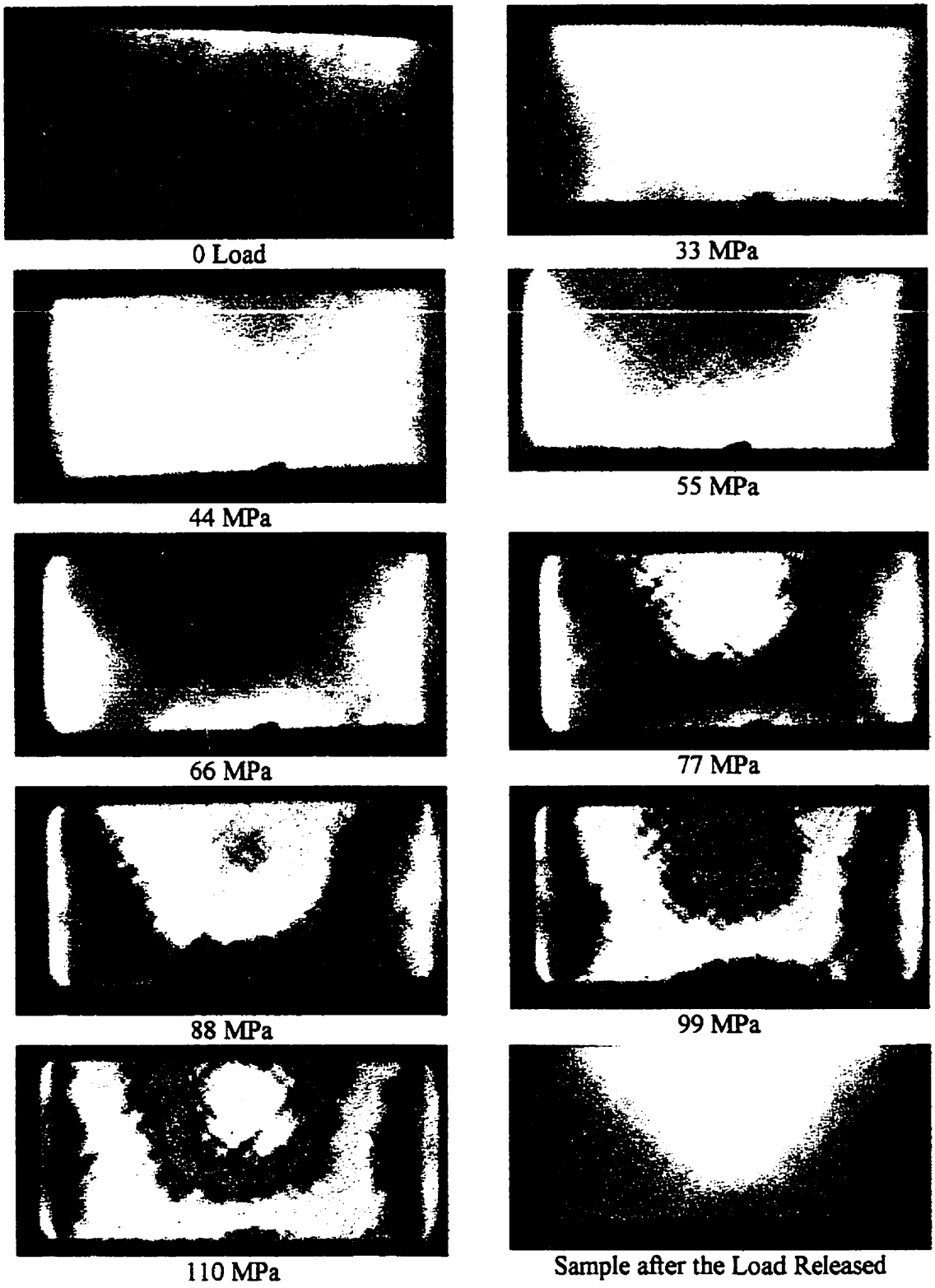

Figure A6. Photoelastic fringe patterns of $[\pm 45]_{2s}$ sample

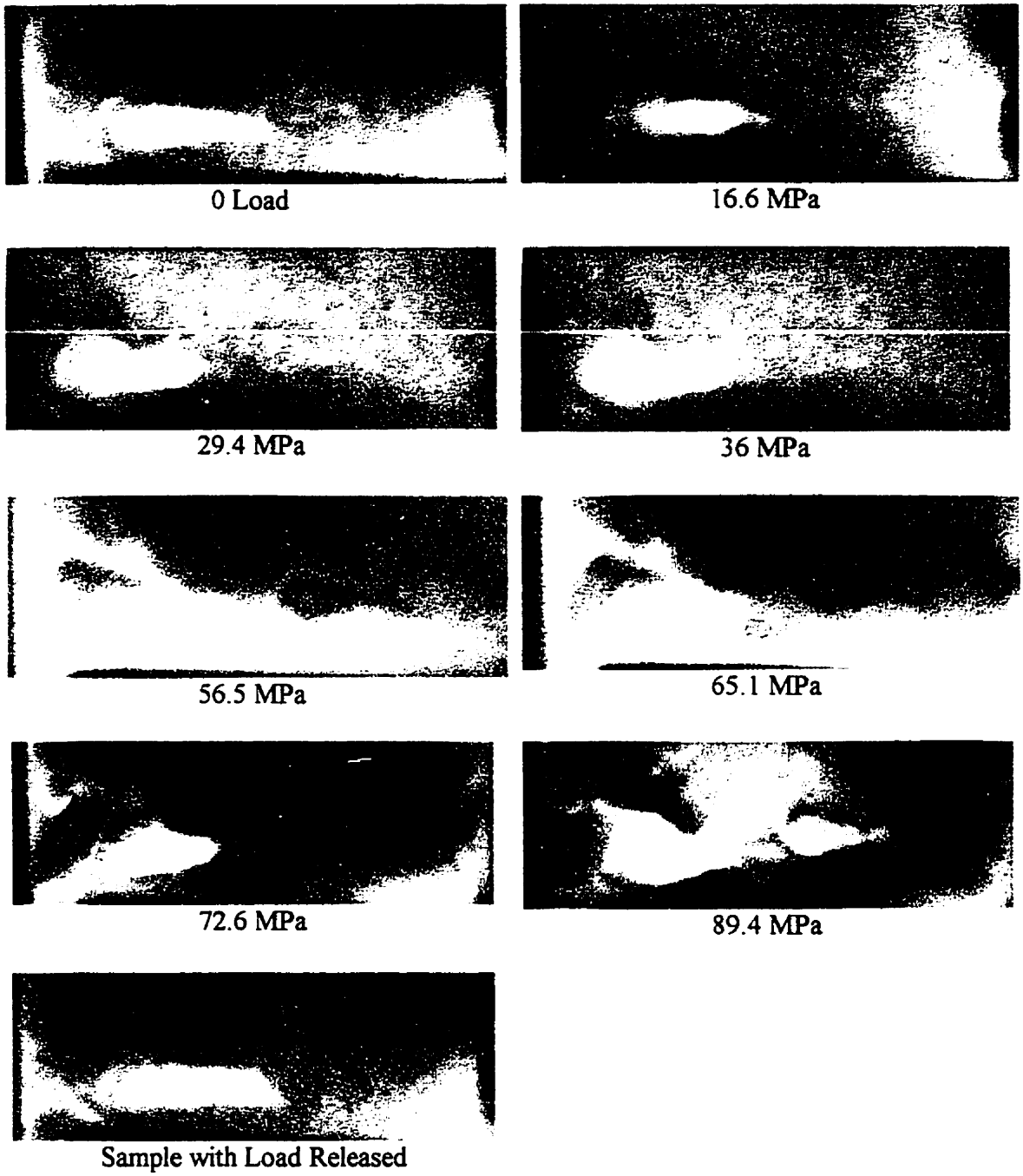

Figure A7. Photoelastic fringe patterns of $[\pm 60]_{2s}$ sample

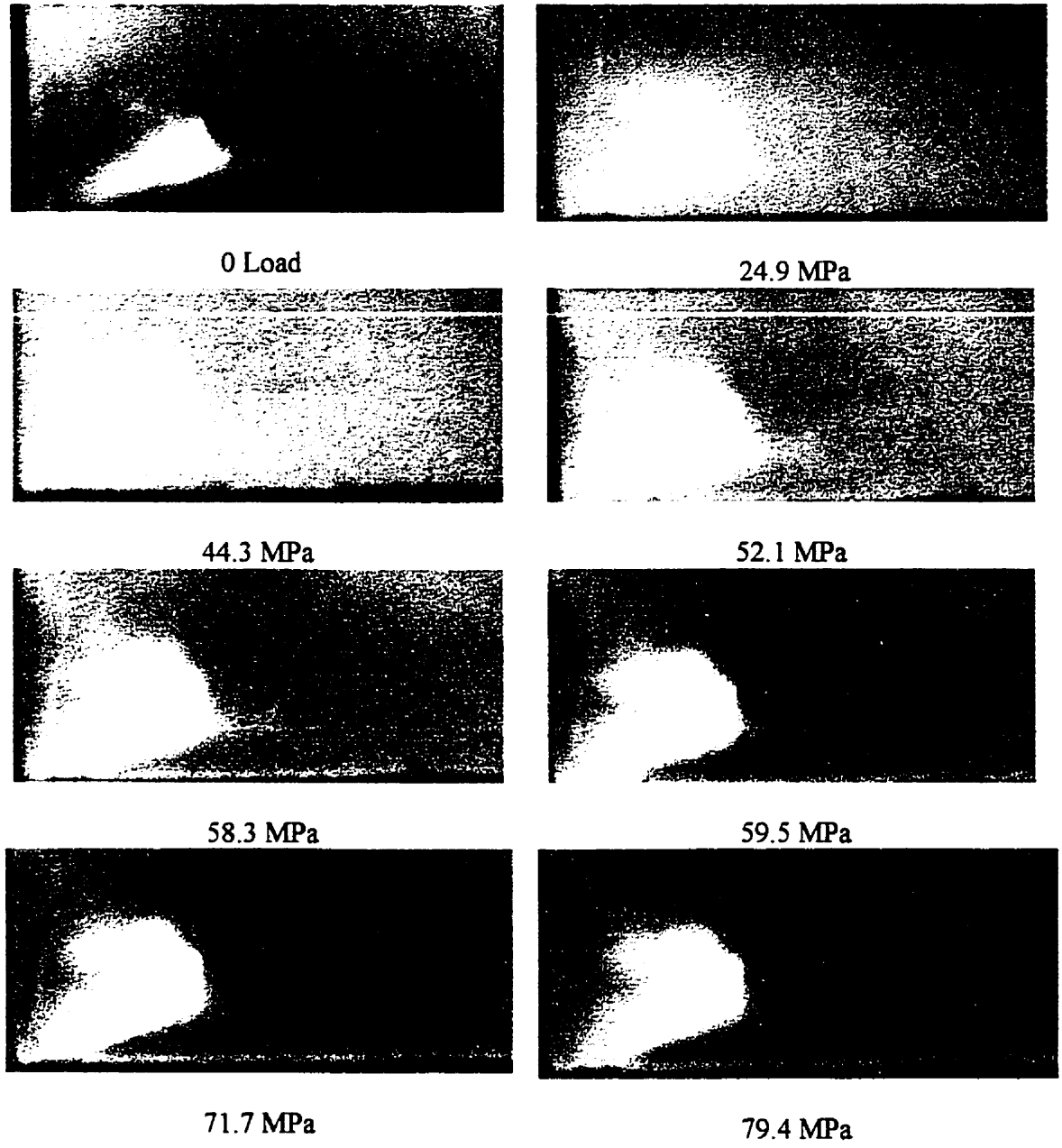

Figure A8. Photoelastic fringe patterns of $[\pm 75]_{2s}$ sample

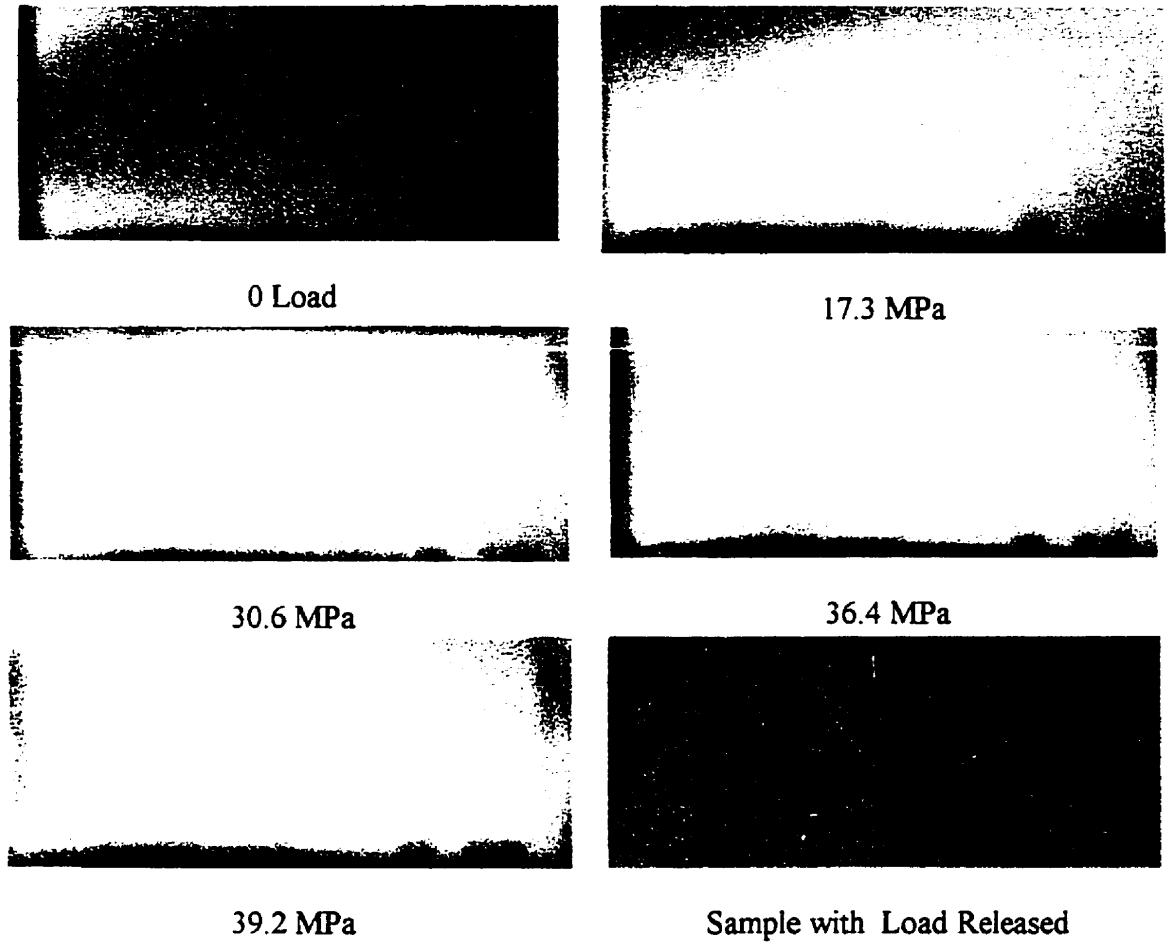

Figure A9. Photoelastic fringe patterns of $[90]_8$ sample

A.2.2. Photoelastic Fringe Patterns in Compression

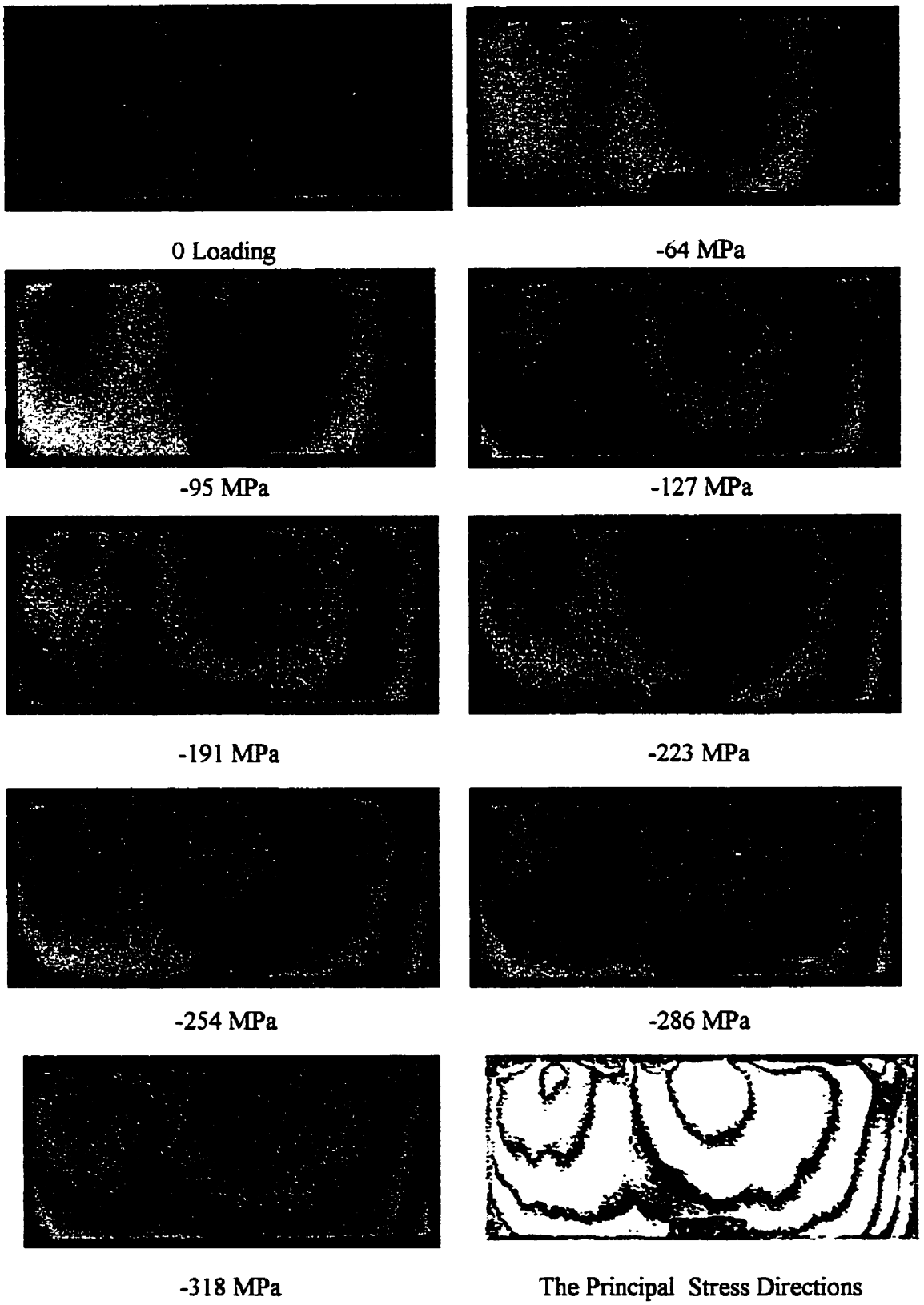

Figure A10. Photoelastic fringe patterns of $[\pm 15]_{2s}$ sample in compression

A.3 Elastic Constants and Strengths

Table A2. Elastic Constants and Strength of ASTM Samples

$[\pm\phi]_{2s}$	E_x (GPa)	ν_{xy}	σ_u (MPa)	ε_u (%)
15	88.8±5.5	0.97±0.09	680±60	0.73±0.04
30	33.7±1.2	1.40±0.10	420±10	1.95±0.20
45	13.9±1.2	0.73±0.03	150±5	3.41±0.21
60	9.0±0.5	0.31±0.04	70±4	0.77±0.05

Table A3. Elastic Constants and Strength of 25mm Width Samples

$[\pm\phi]_{2s}$	E_x (GPa)	ν_{xy}	σ_u (MPa)	ε_u (%)
0	151±9	0.24±0.16	1892±54	1.91±0.28
15	115±8	0.57±0.19	954±130	0.88±0.10
30	54.2±12.9	1.03±1.36	627±53	2.64±0.31
45	22.0±3.3	0.73±0.05	227±24	6.29±0.85
60	12.4±1.3	0.31±0.01	95±3	1.04±0.10
75	11.7±1.5	0.08±0.01	69±15	0.68±0.14
90	10.7±1.5	0.03±0.00	57±8	0.58±0.11

Table A4. Elastic Constants and Strength of 43mm Width Samples

$[\pm\phi]_{2s}$	E_x (GPa)	ν_{xy}	σ_u (MPa)	ε_u (%)
0	163±30	0.23±0.10	-	-
15	141±20	0.33±0.13	1279±96	1.12±0.07
30	57.8±15.2	0.30±0.05	868±46	3.36±0.92
45	29.0±3.8	0.37±0.11	169±5	2.25±0.10
60	13.4±1.5	0.28±0.03	97±7	1.20±0.14
75	11.1±1.7	0.06±0.01	71±9	0.64±0.09
90	9.8±0.8	0.01±0.00	42±8	0.43±0.09

Table A5. Elastic Constants and Strength of 100mm Width Samples

$[\pm\phi]_{2s}$	E_x (GPa)	ν_{xy}	σ_u (MPa)	ε_u (%)
0	-	-	-	-
15	110±7.8	0.09±0.04	-	-
30	59.8±7.6	0.29±0.16	-	-
45	32.7±6.5	0.20±0.07	-	-
60	13.4±1.2	0.13±0.06	-	-
75	10.7±0.5	0.08±0.04	-	-
90*	10.7±0.6	0.04±0.02	-	-

*: Average of 2 specimens.

A.4 Elastic Constants (ASTM D3039 Criterion)

Table A6. Elastic Constants and Strength of 25mm Width Samples

$[\pm\phi]_{2s}$	E_x (GPa)	ν_{xy}	σ_u (MPa)	ε_u (%)
0	140±8	0.24±0.10	1892±54	1.91±0.28
15	106±7	0.73±0.14	954±130	0.88±0.10
30	39±2	1.25±0.04	627±53	2.64±0.31
45	17.6±1.6	0.74±0.01	227±24	6.29±0.85
60	11.4±0.5	0.31±0.01	95±3	1.04±0.10
75	11.2±1.4	0.08±0.01	69±15	0.68±0.14
90	9.7±0.7	0.03±0.00	57±8	0.58±0.11

Table A7. Elastic Constants and Strength of 43mm Width Samples

$[\pm\phi]_{2s}$	E_x (GPa)	ν_{xy}	σ_u (MPa)	ε_u (%)
0	146±9	0.23±0.08	-	-
15	108±6	0.65±0.13	1279±96	1.12±0.07
30	44±4	0.70±0.16	868±46	3.36±0.92
45	24.2±3.3	0.34±0.10	169±5	2.25±0.10
60	11±0.7	0.29±0.02	97±7	1.20±0.14
75	11.1±0.4	0.06±0.01	71±9	0.64±0.09
90	9.4±0.8	0.02±0.00	42±8	0.43±0.09

Table A8. Elastic Constants and Strength of 100mm Width Samples

$[\pm\phi]_{2s}$	E_x (GPa)	ν_{xy}	σ_u (MPa)	ε_u (%)
0	-	-	-	-
15	81±6	0.44±0.08	-	-
30	40±4	0.87±0.01	-	-
45	22±1	0.55±0.22	-	-
60	10.4±0.7	0.29±0.03	-	-
75	9.3±0.2	0.10±0.00	-	-
90*	10±0.7	0.04±0.02	-	-

*: Average of 2 specimens.

A5. Stress Concentration on 100 mm Specimen

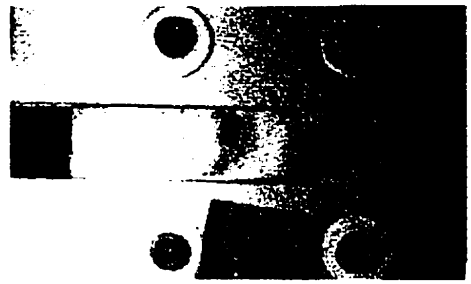

Figure A11. The 100 mm $[\pm 15]_{2s}$ specimen under 1.8 kN load